Integration of Advanced Optics for Trapped Ion Quantum Information Processing

by

Rachel M. Noek

Department of Electrical and Computer Engineering
Duke University

Date: _____

Approved:

_____
Jungsang Kim, Supervisor

_____
David J. Brady

_____
Daniel J. Gauthier

_____
John E. Thomas

_____
Peter Maunz

Dissertation submitted in partial fulfillment of the requirements for the degree of Doctor of Philosophy in the Department of Electrical and Computer Engineering in the Graduate School of Duke University
2013

Abstract

Integration of Advanced Optics for Trapped Ion Quantum Information Processing

by

Rachel M. Noek

Department of Electrical and Computer Engineering
Duke University

Date: _____

Approved:

_____
Jungsang Kim, Supervisor

_____
David J. Brady

_____
Daniel J. Gauthier

_____
John E. Thomas

_____
Peter Maunz

An abstract of a dissertation submitted in partial fulfillment of the requirements for the degree of Doctor of Philosophy in the Department of Electrical and Computer Engineering
in the Graduate School of Duke University
2013

Abstract

Trapped ion systems are the leading candidate for quantum information processing because many of the critical components have already been demonstrated. Scaling trapped ion systems to large numbers of ions is currently believed possible, but much work remains to prove the viability of these large systems. High fidelity computation demands quantum error correction operations which rely on fast, high fidelity detection of the quantum state of a single ion, and high efficiency light collection is essential for rapidly interconnecting remote quantum computing units. The internal states of the ion chosen to encode a quantum bit can be distinguished by detecting light from the ion while the ion is exposed to a probe beam that causes one state to scatter light, but not the other state. To show the viability of collecting light from a point source using a micro-mirror, we demonstrate 27% light collection efficiency from a micro-bead over a large (5 mm) field of view with a 100 μm diameter spherical micro-mirror placed close to the point source. In a separate experiment, we demonstrate high speed, high fidelity state detection of a single $^{171}Yb^{+}$ ion using a very large NA (NA=0.6) lens placed outside the vacuum chamber approximately 1 cm from the ion. With this high NA lens we achieve state detection fidelities of 99%, 99.856(8)%, and 99.915(7)% which correspond to detection times of 10.5, 28.1, and 99.8 μs, respectively. A time of 10.5 μs is the shortest detection time that has been demonstrated in a trapped ion system and is comparable to ion gate times. The fidelity of 99.915% is the highest fidelity demonstrated for an ionic hyperfine qubit.

To my dad for introducing me to science, and to my husband Akita for his continuous support.

Contents

List of Tables

List of Figures

List of Abbreviations and Symbols

Abbreviations

NA	Optical Numerical Aperture.
FoV	Field-of-View: the spatial dimension over which an imaged object is not significantly distorted.
qubit	Quantum bit.
UHV	Ultra High Vacuum, in this document the term is used for pressures $<10^{-10}$ Torr.
UV	Ultra-Violet, the short wavelength or blue color end of the optical spectrum.
EOM	Electro-Optic Modulator.
AOM	Acousto-Optic Modulator, shifts the frequency and diffracts light using sound waves. Also used in this work as fast laser power switches.
ECDL	External Cavity Diode Laser.
TEC	Thermo-Electric Cooler.
PDH	Pound-Drever-Hall, a common laser locking scheme.
PZT	PiezoElectric Transducer, used for short, finely controlled length adjustments.
EMCCD	Electron-Multiplied Charge-Coupled Device, a type of scientific camera.
FS	Fused Silica.
CPGA	Ceramic Pin Grid Array package.
AR	Anti-Reflection, an optical coating to minimize light reflection.

HR	High Reflectivity, an optical coating to maximize light reflection.
RF	Radio Frequency.

Acknowledgements

This thesis would not be possible without the help and advice of my mentors Prof. Jungsang Kim and Dr. Peter Maunz. They have taught me how to approach problems, how to design experiments, and how to identify and control the critical parameters in an experiment. I can never thank them enough for having the patience to accept me as a math major and turn me into a good experimentalist. It has been a rough road, but is has also been fun and extremely rewarding.

Much of my success is due to my lab mates: Dr. Kyle McKay provided a logical, balanced viewpoint when I needed it during the first two years of a difficult transition from cushy office job to leaning over an optical table in a freezing cold lab. Emily Mount has taught me by practice how to be more efficient in the lab, and that the best route to take sometimes is to just try it! Kyle, Emily, and Hui Son have taught me almost all I know about practical mechanical design, always suggesting things that fit the task perfectly. I must thank Richard Nappi for helping me realize those designs in the student machine shop and for proposing modifications that made the machining considerably more approachable. To my Green Team (Geert Vrijsen and Daniel Gaultney): thanks for making it more fun in the lab; having teammates is better than doing it solo. I only wish you had both joined me sooner. Thank you also to Dr. Taehyun Kim, Dr. Caleb Knoernschild, Dr. Soyoung Baek, and Stephen Crain, you provided help and guidance at critical times. To Andre van Rynbach, thanks for your interest in optical cavities and your initiative to help when there was

too much work for one person.

I would be remiss if I forgot to mention those who helped me get here. Thank you to both of my parents for encouraging and supporting me as I carve out my place in the world; life is more fun when your family is proud of you. Also, the scientists in my life before Duke have much to do with my success here, and I cannot express how much I appreciate the encouragement and support I received at Sandia National Labs through Dr. Steven Thornberg, Dr. Jerilyn Timlin, and Dr. Deborah Hunka. You are the three who motivated me, who cheered me on. Whenever I am discouraged, I can hear you saying, *"You can do it."*

Thank you to IARPA/ARO, DARPA, and NSF via my resourceful advisor for funding me through graduate school. And thank you to Milton Chang and the Optical Society of America as well as the Department of Electrical and Computer Engineering and Duke Graduate School for providing travel support to various conferences so I could present my work to my peers and betters.

1

Introduction

Quantum computers have drawn increasing interest in the past few decades for their potential to solve certain types of problems that are intractable with a classical computer. The idea of the quantum computer has been around since the 1980s, when Richard Feynman proposed that a quantum based computer could more efficiently simulate quantum mechanical systems (Feynman, 1986). Aside from quantum system simulations, quantum computers would provide rapid decryption of particular types of cryptographic codes that are currently considered very secure. Several algorithms have been developed that present a theoretical groundwork for practical usage of a quantum computer, including Grover's search algorithm (Grover, 1996), the quantum Fourier transform (Coppersmith, 1994), and Shor's integer factorization (Shor, 1994).

Although some theoretical groundwork exists, the experimental quantum computer is still far from practical use. Entanglement of several particles (Leibfried et al., 2005; Haffner et al., 2005; Monz et al., 2011), factoring of small numbers (Vandersypen et al., 2001), and violations of Bell's inequality (Rarity and Tapster, 1990; Matsukevich et al., 2008) have been demonstrated, but more complex computations have not yet been attempted due to the large number of bits and manipulations

required to perform a quantum circuit (~3,500 bits are required for factoring a 200-digit number without any error correcting scheme (Beckman et al., 1996)).

1.1 Quantum versus classical computing

The quantum bit (qubit) constitutes the fundamental difference between classical computers and quantum computers. A classical bit is binary and thus can only represent one of two states: $|0\rangle$ or $|1\rangle$. A quantum bit can represent these two states, as well as any superposition between them, that is $\alpha|0\rangle + \beta|1\rangle$, where $|\alpha|^2 + |\beta|^2 = 1$ and $\alpha, \beta \in \mathbb{C}$. For two independent qubits, $\alpha|0\rangle + \beta|1\rangle$ and $\alpha'|0\rangle + \beta'|1\rangle$, the combined state is $\alpha\alpha'|00\rangle + \beta\alpha'|10\rangle + \alpha\beta'|01\rangle + \beta\beta'|11\rangle$. Two classical bits would be able to represent only one of these states at any given moment: $|00\rangle$, $|10\rangle$, $|01\rangle$, or $|11\rangle$. Quantum algorithms take advantage of the qubits' ability to hold exponentially more information than classical bits (although this is controversial because there is not infinite precision in the readout) to improve the scaling of computations. For example, Shor's algorithm takes time $\mathrm{O}(\log N)$ to factor an integer N (Shor, 1994), where the best classical algorithm takes time $\mathrm{O}(\mathrm{e}^{(\log N)^{1/3}(\log\log N)^{2/3}})$ (Odlyzko, 1995).

1.2 Quantum computing with trapped ions

It is critical to make a careful selection of the physical qubit, considering the requirement for many qubits and the varied manipulations necessary to carry out a complete circuit. The qubit needs to have a two level quantum system that can be coherently manipulated, maintain coherence much longer than typical gate times, and be read out when necessary. Here, trapped ions are used due to their long relative coherence times (Fisk et al., 1997; Olmschenk et al., 2007) and the scalability of qubit interactions (Cirac and Zoller, 2000; Molmer and Sorensen, 1999; Kim et al., 2005). An ion comprises a definite two-level system based on hyperfine ground states or the

combination of a ground and long-lived excited state that has the benefit of easy measurement via the detection of photon emission. Using ions, it is also possible to convert between a stationary qubit (ion) and a convenient "flying" qubit (photon) that can travel long distances (i.e. outside the vacuum chamber).

1.3 Scaling Trapped Ion Quantum Computing

Major challenges remain in scaling trapped ion quantum computing. Microfabricated planar ion traps have been demonstrated (Seidelin et al., 2006) and provide a scalable solution for ion trap structure. Segmented microfabricated chip ion traps would have dedicated regions for storing and processing quantum information; the ions could be shuttled around the trap by adjusting voltages applied to the electrodes. However, ion heating during shuttling can affect the state of the qubit and shuttling times could become extensive as the chip size increases. These and other difficulties may arise in scaling a single chip to a large number of ions. To extend the quantum computer beyond a single chip, photon mediated remote entanglement of two ions (Moehring et al., 2007), one in each subsystem, can be used to establish a quantum link between two subsystems. Entanglement between ions in different traps (or subsystems) has been demonstrated before; however, the success probability of this probabilistic scheme scales as the square of the photon collection probability into a single spatial optical mode. A dramatic improvement in light collection is necessary to make this scheme useful for scaling quantum information processing. Single spatial mode collection is critical for efficient fiber coupling and thus mode overlap during photon interaction as well as maintaining the photonic qubit.

Due to limited light collection from an ion, state detection is currently the rate-limiting step in trapped ion quantum information processing within a single trap or subsystem. Prior to this work, ion hyperfine qubit states have been determined with high fidelity, but require lengthy detection periods to collect a sufficient number

of photons (Myerson et al., 2008). These detection times are long ($\sim 10^2$-$10^3\,\mu$s) compared with ion quantum gate times ($\sim 10^0$-$10^1\,\mu$s). Shorter detection times are critical to perform practical loophole-free Bell experiments at a single physical site (e.g., two systems at one university) because the measurement must be done faster than a photon can travel directly between the two systems.

1.4 Improving photon collection from single ions

Various practical constraints arise in trying to collect a large solid angle of the light emitted by a single trapped ion. To date, ions are typically trapped in a large (4-6 inch) ultra-high vacuum (UHV) chamber, and an imaging objective is placed outside a large (3-4 inch) front viewport. The trap is usually recessed in the chamber by $\sim$10 mm or more to minimize the effect of stray fields at the trapping site that originate from electrostatic charge buildup on the front viewport (an effect that is worse in the presence of ultraviolet light, which is often required for ion manipulation (Harlander et al., 2010; Wang et al., 2011)). Due to the total distance between the objective lens and the ion, a standard lens can typically collect only a few percent of the total light emitted by the ion. The surface ion traps that are growing in popularity because of their scalability make it difficult to cover a large fraction of the emission solid angle. The whole system must be designed to facilitate the use of optics for large solid angle collection.

Others have recently made progress in solving the light collection problem using microcavities (Trupke et al., 2005; Sterk et al., 2012), Fresnel microlenses (Streed et al., 2011; Jechow et al., 2011; Brady et al., 2011), and integration of fiber optics (VanDevender et al., 2010). These experiments have not encompassed hyperfine ion state detection, and it is unclear what fidelity and readout speed are achievable using these methods. A hyperfine ion qubit state detection fidelity of 99.77% in 400 μs (Myerson et al., 2008), the best result prior to this work, employed an

improved state classification process rather than increased light collection. An optimized strategy is required to determine the state, but ultimately it is critical to improve the contrast between the bright and dark states to maximize the detection fidelity and remote ion entanglement rate and minimize the ion state readout time.

We approach this problem in several ways resulting in varied benefits. In our first approach, we design an ion trap to be incorporated with an optical cavity such that the optical cavity mode was matched to an optical fiber at one end, which allows for high probability ($p = 0.3$) collection of emitted photons directly into the single mode fiber as required for strong spatial overlap during remote entanglement generation. This type of collection takes advantage of the Purcell effect of enhanced emission from the ion into the cavity mode, and the setup can work well for other interesting cavity quantum electrodynamics experiments. Although an optical cavity has many merits, among the difficulties are system integration, scalability, and sensitivity to external phenomena. An alternate approach is to design a surface ion trap (in a collaboration between Duke University and Georgia Tech Research Institute) to incorporate a micro-optic mirror with small radius of curvature ($\sim$100 μm) beneath the ion trapping location. This could provide a significant improvement in light collection, although a large fraction of the collected light cannot be easily matched to a single mode fiber and thus could help significantly more with ion state detection than remote entanglement generation. For our third system, we refit the vacuum chamber with a deeply re-entrant front window to accommodate a custom, large numerical aperture lens. The custom lens, located outside the vacuum chamber, was designed for high collection efficiency from the ion with an output mode matched to a single Gaussian mode for high fiber coupling efficiency.

The focus of this thesis is to demonstrate improved light collection from a single ion to a single spatial mode. We experimentally determine the viability of various methods for improving light collection from trapped ions using integrated optical

designs. The goal is to reduce the state detection time to be comparable with the time required for other ion quantum operations while maintaining a high state detection fidelity.

1.5 Dissertation organization

This thesis is organized as follows: the introduction to the topic and challenges addressed in this work constitute chapter 1. Chapter 2 discusses the ion, ytterbium, used in these experiments and everything necessary to trap and manipulate the ion as required for this work. Chapters 3, 4, and 5 include details of the setup and experiments for each of the three approaches mentioned above, and chapter 6 discusses applications and future possibilities for each of these methods.

Summary of My Contribution

I have written this document in a tone that emphasizes the experiments and results rather than precisely who was responsible for any given portion of the work. This section is meant to clarify the part of the work for which I was responsible.

Chapter 2 discusses the ion trapping setup, which started from nothing during my first year and has been constantly expanding during my time at Duke. I was responsible for a significant portion of the initial laser setup including laser stabilization, cavity assembly and alignment, optical alignments, optical measurements including choosing appropriate photodiodes, designing and assembling circuits and addressing noise problems. I built some of the lab control hardware and software, and made designs for and modifications to vacuum chambers. The setup changes over time and that implies that many people have the opportunity to redesign existing setups. Sometimes I was the first to design a setup, and other times I did one of the many redesigns. All of this leads to some vagueness in "ownership". I point this out to avoid offending later students who came along and improved on some of my

own designs, and to indicate that I do not feel ownership over the entire ion trapping setup, although I have at some time touched all of it.

Chapter 3 includes my discussion about the integrated fiber, cavity, and ion trap. The overarching design was done by others and published separately. I fabricated the ion trap chip (not the submount), and was the first person in our lab to trap in a linear microfabricated chip trap. I also did all of the characterization of the trap, and created most of the setup for doing that characterization. I worked on fabricating on the fiber tip and concluded that it was not compatible with any of our super-polishing processes.

The multiscale optics experiments in chapter 4 involve measuring the efficiency of light collection from a point source using a combination of custom etched micro-mirrors and a low numerical aperture (NA) lens. I did not do any of the fabrication in this section. I built and performed the experiment and analyzed the data. However, another graduate student contributed the Zemax simulations. I assembled the low NA lens, and GTRI fabricated the mirrors and ion trap. I adapted my vacuum chamber to accommodate the new trap chip, and did everything related to attempting to trap an ion with that chip.

Chapter 5 includes details about our high numerical aperture lens light collection. We purchased the lens, designed according to specifications that were determined by several group members. I prepared the chamber for the new chip, trapped, characterized the trap, and was responsible for the experimental portion (setup and data collection). Dr. Geert Vrijsen did the simulations (although I independently co-developed early versions of the simulations for my own understanding) and he also contributed the derivations of the ion scattering rates that appear in chapter 5 and the Appendix.

2

Ion Trapping and Experimental Setup

Basic ion trapping experiments require an ion trap in high vacuum, laser systems for cooling and manipulation, an imaging lens, and detector. All of these elements are chosen for high efficiency based on the choice of ion. There are several choices of atomic ion species that can be used as quantum bits. We chose our atomic species by considering the ratio of the time it takes to perform gates to the coherence time, the possible qubit states, and the complexity of states and their branching ratios. These determine their usefulness as a qubit, as well as practical requirements for optical pumping and repumping wavelengths. The sensitivity of the qubit to stray fields and state read-out fidelity are also important parameters. There are different ways in which ions can store quantum information; the common qubit types include optical, polarization, and hyperfine qubits. The main differences between these qubits are in the required procedures for state preparation and detection, their sensitivity to external fields, and the primary wavelength required for cooling and manipulation. The cooling wavelength is often far in the UV where the available laser power and optics are limited due to material scattering losses and absorption of UV light. For this work we have chosen $^{171}Yb^{+}$ as our qubit due to its reasonable manipulation

and pumping wavelength requirements and long coherence time. This chapter will discuss the properties of $^{171}Yb^{+}$ and the experimental setup for manipulating and detecting this species of ion.

2.1 The Ytterbium Ion

2.1.1 $^{171}Yb^{+}$ Qubit

We use single ytterbium isotope 171 (natural abundance 14.3%) ions to act as hyperfine qubits. $^{171}Yb^{+}$ has nuclear spin I = ½, which results in a relatively simple atomic level structure with two hyperfine ground states $|F = 0\rangle$ and $|F = 1\rangle$ with one and three Zeeman states, respectively. The states $|F = 0, m_F = 0\rangle$ and $|F = 1, m_F = 0\rangle$ are hyperfine clock states - insensitive to the magnetic field to first order - and can therefore have a very long relative coherence time (>15 minutes (Fisk et al., 1997)). A closed cycling transition which can be used for Doppler cooling the ion and state detection is resonant with 370 nm light, a wavelength which is long enough that suitable optics and optical fibers are available. A large hyperfine separation (12.6 GHz) between the qubit states allows for high fidelity state detection that will be discussed later in this document.

A neutral Yb atom can be photoionized by exciting it from the $^1S_0$ state to the $^1P_1$ state with 399 nm light, then another beam ⩽394 nm provides enough energy to free the electron to the continuum. The ion is Doppler cooled by applying light red detuned (typically 2-80 MHz) from resonance with the $^2S_{1/2}\,|F=1\rangle \leftrightarrow {}^2P_{1/2}\,|F=0\rangle$ cycling transition. A sideband at 14.7 GHz depopulates the dark $^2S_{1/2}\,|F=0\rangle$ state. The ion decays from the $^2P_{1/2}$ state to the long-lived $^2D_{3/2}$ state 0.5% of the time, but can be returned to the cycling transition with high probability by applying repump light resonant with the $^2D_{3/2} \leftrightarrow {}^3D[3/2]_{1/2}$ transition at 935 nm (see Fig. 2.1). Rare decay or collisions with background gases can move the ion from the $^2P_{1/2}$ or $^2D_{3/2}$ states to the $^2F_{7/2}$ state, and from there the it can be repumped to the cycling

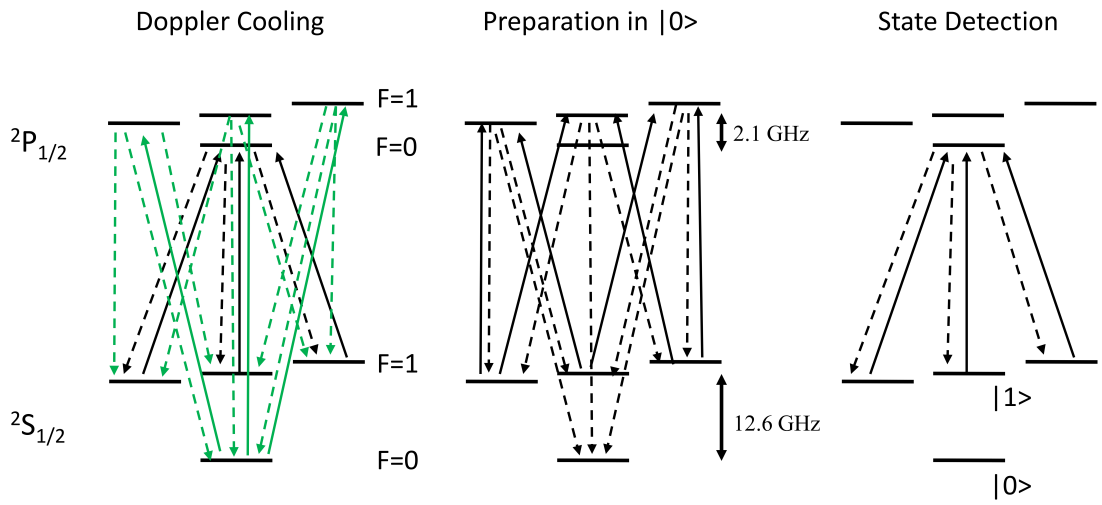

FIGURE 2.1: Yb level scheme for isotope 171 qubit. (left) Doppler cooling at 370 nm with some power in a 14.7 GHz sideband to repump from $|0\rangle$. (middle) Optical pumping to $|0\rangle$ by applying 2.1 GHz sideband with enough power to suppress the carrier signal. (right) State detection is performed with resonant light using a separate beam that does not pass through the EOMs. For all cases a 935 nm repump beam is used to recover the ion from the $^2D_{3/2}$ state.

transition with 638 nm light. Thus only four lasers are required for photoionization, trapping, Doppler cooling, state preparation, and state detection of ytterbium ions, all of which are available in the form of inexpensive laser diodes.

2.1.2 State Initialization and Detection

For this thesis, the qubit $|0\rangle$ state is defined as the $^2S_{1/2}\,|F=0, m_F=0\rangle$ state and the qubit $|1\rangle$ state is defined as the $^2S_{1/2}\,|F=1, m_F=0\rangle$ state. The qubit can be prepared in the $|0\rangle$ state by sending the 370 nm beam through an electro-optic modulator (EOM) to produce a frequency sideband of 2.1 GHz with strong modulation to suppress the carrier signal as observed with an optical cavity. This frequency difference is equivalent to the frequency difference between the $^2P_{1/2}|F=0\rangle$ and $|F=1\rangle$ states. The first positive sideband frequency is resonant with the $^2S_{1/2}\,|F=1\rangle \leftrightarrow {}^2P_{1/2}\,|F=1\rangle$ transition. From selection rules, the $^2P_{1/2}\,|F=1\rangle$ states will decay to

the qubit $|0\rangle$ state and the ${}^2\mathrm{S}_{1/2}\,|F=1, m_F=\pm 1\rangle$ states with equal probability. The ${}^2\mathrm{S}_{1/2}|F=1\rangle$ states will continue to be pumped to the P state, but the $|0\rangle$ state will not. Without light to repump the ion from the dark $|0\rangle$ state, the ion is pumped dark and thus initialized to the $|0\rangle$ state with high probability (error $<1\times10^{-4}$). The qubit can be rotated between the $|0\rangle$ and $|1\rangle$ states by applying a microwave field at 12.6 GHz, resonant with the hyperfine splitting between the ${}^2\mathrm{S}_{1/2}\,|F=0\rangle$ and ${}^2\mathrm{S}_{1/2}\,|F=1\rangle$ states.

The ion quantum state can be detected by measuring the fluorescence while applying 370 nm light resonant with the ${}^2\mathrm{S}_{1/2}\,|F=1\rangle \leftrightarrow {}^2\mathrm{P}_{1/2}\,|F=0\rangle$ transition. When the ion is in the $|0\rangle$ state, there is no resonant transition, and hence nominally no scattering. If the ion is in the $|1\rangle$ state, the light is resonant with the transition and the ion will typically scatter many photons before decaying to the dark ${}^2\mathrm{S}_{1/2}\,|F=0, m_F=0\rangle$ state. The detection process preserves the ${}^2\mathrm{S}_{1/2}\,|F=1\rangle$ state because decay to the ${}^2\mathrm{D}_{3/2}$ returns the qubit to the cycling transition (and also by selection rules). The scattering rate is affected by the intensity of the detection beam probing the ion and the detuning of the beam from resonance.

2.2 Ion Traps

A singly ionized atom can be trapped using a combination of radio frequency (RF) oscillating electric fields and static DC fields, commonly known as a Paul trap (Paul, 1990). The RF and DC fields are typically applied in 3D space on four rods aligned at the corners of a square, where the RF signal is applied to two diagonal rods, and DC voltages are applied to the remaining two rods (Fig. 2.2a). This configuration of RF with respect to the RF ground generates a 2D time-averaged confinement, and the DC rods can be divided into segments to provide confinement along the remaining axis parallel to the rods, forming a 3D trap. A quadrupole electric potential generated

by an RF signal at frequency Ω_{RF} is described by

$$\Phi(x,y,z,t) = U\frac{1}{2}(\alpha x^2 + \beta y^2 + \gamma z^2) + \widetilde{U}\cos(\Omega_{\mathrm{RF}}t)\frac{1}{2}(\alpha' x^2 + \beta' y^2 + \gamma' z^2), \quad (2.1)$$

where the possible solutions are restricted to $\alpha+\beta+\gamma=0$ and $\alpha'+\beta'+\gamma'=0$ by the requirement that the Laplace equation $\Delta\Phi = 0$ at any time t. The equation of motion due to this potential can be transformed to a Mathieu differential equation

$$\frac{d^2x}{d\xi^2} + \left[a_x - 2q_x\cos(2\xi)\right]x = 0, \quad (2.2)$$

where

$$\xi = \frac{\Omega_{\mathrm{RF}}t}{2},\ a_x = \frac{4q_{\mathrm{ion}}U\alpha}{m\Omega_{\mathrm{RF}}^2},\ q_x = \frac{2q_{\mathrm{ion}}\widetilde{U}\alpha'}{m\Omega_{\mathrm{RF}}^2}. \quad (2.3)$$

The solutions to the Mathieu equation are dependent only on a_x and q_x (Leibfried et al., 2003). For the ion traps discussed here, $a_x \approx 0$, and q_x is referred to as the Mathieu stability parameter q. Along $a_x = 0$, the stability regions become smaller with increasing q, making a small q value desirable (see stability q diagram in (Leibfried et al., 2003)).

The total trap potential can be calculated by summing the ponderomotive pseudopotential and the static DC potential. The width of the harmonic potential (or trap secular frequencies) and depth of the potential null can be tuned with the magnitude of the electric field applied and spatial position of the rods. We estimate the trap secular frequencies from trapping field simulations by calculating the eigenvalues of the Hessian of the total potential. The Hessian matrix is $\mathrm{H_{ij}} = m\omega_{\mathrm{i}}^2\delta_{\mathrm{ij}}$ for a 3D harmonic potential, where $\mathrm{i,j} = x, y, z$ and ω_{i} is the trap secular frequency in a given direction.

Projecting a quadrupole trap onto a 2D surface approximately maintains the 3D harmonic ponderomotive pseudopotential, and a null is formed some distance above

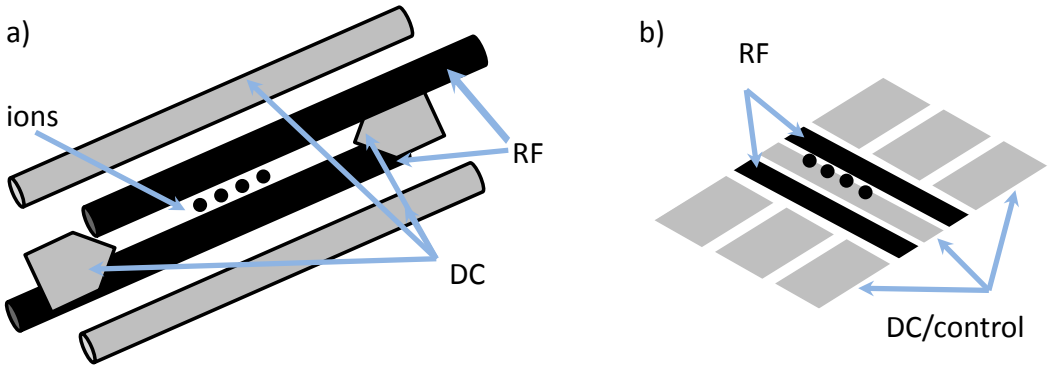

FIGURE 2.2: a) A quadrupole trap consisting of two RF rods, two DC rods, and two DC end caps. The ions are trapped in the center. b) An approximate projection of a) onto a two-dimensional surface, where the ions are trapped in a line above the surface.

the planar surface as shown in Fig. 2.2b. Two-dimensional surface traps are appealing because they can be microfabricated with reasonable repeatability (Stick et al., 2010) and are thus considered a scalable technology. Microfabricated traps are easily designed and modeled, and can be created in large quantities. Scalable surface trap designs generally suffer from shallow trap depths because all fields originate from a plane and decay with distance, combined with maximum voltage limitations imposed by small wires and thin insulating layers that are common to microfabricated structures. However, both planar and multi-layer traps have been successfully fabricated and show reasonable performance for very basic quantum computing operations (Seidelin et al., 2006; Stick et al., 2006). Various types of microfabricated surface traps are used for the experiments discussed in this thesis, and Table 2.1 summarizes the relevant parameters for these traps.

---

[1] Georgia Tech Research Institute, Atlanta, GA, USA

[2] Sandia National Laboratories, Albuquerque, NM, USA

Table 2.1: Relevant parameters for the microfabricated traps discussed in this thesis.

Origin	Ω_{RF}	V_{RF}	Trap Depth	Secular Freq./2π	q
Duke Glass Trap	37 MHz	200 V	270 meV	5 MHz	0.4
GTRI[1] Mirror Trap V2	22 MHz	150 V	60 meV	N.A.	0.2
SNL[2] Thunderbird	28 MHz	250 V	150 meV	2 MHz	0.2
SNL[2] HOA	24 MHz	260 V	550 meV	5.2 MHz	0.6
	37 MHz	200 V	140 meV	2.6 MHz	0.2

2.3 Helical Resonators

High voltage RF delivery is a significant problem in ion trapping due to the high power required and severe impedance mismatch between the RF generators (50 Ω) and the ion trap (surface traps are ∼10 pF). The community has found a unique solution in helical resonators. Helical resonators consist of a copper can with a thick copper wire coil inside that is grounded via direct soldering to the can at one end (Macalpine and Schildknecht, 1959), and have long been known to the radio community. The size of the can, number and diameter of coils in the wire and the length of the coil determine the inductance and capacitance of the resonator, which ultimately determine the resonant frequency and characteristic impedance. A helical resonator uniquely solves several problems simultaneously: first, it provides an impedance match between the 50 Ω output of the RF generator and the large capacitance load that is the trap. Secondly, it filters the RF signal with a quality factor related to the construction, and finally, it is a quarter-wave transmission line that provides an additional voltage amplification stage, not exactly known, but estimated as (Olmschenk, 2009)

$$V_{\mathrm{RF}} = \varepsilon \sqrt{P_{\mathrm{RF}} Q}, \tag{2.4}$$

where P_{RF} is the input RF power, $\varepsilon \approx 30$ is an estimated geometric factor applicable to most resonators made in our lab, and Q is the loaded quality factor of the resonator. The final resonator was designed by optimizing these parameters over practical con-

straints (e.g., wire gauge), and estimating the additional impedance load of the trap based on the capacitance measured across the RF feedthrough pins. The reflected power coupled back through the coupler gives information about the resonant frequency and the quality factor of the helical resonator. The quality factor, Q, of the resonator is measured to estimate the RF power required to generate the desired trap RF voltage. The Q is measured as the center frequency and lowest reflection point, f, divided by the width, Δf, which is measured on a spectrum analyzer as 3 dB down from maximum reflection on either side of the minimum reflection dip (resonant) frequency. There is not a good way to measure the RF voltage directly because of the capacitive load of the trap ($\sim$10 pF). An attempted measurement loads the circuit and hence changes the resonant frequency, Q, and impedance matching to the trap. Thus, we rely on our estimate to calculate the correct RF voltage and can only verify the actual RF power after we trap an ion and measure the trap secular frequencies, which are sensitive to the RF voltage.

2.4 Vacuum Assembly

A top-down view of the vacuum assembly is shown in Fig. 2.3. An ion pump and sheets of non-evaporable getter pump continuously pump down the chamber and a titanium sublimation (Ti:sub) pump is fired as necessary to maintain a pressure $<$ 1.9×10^{-11} Torr. The chamber is vented with nitrogen and continuously purged during chamber modifications, whenever possible. The ion trap faces the front support structure, which is used to mechanically attach magnetic field coils, a microwave horn, and other necessary items. A standard 98-pin ceramic pin-grid array (CPGA) chip carrier is mounted in the standard 6-inch octagon ultra-high vacuum (UHV) chamber facing a large anti-reflection (AR) coated fused silica (FS) window. DC electrical connections (including connections for Yb ovens) are fed through a 51-pin micro-D connector. The RF signal is allotted a separate feed-through on the opposite

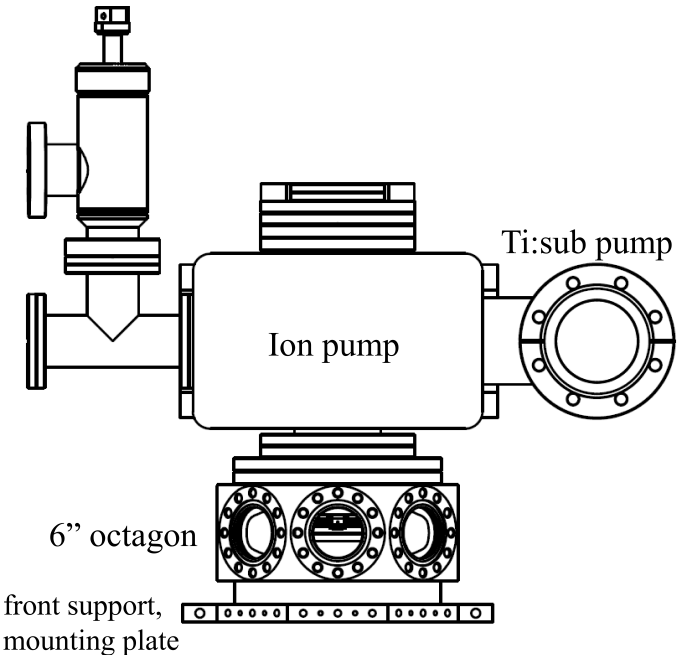

FIGURE 2.3: Top-down view of the vacuum chamber. A 6 in. octagon is attached to an ion pump with a 5-way cross. The system is vented with nitrogen via the all-metal valve (top left) and continuously purged during chamber modifications.

side of the chamber to reduce RF pickup on DC lines, and to maintain desired optical access to the ion trap. AR coated FS windows are installed on the remaining ports of the octagon, which provide optical access to the trap.

Before mechanical hardware parts are assembled in the chamber, all parts are thoroughly cleaned in an ultrasonic acetone bath for $\geqslant$30 min., followed by an ultrasonic isopropanol bath for $\geqslant$10 min. The acetone bath is repeated until the acetone is still clear after 30 min., and the parts appear clean and free of dirt and grease. After the ultrasonic cleaning, the parts are pre-baked in clean UHV grade aluminum foil at 250-300 °C for 24 hours. While the parts are still warm they are moved directly to nitrogen purge storage for 1-2 days if they are not used immediately. Before the hardware is installed, it is dipped in trichloroethylene (TCE) to remove any lingering grease and rinsed with IPA, then blown dry with a house nitrogen gun. All

vacuum assembly is performed in a class 1000 cleanroom facility (class 1000 allows a maximum of 1000 0.5 μm or larger particles per cubic foot of air).

The assembled chamber is baked under vacuum in a large oven, and the temperature is ramped at 0.5 °C/min to 200 °C and held for several days (typically 5 days) to help remove water and other contaminants. During the bake, the chamber is initially pumped by a turbo pump backed by a leak detector that contains an internal turbo pump backed by a roughing pump. Typically the ion pump is turned on when the chamber pressure reaches $\sim 10^{-7}$ Torr. While the oven is still at 200 °C, once the pressure is low enough that the turbo pumps do not aid in reducing the pressure (high 10^{-8} Torr range), the all metal valve is hand-tightened to close off the chamber. The bake continues until the pressure stabilizes over a 12-24 hr time period, usually a pressure in the low- to mid- 10^{-8} Torr range. The oven is ramped down at <0.5 °C. At room temperature, the all-metal valve is closed to the previous torque. The turbo pumps are turned off, and as the foreline is vented the pressure is monitored and the all-metal valve is tightened a few in.-lbs. at a time until no pressure increase is observed (this is a very fast process; if the all-metal valve leaks, the pressure rises very quickly when the line is vented). After the pressure has stabilized, a titanium sublimation (Ti:sub) pump is fired at the recommended current for 2 minutes. This is repeated every 30-60 min. until the pressure drops below the 1.9×10^{-11} Torr. The resulting room temperature pressure is less than 1.9×10^{-11}, the minimum pressure readable by our ion gauge.

The lasers are aligned through the side windows of the chamber, parallel to the surface of the planar ion trap (discussed in Chapter 3). The 370 nm beam is aligned across the chip at 45° to the RF rails, and the 399 nm and 935 nm beams are overlapped using a dichroic mirror and aligned to roughly overlap with the 370 nm beam traveling in the opposite direction. When present, the 370 nm detection beam is aligned parallel to the Doppler cooling beam and travels beneath it by a few

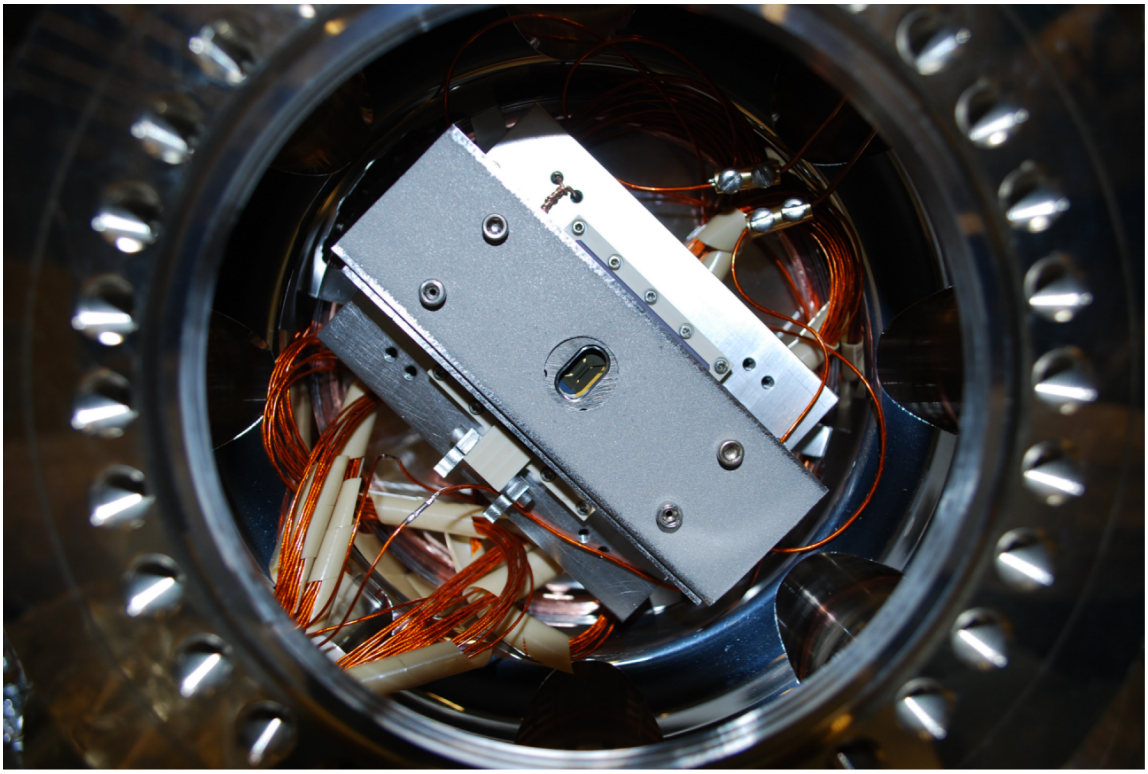

FIGURE 2.4: Ion trap assembly in vacuum chamber. The slotted ground shield design is used for all experiments except for the trap discussed in chapter 3. The slotted ground shields are covered by a sheet of non-evaporable getter on the front and back side.

millimeters; a focusing lens is used to overlap the parallel beams at the ion location. Figure 2.4 shows the final assembly in the octagon.

2.5 Laser Systems

Highly stabilized laser systems are required for trapping and manipulating ions. External cavity stabilized diode lasers (ECDLs) are used to provide light at 370 nm, 399 nm, and 935 nm. The external cavity in Littrow configuration is used to ensure single frequency operation and for stabilization and wavelength tuning over a several nanometer range. An optical grating is used to provide wavelength selective feedback to the diode, where the frequency dependent gain is determined by the combination

of modes supported by the internal cavity of the diode laser, the gain medium and the external cavity. By tilting the grating angle in conjunction with changing the current supplied to the diode, the lasing wavelength can be tuned over the range of several gigahertz without experiencing mode hops, that is, frequency hopping from one supported mode to the next supported mode. The temperature is stabilized and adjusted using a thermoelectric cooler (TEC). The 370 nm laser used in these experiments has a free space lasing wavelength of 371 nm at room temperature and must be cooled to ∼-10 °C to achieve optimal gain and stable lasing at 370 nm. The laser box is slowly nitrogen purged to maintain a dry environment and prevent water condensation on the diode, and the base is water cooled to provide a heat sink for the TEC.

Optical feedback from an external cavity along with temperature stabilization provide a narrow laser linewidth (∼1 MHz), but the narrow line drifts over time. To prevent this, the lasers must be locked to a more stable reference such as a wavelength meter or spectroscopy setup. Our wavelength meter (Toptica High Finesse, WSU-10) can be used to stabilize the frequency of several lasers simultaneously to tens of megahertz, but hyperfine spectroscopy is needed for accurately calibrating the wavemeter and stabilizing the Doppler cooling laser frequency as required for our experiments. The Doppler cooling and detect beams used in our experiments are locked indirectly to a Rubidium cell via feedback from a transfer cavity. To accomplish this, light from an additional ECDL at 780 nm is passed through a fiber EOM to produce a frequency tunable sideband that can be used for Rubidium spectroscopy. The laser (carrier signal) can be locked at any frequency that is less than 20 GHz detuned from a rubidium transition. The first negative sideband from the EOM is used to generate a Doppler-free saturated absorption spectrum and the feedback is used to lock the laser to a hyperfine line of rubidium using a Pound-Drever-Hall (PDH) scheme (Pound, 1946; Drever et al., 1983) which has the benefit of being

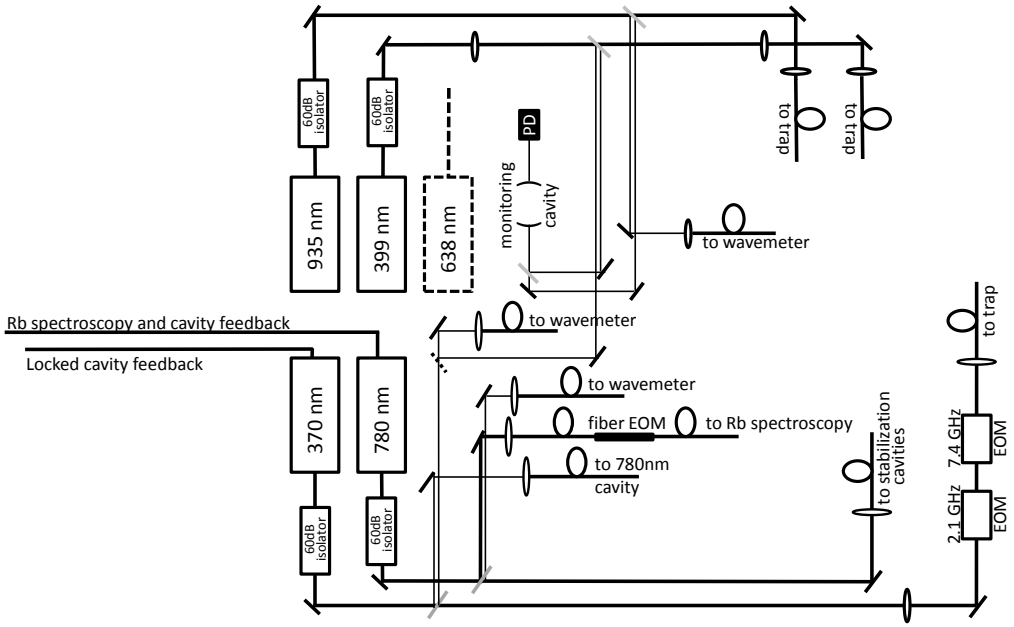

FIGURE 2.5: Optical setup for trapping and manipulating ytterbium ions. Gray surfaces denote mostly transmissive windows for extracting two weak beams from the main beam path.

robust against intensity fluctuations.

An optical cavity is used to lock the frequency of the 370 nm laser with respect to the 780 nm laser. The ability to tune the 780 nm laser by a free spectral range allows one to lock the 370 nm laser at the ion transition. The transfer cavity is stored in vacuum because the dispersion of air is large and minimal changes in temperature, pressure or humidity would cause shifts of tens of megahertz in a transfer lock between the two wavelengths. The drawback to this tranfer cavity locking method is that we have noticed decay in the UV optical coatings over time, similar to that described in Ref. (Sterk et al., 2012), that results in a reduced error signal for locking.

Another free-space cavity is used to monitor the modulation of the 370 nm laser by each of the bulk UV EOMs. The other lasers are monitored with an additional broad-band coated free-space optical cavity.

Optical isolators are placed in the beam path of each laser, as close to the laser output as possible, to prevent frequency destabilization due to optical feedback from back reflections originating downstream in the optical path. To determine the effectiveness of the isolator, the laser frequency is tuned by changing the voltage applied to the piezoelectric transducer (PZT) used to fine tune the position of the optical grating used for external cavity feedback to the laser diode. The laser output is monitored on an optical cavity to ensure that the frequency tuning is smooth over a single stable mode-hop free tuning range. If the frequency tuning is not smooth and the signal appears to "catch" repeatedly at the same frequency, then a lens tissue is placed before the isolator and the experiment repeated. If the effect is reduced or absent, the lens tissue is used to check the influence of any possible back reflections by waving it in the optical path so that the tissue is between only a single retro-reflector and the laser at a time. After the optics are realigned so that the back reflection is gone, the frequency tuning sweep as monitored on the cavity appears to be smooth.

Acousto-optic modulators (AOM) (IntraAction, Inc.) are used for fast, computer-controlled power switching of the 370 nm cooling and detection beams. The beam position relative to the input RF control signal as it passes through the AOM is a compromise between an undesirable delay in switching that is greater as the beam is moved away from the input power source, and the extinction between the zero and first order that is poor if the beam passes too closely to the input source. The measured delay for the detection beam AOM is $\sim$1 µs with the beam center passing a few millimeters from the input source edge of the window. A schematic of the current optical setup is shown in Fig. 2.5.

An FPGA controls the beam power switching via AOM signal switching, EOM

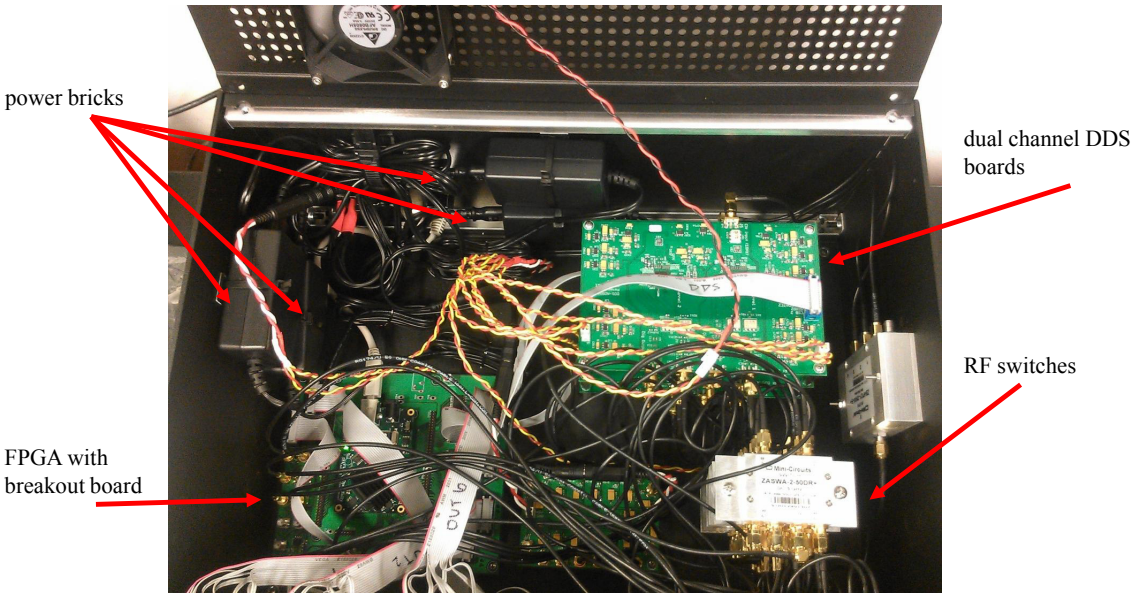

FIGURE 2.6: A main control box that I built for our quantum information experiments. This box contains a control FPGA for recording photon counts, generating power switching signals, and setting RF frequencies and power levels; direct digital synthesizer (DDS) RF sources; RF switches; and power supplies.

sideband frequencies, resonant microwaves used for flipping the qubit state, recording the PMT signal, and any other time critical events. A homemade box for this setup is shown in Fig. 2.6. Timing control is critical for real-time experiments, where each step takes $10^1 - 10^3\,\mu$s. Recording the time-of-arrival of PMT events to within the timing bin of the FPGA (20 ns) is also critical for our ion state detection experiment discussed in chapter 5.

2.6 Generic Light Collection with an Off-the-Shelf Lens

Photons emitted by the ion are, in general, collected outside the vacuum chamber with $f/1.9$ imaging optics consisting of 5 lenses with total object magnification of -10. $f/1.9$ corresponds to coverage of 1.6% of the total solid angle of light emitted by the ion. The photons travel $\sim$1 meter after the lens to an electron-multiplied charge-

coupled device (EMCCD) camera (Andor UV-enhanced iXon). A 6 nm bandpass filter at 370 nm is attached to the camera to filter out detuned background photons. For more sensitive operations, such as measuring the emission lineshape, fine tuning the laser pointing, or detecting the state of the ion, the emitted photon count rates are monitored on a photomultiplier tube (PMT) detector after passing through an iris and bandpass filter.

3

An Integrated Ion Trap and Optical Cavity with Direct Fiber Coupling

Free-space collection of the light emitted by the ion requires coverage of a large fraction of the ion's solid angle and can be geometrically difficult. One can still efficiently collect the emitted light by covering a limited solid angle of the ion and taking advantage of enhanced spontaneous emission when the ion is trapped in an optical cavity (Purcell, 1946). When the atom-cavity coupling is higher than both the cavity loss rate and the spontaneous emission rate, the field builds up in the cavity. The optical coatings can be carefully designed to have the primary source of cavity decay be transmission through one of the mirrors so that the light from the ion can be collected outside the cavity.

The design discussed in this chapter uses a planar-concave optical cavity as described above for the purpose of efficiently collecting the emission from the ion. With our scalable design integrating a surface ion trap with an optical cavity that is Gaussian mode matched to a single mode fiber, we expect high photon collection from a single trapped ion. In this chapter I discuss the design, fabrication and characteriza-

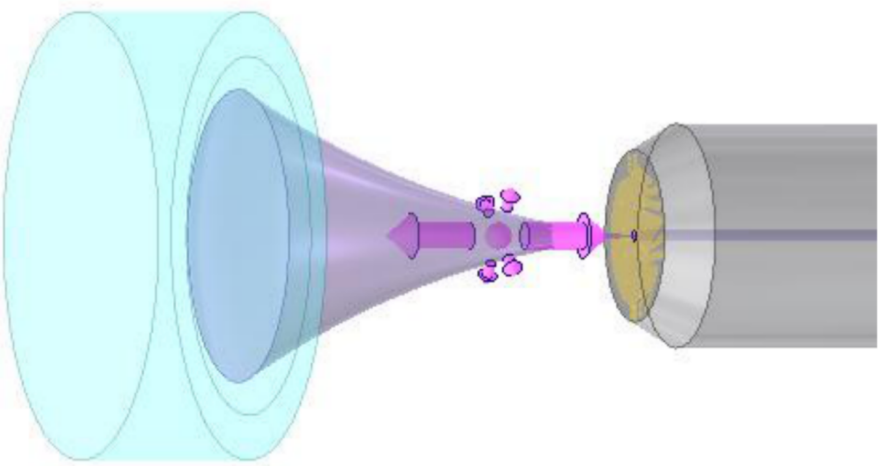

FIGURE 3.1: Design for integrated trap and optical cavity with direct fiber coupling. The single-layer trap is fabricated on the surface of a flat fiber tip, and the cavity is closed with a conventional curved mirror.

tion of the ion trap on a flat, uncoated substrate that is compatible with the cavity geometry described in the following section, as well as the progress in fabricating the trap on a ferruled fiber tip.

3.1 An Integrated Optical Cavity and Ion Trap for Improved Collection of Photons

The ion trap studied in this experiment is designed for integration with an optical cavity for direct coupling of emitted light into an optical fiber, as shown in Fig. 3.1a (Kim and Kim, 2009; Kim et al., 2011). The optical cavity is formed between a concave mirror and a flat mirror, which is realized by the high reflectivity coated tip of a fiber on which the surface ion trap is fabricated. The planar-concave cavity is aligned in a near-concentric geometry where the length of the cavity is almost equal to the radius of curvature of the concave mirror, such that the beam waist of the cavity mode lies on the flat mirror. An important cavity parameter is the cavity finesse

$$\mathcal{F} = \frac{\Delta\nu}{\delta\nu} \approx \frac{2\pi}{\mathcal{L}}, \tag{3.1}$$

where $\Delta\nu$ is the cavity free spectral range (FSR, the distance between peaks), $\delta\nu$ is the cavity linewidth, and $\mathcal{L}$ is the total cavity loss. The cavity field decay rate can be written as

$$\kappa = \pi \left(\frac{\mathrm{FSR}}{\mathcal{F}} \right). \tag{3.2}$$

For this cavity geometry, maximum coupling between the dipole moment of the ion and the cavity field is achieved when the ion height equals the Rayleigh length of the cavity mode (Kim et al., 2011). The Purcell enhancement factor for the ion in the cavity is $2C + 1$ (Mundt et al., 2002), where $C = g^2/(\kappa\Gamma)$ is the cavity cooperativity parameter, which is the ratio of atom-cavity coupling g and system dissipation ($\Gamma = 2\pi \times 19.6\,\mathrm{MHz}$ the linewidth of the atomic transition). With our design conditions, the cooperativity is given by

$$C = 3\mathcal{F} r_B \lambda^2/(\pi^3 r_{ion}^2), \tag{3.3}$$

where $\mathcal{F}$ is the finesse of the cavity, r_B is the branching ratio of the ion's excited state into the final state of interest, λ is the wavelength of the emitted photon, and r_{ion} is the radius of the cavity mode at the location of the ion (Kim and Kim, 2009). Compared to conventional cavity QED designs where the beam waist of the cavity mode is 20-30 μm (Guthohrlein et al., 2001; Ritter et al., 2012), the beam waist in our design is approximately 2.4 μm. This small mode waist occurring at one end of the cavity allows the cavity be long (5 mm) and yet still have a very small mode radius at the ion (3.4 μm). The effective cavity mode volume is very small for our cavity, and in our case is given by

$$V_{\mathrm{eff}} = \frac{1}{4}\pi r_{\mathrm{ion}}^2 L, \tag{3.4}$$

where r_{ion} is the beam radius at the location of the ion and L is the cavity length. The small mode volume allows for a high cooperativity with much lower finesse, and

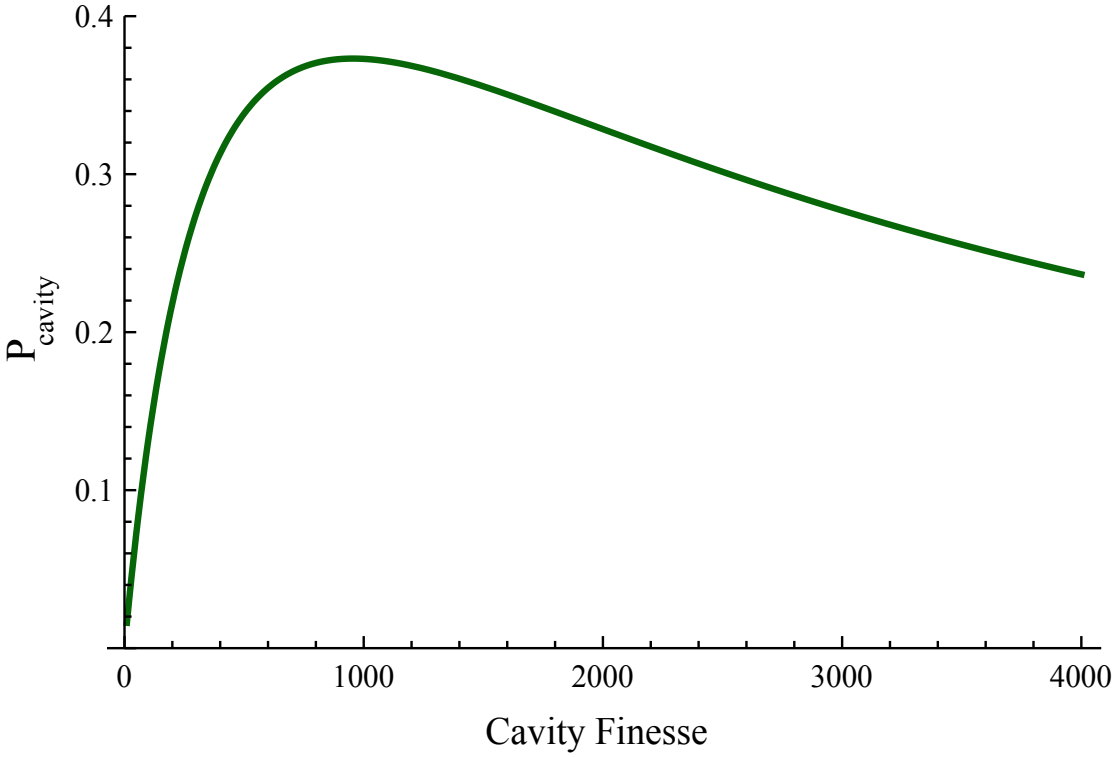

FIGURE 3.2: Probability to collect an emitted photon from the cavity as a function of cavity finesse. Low finesse indicates large losses and low atom-cavity coupling, which gives a small probability to collect the photon via desired transmission due to other cavity losses and low probability for the photon to have been emitted into the cavity mode. As the finesse is increased, the probability to collect the photon into the fiber decreases as the photon will instead be exchanged between the cavity and the atom and can be lost by spontaneous emission outside the cavity.

allows some mirrror loss in the form of transmission through the output coupling mirror. The atom-cavity coupling is

$$g = \left(\frac{\Gamma 3\pi c^3}{2V_{\text{eff}}\omega^2} \right)^{1/2}, \tag{3.5}$$

where ω is the ion transition frequency. We can optimize the light collection with critical damping, which for our cavity occurs when $g = \kappa$. Table 3.1 summarizes the parameters for our cavity.

Table 3.1: Cavity design parameters for our integrated fiber-cavity.

Parameter	Variable Name	Value
Mode waist	$w_\circ$	$2.4\,\mu\text{m}$
Cavity length	L	$5\,\text{mm}$
Ion height	z_{ion}	$50\,\mu\text{m}$
Beam radius at ion	r_{ion}	$3.4\,\mu\text{m}$
Atom-cavity coupling	g	$2\pi\times 18\,\text{MHz}$
Mode volume	V_{eff}	$4.6\times 10^{-5}\,\text{mm}^3$

The probability for an excited atom to decay into the cavity mode and for that photon to leave via the cavity decay is

$$P_{\text{cavity}} = \left(\frac{\kappa}{\kappa+\Gamma/2}\right)\left(\frac{2C}{2C+1}\right), \tag{3.6}$$

where the first term is the probability that the decay is from the cavity, and the second term is from the Purcell enhancement. This probability is shown in Fig. 3.2 as a function of the cavity finesse. A low finesse indicates large losses and low atom-cavity coupling, which gives a small probability to collect the photon via desired transmission due to other cavity losses and low probability for the photon to have been emitted into the cavity mode. As the finesse is increased, the probability to collect the photon into the fiber decreases as the photon will instead be exchanged between the cavity and the atom and can be lost by spontaneous emission from the ion into free space (outside the cavity). The total probability to collect the photon into the fiber is also a function of the optical mode matching between the fiber and the cavity ε and is given by

$$P_{\text{fiber}} = \left(\frac{\kappa}{\kappa+\Gamma/2}\right)\left(\frac{2C}{2C+1}\right)\left(\frac{T_f}{T_f+\mathcal{L}'}\right)\varepsilon, \tag{3.7}$$

where first two terms are from P_{cavity}, and the third term is the fraction of cavity loss that is transmission through the fiber mirror T_f with total cavity loss being

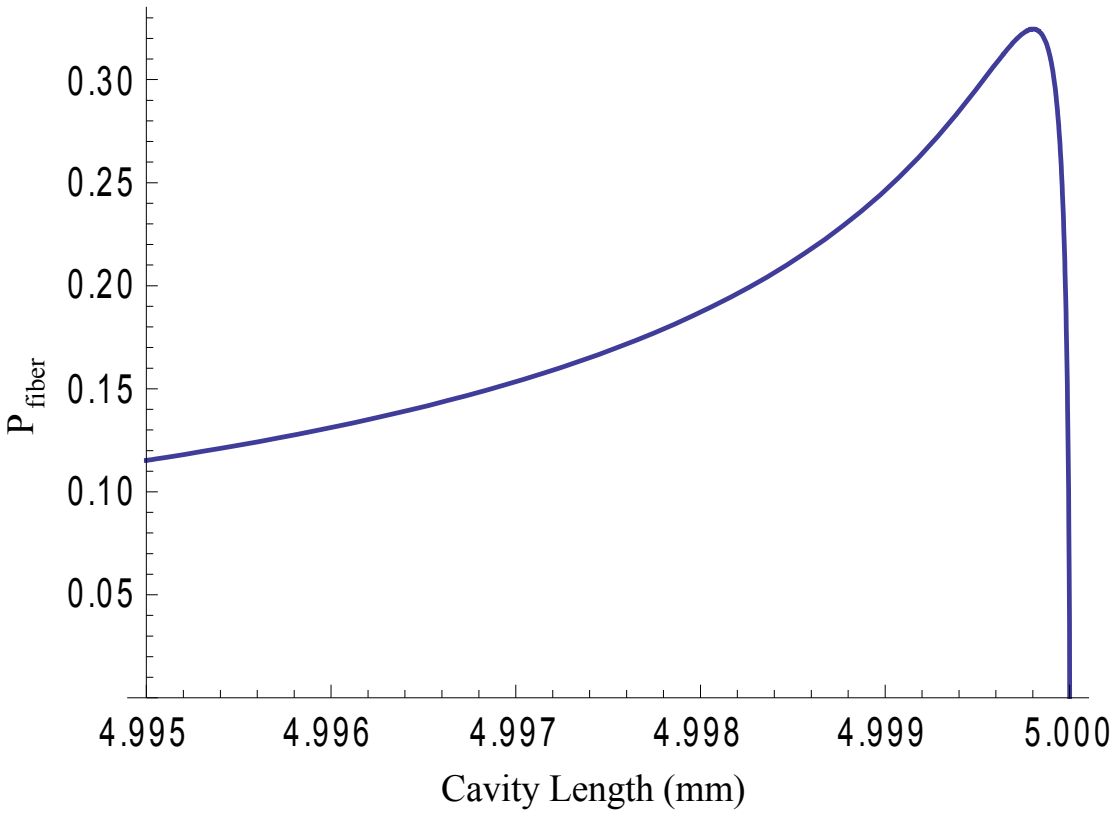

FIGURE 3.3: Probability to collect an emitted photon into the fiber as a function of cavity length. The Gaussian mode matching between the fiber and cavity changes rapidly with cavity length due to the increasing beam diameter as the cavity length decreases.

$\mathcal{L} = T_f + \mathcal{L}'$. As the cavity length is shortened, the mode size on the flat mirror and fiber face increases, decreasing the Gaussian mode overlap. The combined probability to collect the photon from the cavity and into the fiber as a function of the cavity length (assuming a mirror radius of curvature of 5 mm) is shown in Fig. 3.3.

Finally, our free design parameter is the cavity loss. Based on our simulations and the availability of high reflectivity coatings at 370 nm, we choose our mirror characteristics to maximize the light collection into the fiber. We expect to collect up to 30% of the emitted photons into the optical fiber mode with this design (Kim et al., 2011).

3.2 A Custom Ion Trap for Fiber-Cavity Integration

3.2.1 Custom Trap Design

The planar mirror in the cavity-integrated design will consist of a single mode optical fiber tip coated for high reflectivity with an ion trap fabricated on top. The ion trap was designed to have a simple geometry to maximize trap potential depth and rely only on a simple fabrication process in order to minimize damage to the highly reflective, super-polished mirror surface (Herskind et al., 2011). The basic design is a linear trap with a central grounded rail and two RF rails on either side, surrounded by segmented DC electrodes on the outside. The width of the gap between RF and DC electrodes was chosen to limit the risk of material breakdown at high RF voltage. To determine the minimum gap size, we fabricated a test structure with 1 μm thick Au on 20 nm Ti deposited onto a 0.5 mm thick fused silica substrate using electron beam (e-beam) evaporation. The test pattern had pairs of lines 30 μm wide and 2.36 mm long with varying gap widths of 3-8 μm. For each pair, 350 VDC was applied while monitoring the leakage current for 20 minutes. An increase in leakage current over this period acted as a non-destructive indication of material breakdown. Gaps $\geqslant 5$ μm had small, constant leakage currents (< 2 nA), and the smallest stable gap size of 5 μm was used for the RF electrodes on the trap. Away from the trapping zone, the gap was increased to avoid material breakdown along the extended length of the trap. A 3 μm gap was used between DC electrodes to avoid any additional exposure to the glass surface which could charge and cause drifts in the trapping potential. The central ground rail has a hole in the middle to accommodate the cavity mode, over which the ion will be trapped. The number of transverse DC control electrodes was determined by selecting the number of electrodes needed to easily position the ion in a harmonic well over the center of the optical mode. A symmetric pattern of three 150 μm wide adjustment electrodes in the center of the

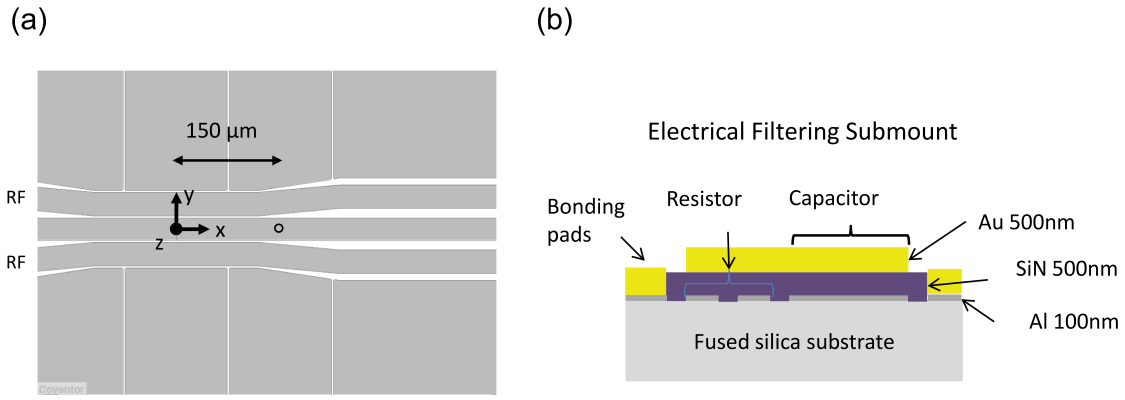

FIGURE 3.4: (a) The central layout of the trap. The center rail is ground with a hole for the cavity mode, and the electrodes outside the RF rails are DC electrodes with ∼150 µm pitch. (b) The cross-section of the submount, integrated with RC filters. Resistors are fabricated on the first metal layer, consisting of 100 nm of Al. Silicon nitride (500 nm) is used as the dielectric layer, and a filter capacitor is created by a second metal layer consisting of 500 nm of gold.

trap was combined with wide outer electrodes, as shown in Fig. 3.4.

3.2.2 Ion Trap Simulations

The trap fields are simulated using a boundary element method simulation software (Charged Particle Optics, or CPO). Each electrode is independently simulated by assuming a 1 V potential and grounding all other electrodes. The field results from each electrode are summed and scaled independently in Mathematica to produce an overlapping field null at the desired trapping location while maximizing the trap depth. Secular trap frequencies are estimated from the eigenvalues of the Hessian of the total trap potential. Figure 3.5 shows the contour map of the trapping potential in the y-z plane. The RF electrode width and separation were determined by compromising between creating a deeper trapping potential and the height of the trapped ion. The final solution has RF electrodes with equal width and center-to-center spacing of 58 µm, giving an ion height of 50 µm and a deep surface trap potential well of 270 meV in the weakest direction (z direction in Fig. 3.4a).

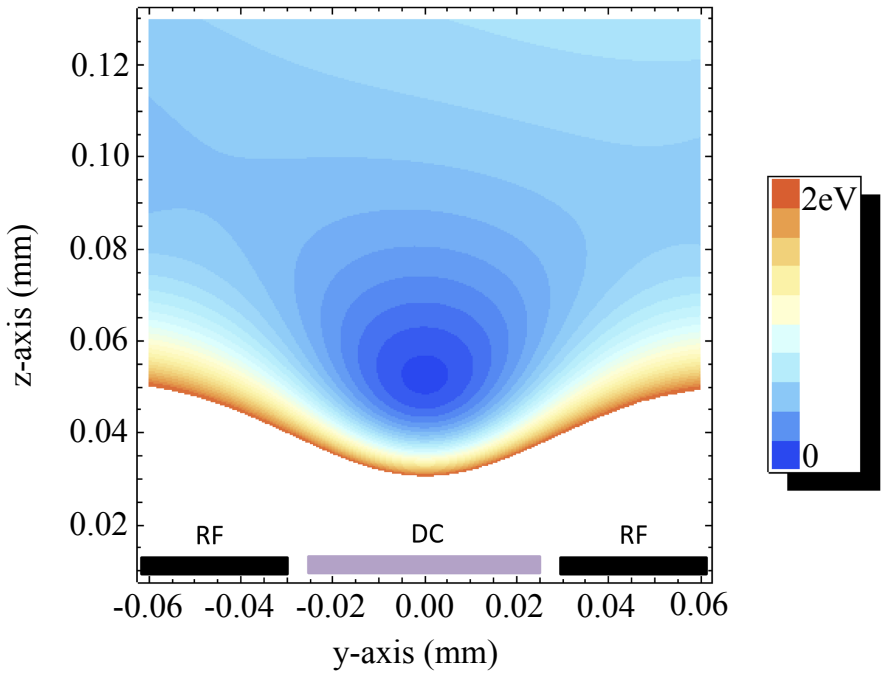

FIGURE 3.5: Simulation of the trapping potential for the fiber tip trap using boundary element methods. The plot shows a cross-sectional contour map of the trapping potential above the surface.

3.2.3 Ion Trap and Filter Submount Fabrication

The ion trap was patterned on a 0.5 mm thick quartz substrate using NRF016-D2 negative photoresist (JSR). To do this, the photoresist was spun on a 1 cm square substrate at 6000 rpm for 30 s, pre-baked on a hotplate at 90 °C for 60 s, exposed at 10.5 mW/cm^2 for 18 s, post-baked at 90 °C for 60 s and finally developed in MF-319 developer for 60 s. The sample was then coated with a 200 Å Ti sticky layer followed by 1,000 nm Au using e-beam evaporation, which was then lifted off in an acetone soak. In order to avoid RF pickup signal on the DC electrodes which could cause micromotion of the ion, the trap is mounted on a multilayer submount structure containing electrical filters with meandering trace resistors of $\sim 7.5\,\mathrm{k}\Omega$ and

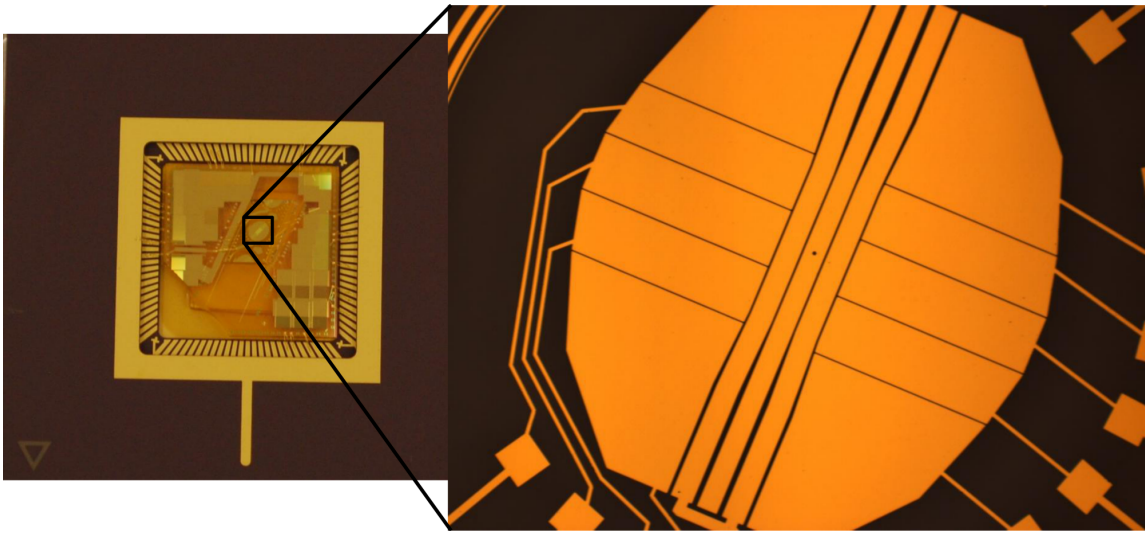

FIGURE 3.6: The trap, 1 μm thick Au on fused quartz, is glued to a submount and installed in a CPGA package.

133 pF parallel plate capacitors, providing low pass filters with cutoff frequencies near 160 kHz (Fig. 3.4b). The submount structure was fabricated by sputtering 100 nm Al on a 0.5 mm thick fused silica (FS) substrate. S1813 positive photoresist was patterned on the Al by spinning at 3000 rpm for 30 s, followed by a soft bake at 115 °C for 60 s, then exposed at 365 nm for 8.0 s at 10.5 mW/cm^2 and developed in MF-319 for 30 s. To etch the resistors in the bottom layer of Al, the patterned photoresist was hard baked for 120 s at 115 °C and the sample was etched using reactive ion etching (RIE) in an inductively-coupled plasma (ICP), with 10 sccm BCl_3, 20 sccm Cl_2, ICP power of 400 W and RIE power of 100 W. Immediately after the etch the sample was rinsed thoroughly to prevent continued etching of Al by the residual Cl on the surface. The photoresist dissolved in an ultrasonic acetone bath for 20 minutes. Next, an insulating dielectric layer of silicon nitride was deposited using a plasma enhanced chemical vapor deposition (PECVD) system with the following parameters: 650 mTorr, 50 W RF, 3% 750 sccm SiH_4, 40 sccm NH_3, 100 minute deposition time. These parameters resulted in 600 nm SiN film. The SiN film was etched by patterning

with NFR016-D2 under the same conditions used to fabricate the trap as described above. A process using RIE with 25 sccm SF_6 at 20 mTorr, with 100 W RF power for 90 seconds was run twice to completely remove the exposed SiN film. The final layer of Ti/Pt/Au was patterned using the same NFR016-D2 negative resist process, then 500 nm/100 nm/250 nm of Ti/Pt/Au were e-beam evaporated on the sample and lifted off in a 2 hour acetone soak, using ultrasonics when necessary.

After dicing to produce a rectangle approximately 2×4 mm, the trap substrate was epoxied to the submount structure using UHV-compatible epoxy and connected electrically via wirebonds. Several wirebonds were used on the RF signal to ensure that the wires did not melt or detach. A 6" ultra-high vacuum octagon was assembled with a standardized socket for a 98-pin CPGA package (Fig. 3.6). A small mesh sheet was mounted 2 mm over the trap to provide a local ground shield while allowing imaging of the ion from directly above the chip surface. The trap and submount were glued to the CPGA and mounted in the octagonal chamber so that the chip faces a large front window for optical imaging access; laser access was available at $\pm\,45^\circ$ to the RF rails, parallel to the trap surface via smaller side windows.

3.2.4 Experimental Setup and Trap Demonstration

The UHV chamber was baked at 200 °C for approximately one week to achieve a final pressure $< 1.9\text{x}10^{-11}$ Torr (the measurement limit for our ion gauge) at room temperature. A Yb oven consisting of a crimped 1 inch stainless steel tube with $\sim$3 mg of natural Yb loaded inside was aligned parallel to the surface of the trap, 1 mm above the trap surface pointed at the trapping location at an angle of -22.5° relative to the RF rails.

The 39 MHz RF trapping field are generated from a direct digital synthesizer (DDS) RF source which is amplified by 30 dB and applied to a helical resonator through a -20 dB coupler, and fed through the vacuum chamber to the trap. In this

setup,the resonator Q=50, and approximately 200 V were applied to the trap.

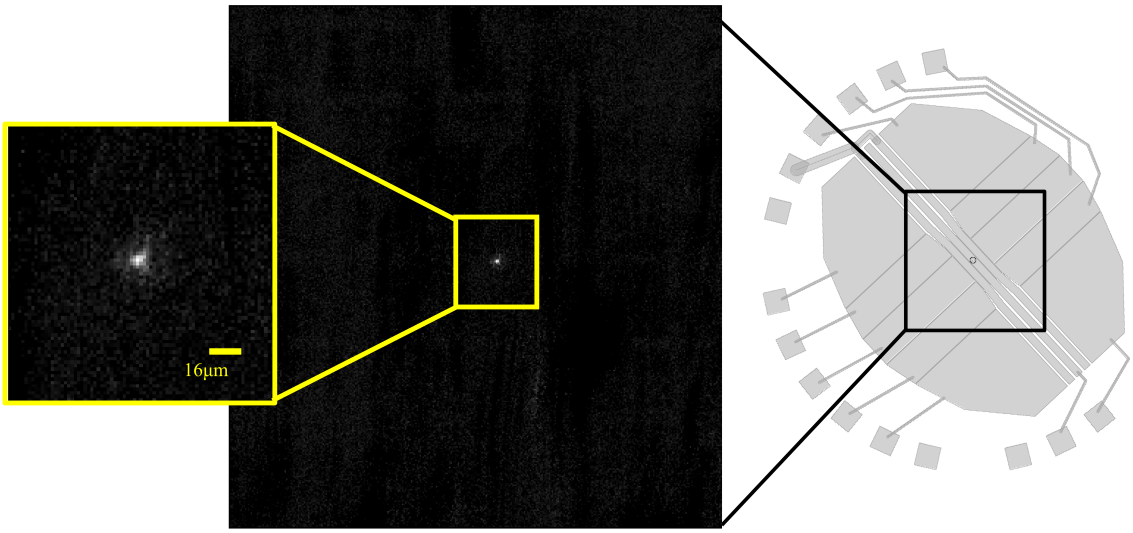

FIGURE 3.7: A trapped and Doppler cooled $^{174}Yb^{+}$ ion, trapped with the fused quartz trap imaged with a magnification of 10 on an EMCCD camera.

For this experiment, the photoionization beam at 399 nm and the re-pump beam at 935 nm co-propagate along the surface of the trap at 45° to the RF axis with a focused beam radius of 18 μm and 25 μm, respectively. The 370 nm Doppler cooling beam counter-propagates to these two beams with a beam radius of ∼16 μm (Fig. 3.7). The focus of each of the three beams is aligned to be at the center of the trapping zone.

Ytterbium isotope 174 was loaded into the trap by resistively heating the Yb oven which sends a flux of evaporated neutral Yb atoms over the trapping location. An ion is trapped when a neutral atom is photoionized as it crosses the trap field null location. By tuning the 399 nm laser frequency, we can isotope-select the ions being loaded into the trap. Also, surface electrode traps are typically not deep enough to hold hot ions, and other isotopes do not Doppler cool quickly enough to become trapped because of the large detuning of the Doppler cooling beam.

3.2.5 Trap Characterization

Figure 3.7 shows the image of a single $^{174}Yb^{+}$ ion trapped with the custom ion trap; the image is taken with an electron-multiplied charge coupled device (EMCCD) camera and imaged with a magnification of 10. The EMCCD detects the scattered photons from the ion during the Doppler cooling transition. Trapping times > 4 hours were observed with $4\,\mu W$ of 370 nm laser power for Doppler cooling. Other interesting trap properties include micromotion compensation, secular frequencies, and trap heating rate; all of these were characterized for this glass trap and are described in the following pages.

Micromotion of the ion is induced when the RF null of the trap does not coincide with the DC null. Because the DC trapping potential moves the ion away from the RF null, the ion will feel a finite RF field and its center-of-mass motion will be driven by the electrostatic force corresponding to the product of the field and the charge of the ion. There are three ways we observe and minimize the micromotion. In order of increasing sensitivity, they are: (1) measuring the lineshape of the ion, (2) using the RF modulation method, and (3) monitoring the photon count rate and looking for correlation with the RF phase. Measuring the lineshape of the ion is the first step in determining the magnitude of the micromotion. Under severe micromotion, the lineshape will be broad and distorted with bumps at integer multiples of the RF frequency, as shown in Fig. 3.8 (red), compared to a line shape after micromotion compensation (blue). The large amplitude of the ion's motion in all directions causes the photon count rate to be spread out in frequency as the ion sees a time-averaged variety of Doppler shifts.

For the RF modulation technique, the Doppler cooling beam is detuned to the red, reducing the scattering rate of the photons from the ion which are detected using a fast PMT for a predetermined duration. An increase in the amplitude of ion

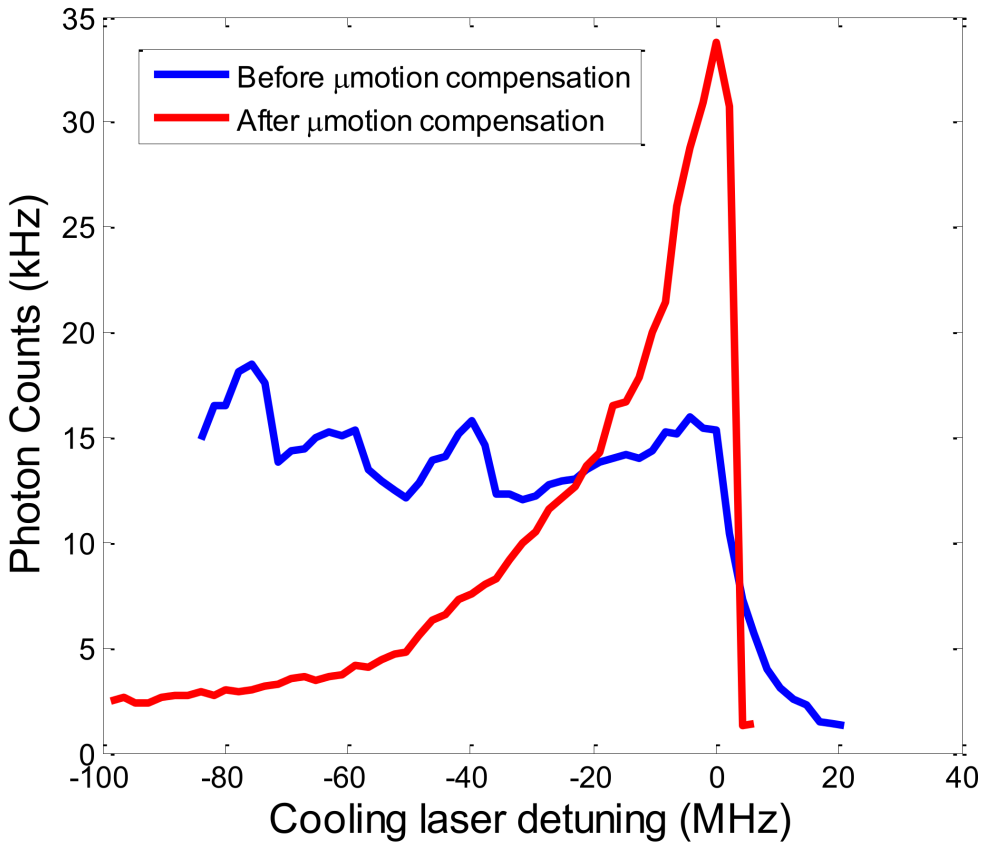

FIGURE 3.8: Lineshapes of the ion with severe micromotion (red), minimized micromotion (blue). Under severe micromotion, the lineshape is broad and distorted with bumps at integer multiples of the RF frequency due to resonant excitation.

motion due to micromotion will result in an increased scattering rate whenever the ion moves towards the cooling beam, bringing the detuned beam closer to resonance due to the Doppler effect. This allows one to detect sharp changes in the ion's motional behavior. An RF modulation signal close to the ion trap secular frequency (∼1-6 MHz) is introduced by mixing the modulation signal with the RF signal. With the modulation signal present, the curvature of the RF trapping potential is modulated, as shown in the inset of Fig. 3.9a. If the RF and the DC null coincide perfectly (ion sitting at the minimum of the RF null), the modulated potential does not induce any additional force on the ion. However, if the ion is sitting off-center with respect

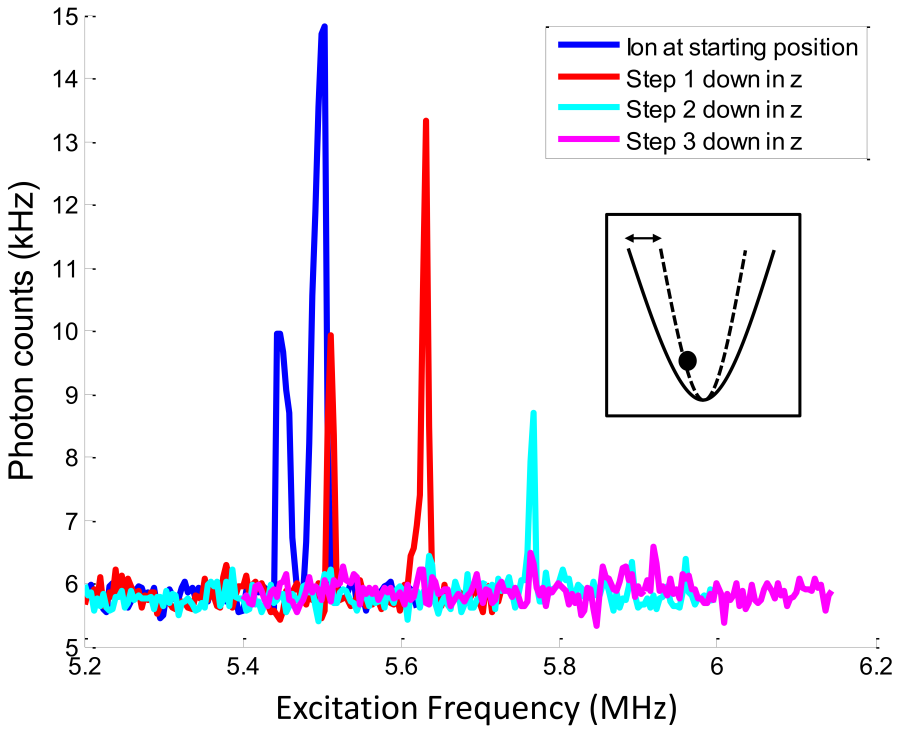

FIGURE 3.9: Measurement of trap frequencies and micromotion compensation using the RF modulation method. The peaks in the photon counts as a function of RF modulation frequency (horizontal axis) indicate resonant excitation of the micromotion of the ion, which can be suppressed (magenta curve) by fine-tuning the DC voltages on the electrodes.

to the RF null, the modulated potential will excite the ion motion at the modulation frequency. When the modulation frequency is equal to the secular frequency of the trap, the ion motion is resonantly excited, leading to a substantial increase in the photon scattering rate.

Figure 3.9 shows the process for minimizing the micromotion by adjusting the DC null to coincide with the RF null. As the frequency of the RF modulation signal is swept, the scattering rate of the ion for the red-detuned cooling beam features two peaks corresponding to the two secular frequencies of the trap (blue curve). We adjust the DC voltages on the control electrodes to move the DC null (in this case, so

that the null moves closer to the trap surface), and the peaks shift both in frequency (as the trap frequency indeed changes) and amplitude (as the DC null moves closer to the RF null) as shown in red and light blue curves. Finally, when the DC null coincides with the RF null, the peaks disappear as the ion motion is not excited by the RF modulation signal (magenta curve).

This RF modulation method also provides the measure of the secular frequencies of the ion trap. The trap frequency in secular approximation is proportional to $\omega_t \propto q_{\text{ion}} V_{\text{RF}}/m\Omega_{RF}$, where q_{ion} is the charge of the ion, m is its mass, and V_{RF} and Ω_{RF} are the amplitude and frequency of the RF voltage applied to the rails, respectively (Wineland et al., 1998). As we modify the DC voltages slightly from the values where the micromotion is minimized so that the resonant peaks are visible, the location of the peaks indicate the secular frequencies of the trap. We observe high radial trap frequencies of $> 2\pi \times 5\,\text{MHz}$, that increase as the RF power applied to the trap is increased. The frequencies increase at different rates with RF power due to the contributions from the DC fields which are anti-trapping in one direction and trapping in the other; this effect is predicted by our simulations.

Photon flux correlation with the RF phase is the most sensitive method for measuring the micromotion amplitude. This technique involves monitoring the photon arrival time with respect to the RF phase, which requires a short time bin with two synchronized input channels. A Picoharp 300 (PicoQuant) with 4 ps time bins records the time correlation measurements. Example data is shown in Fig. 3.10. In the presence of micromotion, the ion's scattering rate will increase with the half of the RF phase. This is because the ion is pushed by the RF field that is regularly flipping direction in time. During the phase of the RF that the ion is pushed in the direction that decreases the Doppler shift, the scattering rate increases. When no further decrease can be made in the correlation between the photon flux and the RF phase, the micromotion is said to be minimized.

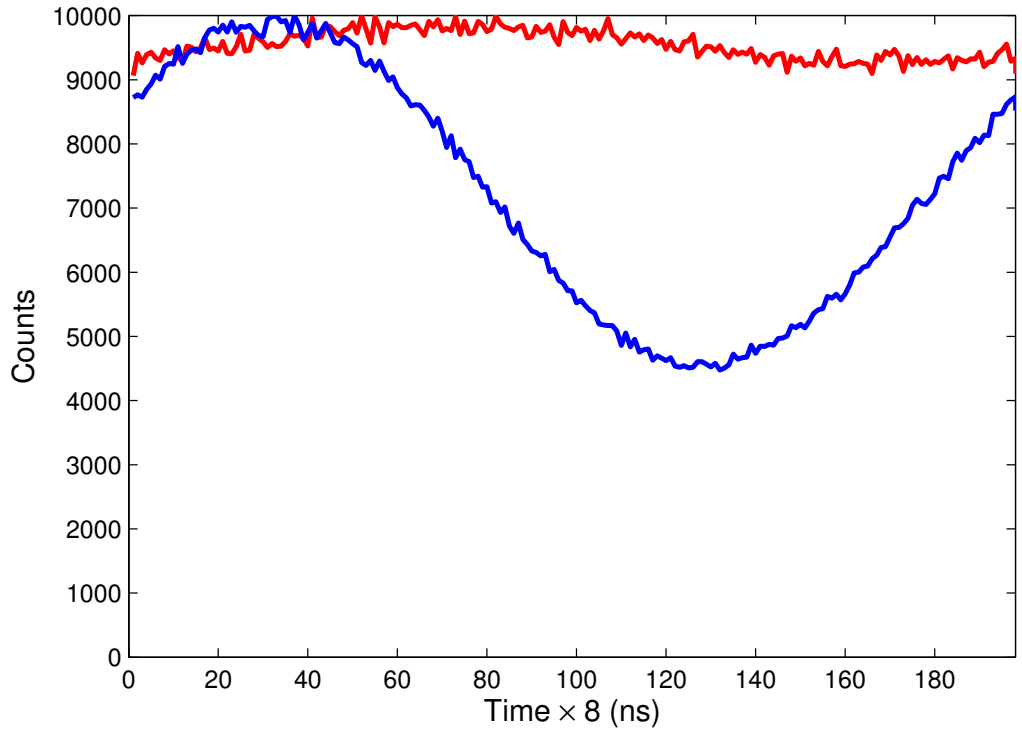

FIGURE 3.10: Micromotion of the ion can be detected by monitoring the photon flux correlation with the RF phase. When the ion is pushed in the direction of a blue shift at the RF frequency, the photon counts increase. During the part of the RF phase that the ion sees a red shift, the scattering rate decreases. The micromotion is defined as minimized when no further improvement can be made in removing the correlation. The blue curve shows micromotion left after improving the linewidth shape, and the red curve is taken after the micromotion has been minimized using the time correlation method.

After the micromotion was compensated, the trap heating rate was measured using the Doppler method described in Refs (Epstein et al., 2007; Wesenberg et al., 2007). In this method, the ion is first cooled to the lowest possible motional state by tuning the cooling beam close to resonance ($\sim$1-2 MHz). Under this condition, the fluorescence is maximized when the ion motion is minimized because increased motion will bring the ion further from the resonance with the cooling beam. The cooling beam is then turned off for a finite heating period, to allow the ion's motional modes to gain additional quanta of excitation. After the heating period, the cooling beam is

turned back on and the fluorescence is monitored until it stabilizes. If the ion heats substantially, the fluorescence drops significantly and recovers as the ion cools down. This process is repeated many times to generate a histogram (Fig. 3.11a) which is fit with a theoretical curve (generated from the convolution of the Maxwell-Boltzmann distribution accounting for different starting temperatures and the expected curve for the change in scatter rate with time) with the free parameter corresponding to the initial motional energy of the ion. Several histograms were collected for different heating periods using the Picoharp 300, and a linear fit through zero was used to infer the change in motional quanta per unit time without cooling. The linearly fit data in Fig. 3.11b show a heating rate of $\dot{\bar{n}}$ =16 quanta/ms. Typically the heating rate is converted to electric-field noise power spectral density (PSD) [$S_E(\omega)$] to compare between different systems and ion species (Hite et al., 2012; Mount et al., 2013) because it is normalized to the charge, mass, and trap frequency. The PSD is

$$S_E(\omega) = \frac{4m\hbar\omega}{q^2}\dot{\bar{n}}, \tag{3.8}$$

where m is the mass of the ion, ω is the trap secular frequency of interest, and q is the charge of the ion. The glass trap PSD-converted heating rate is $\omega S_E(\omega) = 3\times10^{-3}\,\mathrm{V^2/m^2}$, which is comparable to other systems with 50 µm electrode-ion spacing (Hite et al., 2012).

3.3 Fabrication on a Fiber Tip

Fabrication of the surface trap on an HR coated fiber tip is essential to our integrated cavity-trap design. Single-layer gold can be patterned by preparing negative patterned photoresist on the desired surface, followed by line-of-sight evaporation. The excess metal can be lifted off by soaking the sample in acetone.

A microscope was adapted for exposing the fiber tip by introducing a UV LED source through the eyepiece socket, converting the sample stage to a photoresist

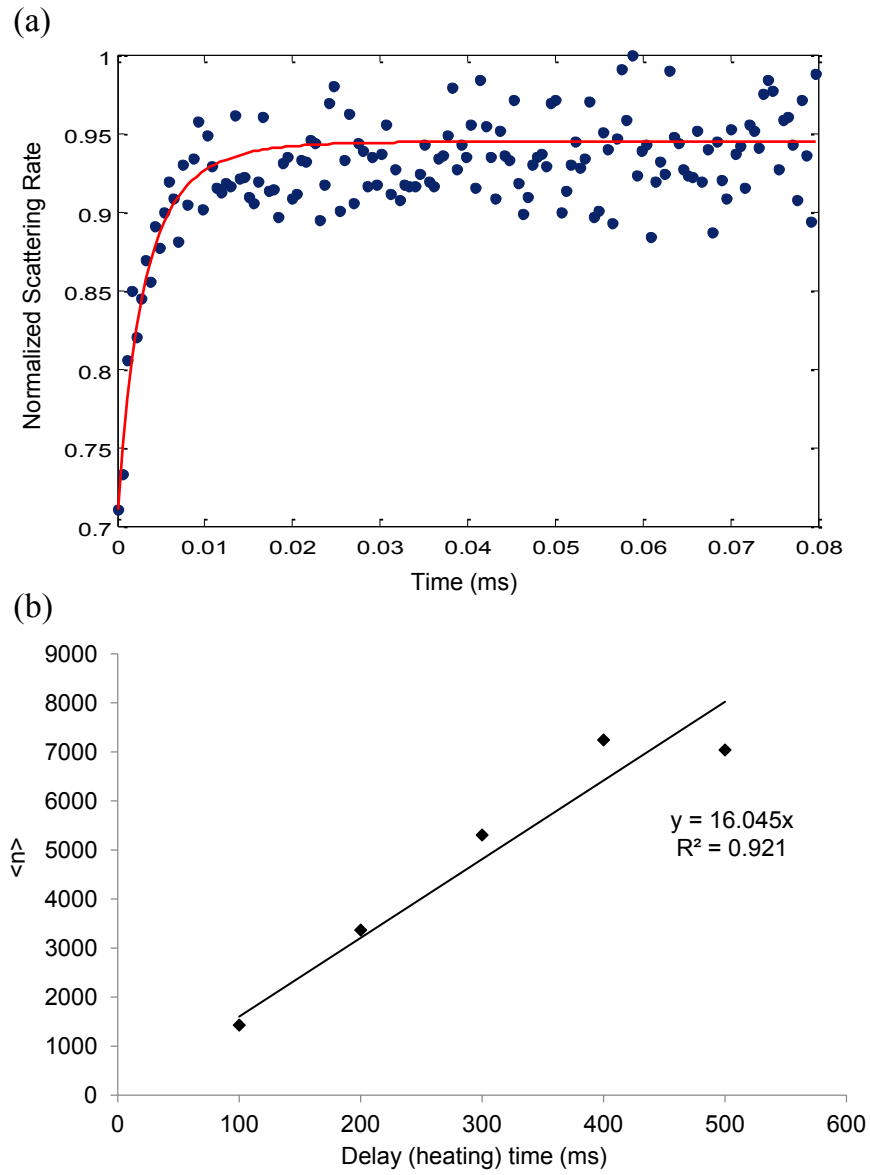

FIGURE 3.11: Scatter rate vs. time histograms for different heating periods were fit to determine the starting motional energy. (a) An example histogram showing the ion losing motional quanta of energy, indicated by the increasing scattering rate over time. The solid line is a least squares fit to the starting energy. (b) The slope of the fit describes the change in average motional quanta per unit time. The measured heating rate was 16 motional quanta/ms.

mask holder, and attaching xyz positioners below the sample stage to fine tune the position of the fiber tip with respect to the mask. The modified microscope is shown in Fig. 3.12. There are several ways to create a uniform coating of the thick liquid

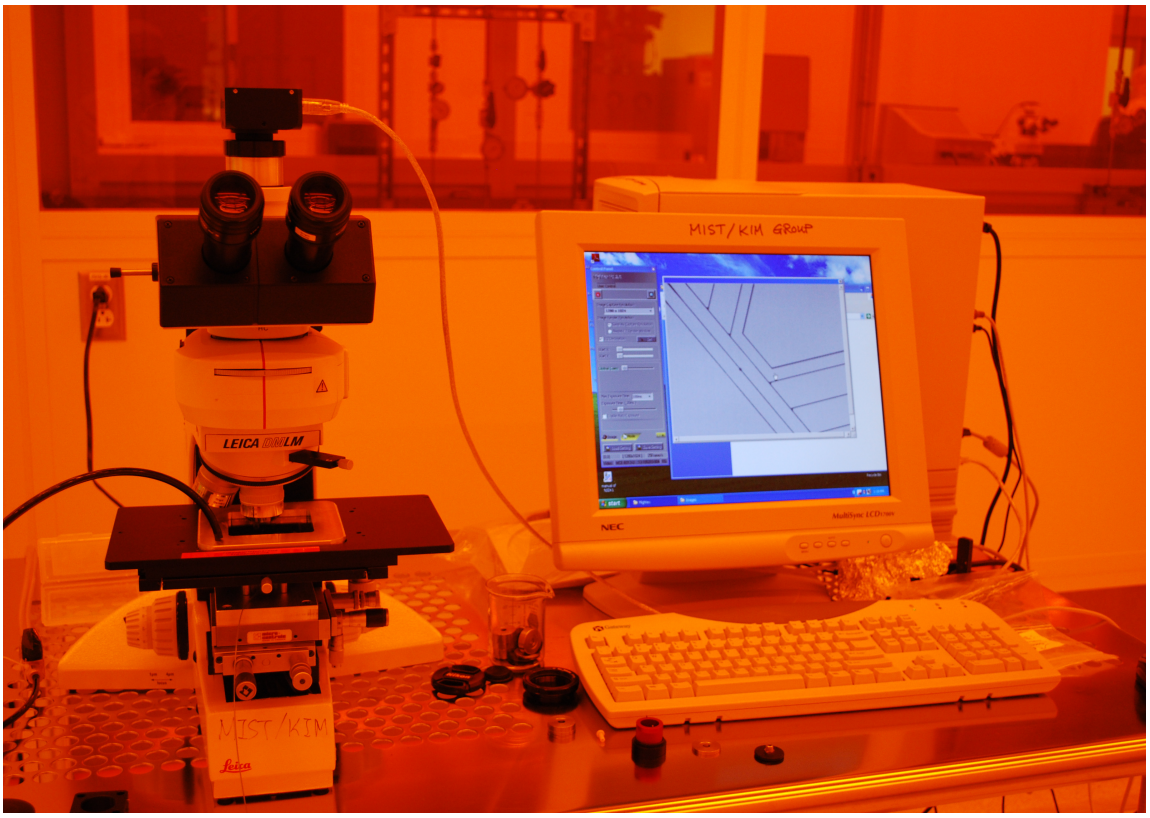

FIGURE 3.12: The fiber tip is exposed using a modified microscope. A 395 nm collimated LED source was fed backwards through an eyepiece hole after the eyepiece was removed. The distribution at the fiber tip was approximately uniform over 2 mm. A custom machined piece holds the photoresist mask with vacuum, and after-market xyz stages underneath the sample platform control the position of the fiber tip.

negative photoresist on a flat surface including stamping, reflowing, and spinning. Creating a thin (3 µm), uniform layer of resist on the fiber tip using these methods is difficult for one of two reasons: the super-polished fiber tip is not flat, and the small 2 mm outer diameter causes problems due to surface tension. When reflowed,

the resist forms a large bead that is significantly thicker in the middle than at that edge. Controlled stamping of the fiber tip on a flat surface results in variation in resist thickness according to the curvature of the fiber tip that can be on the order of 2 µm; the inconsistent results from center to edge after a complete photoresist patterning process including stamping through development are shown in Fig. 3.13. The results from spinning vary, but typically the resist beads at the edge. The entire surface of the small fiber tip is severely effected by edge effects, hence our attempts to form thin resist layers were inconsistent.

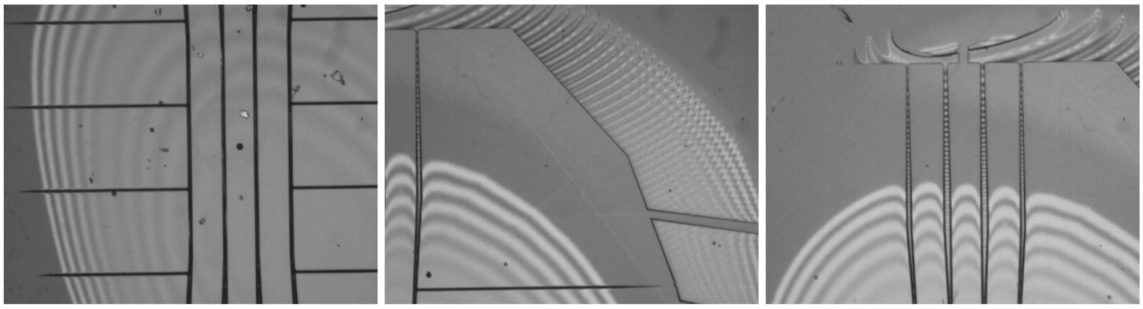

FIGURE 3.13: Example 10x microscope images from fiber tip photoresist patterning after the fiber tip has been superpolished. The superpolishing adds significant curvature down to a radius of ∼10 mm, which causes uneven coating of photoresist on the tip during photoresist stamping. The dark areas are thick (∼5 µm) photoresist, and the light rippled areas are thin layers of photoresist that should have washed away. The image on the far right shows that adjusting the process to remove the remaining photoresist in the center would leave no pattern at the edge.

At the short wavelength used in our experiment, the scattering losses from surface roughness can dominate and must be tightly controlled to create a highly reflective surface. The scattering loss l due to surface roughness is (Elson and Bennett, 1995):

$$l = \exp\left[-\left(\frac{4\pi\sigma_{\mathrm{rms}}}{\lambda}\right)^2\right], \tag{3.9}$$

where σ_{rms} is the root-mean-square (rms) surface roughness of the material, and λ is the wavelength of interest. We require ∼0.5 Å rms roughness to obtain the cavity

finesse required for our experiment. In our experience, the process of super-polishing the fiber tip unavoidably adds significant curvature to the fabrication surface. Existing fabrication techniques rely on having a flat surface, thus applying them to our polished fiber would require significant adaptation.

3.4 Summary for an Integrated Fiber, Trap, and Cavity

A deep trapping potential (270 meV) and high trap frequencies ($\sim 2\pi\times 5$ MHz) at 200 V RF combined with minimized micromotion when the ion is trapped above the central 10 μm hole of the trap indicate that our trap design is suitable for optical cavity experiments. A moderate heating rate of 16 quanta/ms is high for multiple ion experiments that require operation in the Lamb-Dicke regime, but are still suitable for single ion experiments and other tasks not requiring the ion to maintain only a few motional quanta (Wineland et al., 1998). In the future, the cavity design could be integrated with an optical fiber if the fiber were mounted in larger flat surface that could be polished simultaneously with the fiber tip, to avoid curvature due to polishing and surface tension problems during photoresist application. This work was discontinued for this thesis due to funding pressures, as well as practical limitations in realizing this design. However, work related to this cavity concept is being continued in a revised form by another graduate student.

4

Multiscale Optics for Large Solid Angle Collection

Typical construction of ion trap systems in large vacuum chambers makes it difficult to design a high NA imaging system with a wide field-of-view (FoV) due to the large distance between the ion and the first refractive optical element. The lithography industry was able to realize lens systems with a high numerical aperture (NA=0.85) and a FoV of over 25 mm (Matsuyama et al., 2006), but these optical systems suffer from complexity, size, weight, cost, and optical loss due to tens of lens elements. In conventional applications, the NA of the collection optics is limited to about 0.6, corresponding to collection efficiencies of 10% of photons emitted from a point source.

Use of reflective optics like curved mirrors opens up the possibility of dramatically enhancing the photon collection efficiency. Recent experiments and proposals using trapped ions demonstrate the benefit of adequate reflective optical elements for imaging (Shu et al., 2009), state detection (Maiwald et al., 2009), and ion-photon coupling (Luo et al., 2009) applications. While these approaches can dramatically increase the photon collection efficiency, macroscopic optical components suffer from large geometric aberrations that need to be corrected for imaging applications and can only measure point sources located in a limited FoV. Here, we apply a multiscale

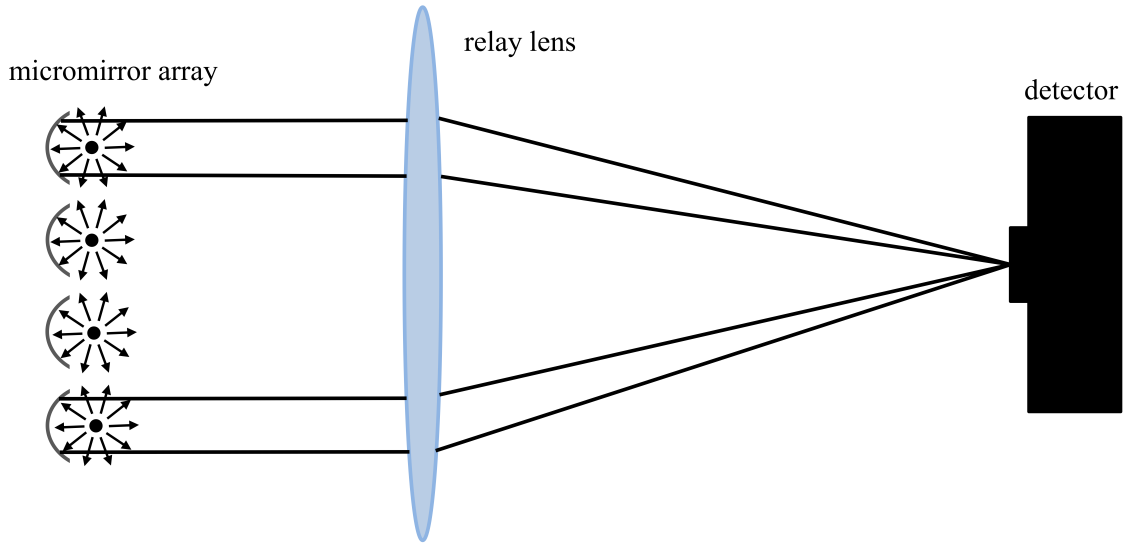

FIGURE 4.1: Micromirrors are located close to each point source to enhance collection efficiency from many sources using a single objective lens, while providing a large field of view.

optical design (Brady and Hagen, 2009) to increase the photon collection efficiency of each point source, while maintaining a large FoV to measure multiple point sources in parallel in a single optical system.

This chapter covers the design and fabrication of the micromirror and testing of the micromirror using a microsphere, as well as conclusions from testing an ion trap with an integrated micromirror.

4.1 Multiscale Optical Design

In our system design, a micromirror is located close to each point source to reflect a large fraction of the emitted photons toward the macroscopic imaging system (see Fig. 4.1). The point source is placed at the focal point of the spherical micromirror, which collimates the portion of the emitted light within its NA. The photons reflected at each micromirror form a nearly uniform, nearly collimated beam covering the aperture of the micromirror. These collimated beams can be easily imaged

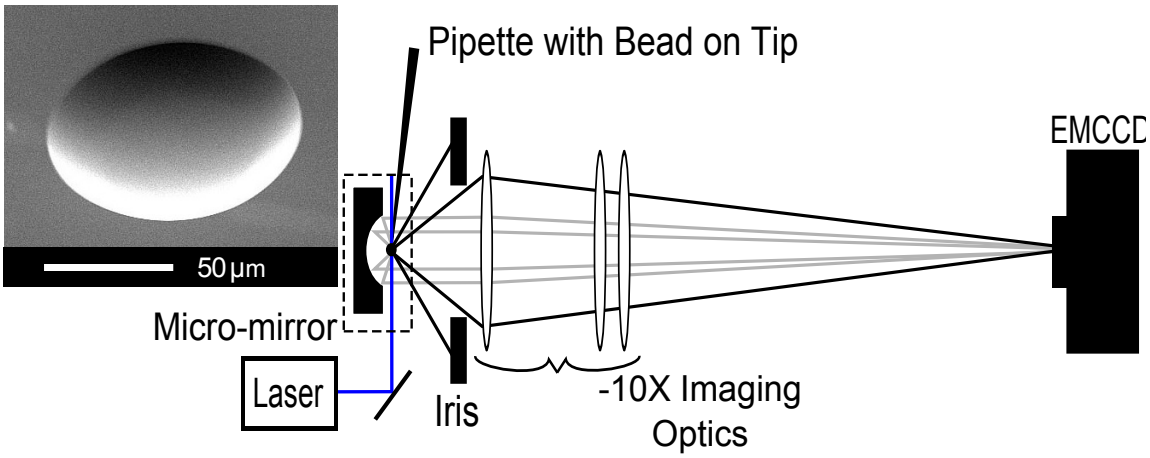

FIGURE 4.2: Experimental setup with a macroscopic $f/1.9$ imaging system and a large NA micromirror. A fluorescent microbead is used as a point source, pumped by a short wavelength laser at 407 nm. Inset shows a scanning electron micrograph of a similar mirror.

using a simple imaging system constructed from conventional, off-the-shelf optical components. In our experiment (Fig. 4.2), an $f/1.9$, 5-lens imaging system with a 2 inch aperture, a magnification of -10, and an effective focal length of 90 mm is designed and simulated with optical design software (Zemax). The optical elements were purchased from Thorlabs and assembled in our lab. The imaging system relays the reflected light from the micromirror onto its image plane, where it is detected with an electron-multiplying charge-coupled device (EMCCD, Andor iXon) with a 512×512 array of 16 µm square pixels. The collection efficiency of each point source is determined by the high NA of the micromirror, while the FoV is determined by the imaging system. One cannot achieve a diffraction-limited image of the point source using this approach. However, a dramatic increase in performance can be provided for the quantum state detection of trapped ions, and in scanning confocal imaging systems where the image resolution is determined by the light excitation source and not by the photon collection optics.

4.2 Micromirror Collection Efficiency Test Using a Microbead

4.2.1 Micromirror Fabrication

The micromirror is fabricated on a $\langle 110 \rangle$ silicon wafer, with a silicon nitride mask layer deposited using a low pressure chemical vapor deposition process. An array of mask openings ranging in diameter from 5 to 80 μm is etched in the nitride mask using reactive ion etching. The mirror used in this experiment was fabricated with a 60 μm diameter mask opening. A 1:8:1 hydrofluoric, nitric and acetic acid (HNA) bath is used to isotropically etch the exposed silicon for 10 minutes. Our process is similar to those demonstrated previously (Trupke et al., 2005), although no agitation is used during the etch. The acid ratios determine the etch rate and final surface roughness of the silicon (Robbins and Schwartz, 1960), and we chose the combination that optimizes surface smoothness (<0.5 nm RMS) and etch rate (4.5 μm/min). Using an unagitated etch, we can control the center location, depth, and radius of curvature of the micromirrrors to within ±2 μm of target values over a large wafer area (∼4 in.). We found the edge of the mirror to be very curved after the etch, which results in a wide angle of scatter both from a parallel laser beam and the object located near the focal point. To remedy this problem, the sample is coated with thick (∼15 μm) SiO_2 to protect the mirrors and then subjected to surface grinding to reduce the sag. A final chemical mechanical polish reduces the grinding scratches and smooths the substrate surface. An SEM image of a similar mirror is shown in the inset of Fig. 4.2. The micromirror used in the measurement, characterized with a Zygo optical interferometer profilometer (see Zygo measurements in Fig. 4.3), has a 100 μm radius of curvature, 90 μm opening diameter and a 15.6 μm sag. The sample is coated with aluminum, and at 407 nm the coated surface has a reflectance of 89%.

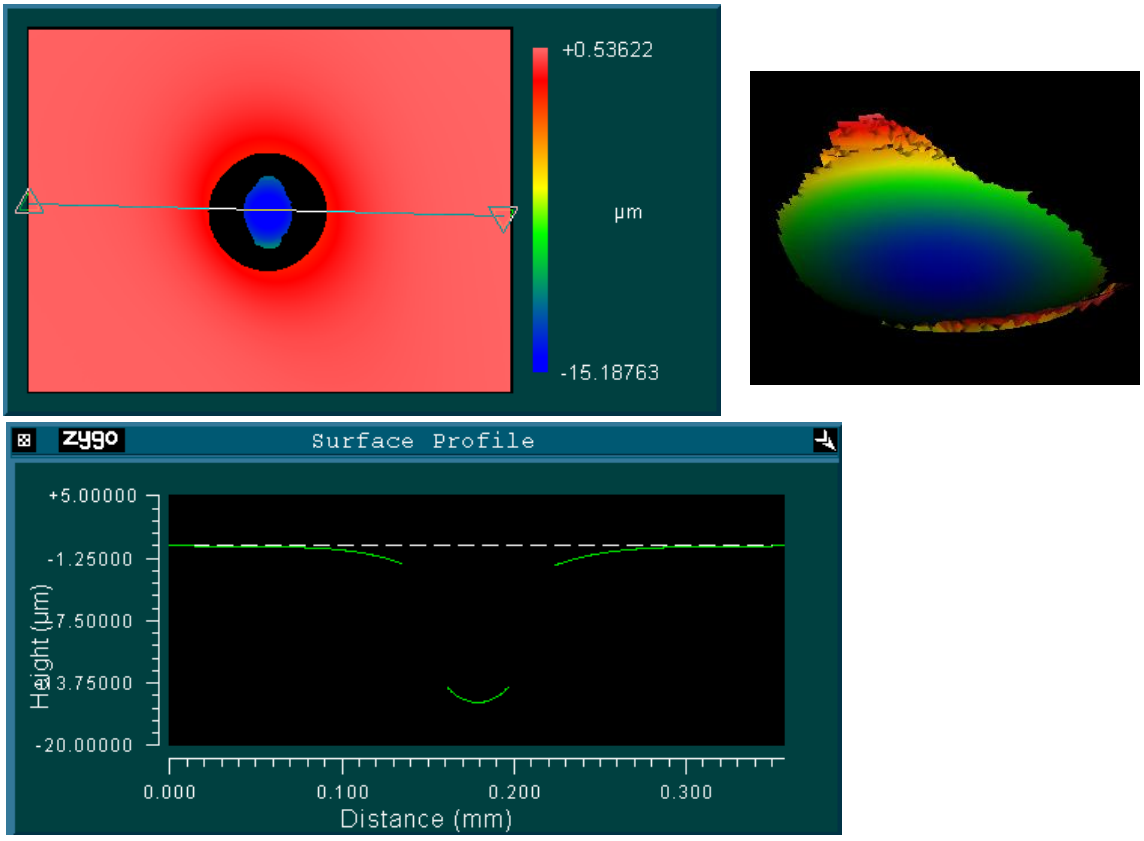

FIGURE 4.3: Zygo optical interferometer profilometer measurements of the etched micromirror after substrate surface grinding and chemical mechanical polish. (top left) A 3D view of the mirror bottom and substrate surface; data is missing due to the steepness of the sidewalls. (bottom left) A profile measurement corresponding to the line drawn across the image in the upper left. (top right) A 3D scan of the mirror bottom.

4.2.2 System Calibration

In order to demonstrate the enhancement in collection, a 15 µm polystyrene fluorescent microbead (FluoSpheres 465 nm, Invitrogen) is used for simplicity in place of a trapped ion. The bead is removed from solution and dried in air on a glass slide. A sharp glass pipette is dipped in UV curing epoxy, most of which is then rubbed off to create a thin coating on the pipette tip. The sticky pipette tip is swiped across the slide to attach a single bead near the end of the pipette, and the epoxy is cured for an hour under a UV lamp. The pipette is mounted on an xyz micromanipu-

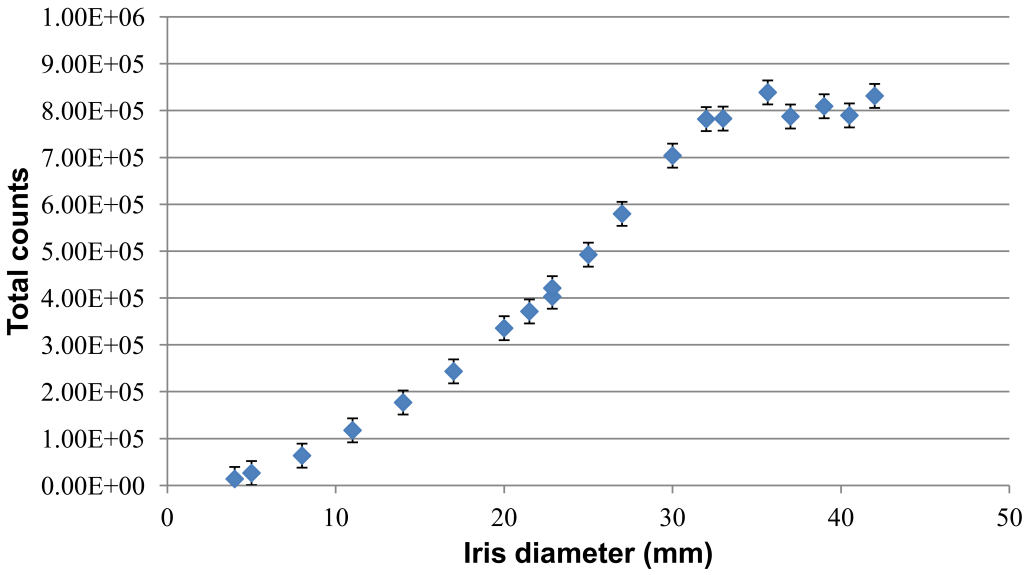

FIGURE 4.4: A bead is imaged on the camera without a micromirror. An iris is placed in front of the imaging lens and the total background corrected counts detected by the camera at different iris openings are used to provide a calibration between counts and system $f/\#$. This calibration allows us to estimate the system $f/\#$ with the micromirror.

lator with 0.2 µm resolution and the pipette is rotated so that it is not positioned between the bead and the micromirror or the bead and the objective lens. The bead is optically pumped with a 407 nm diode laser and has a broad emission spectrum centered at 465 nm. A 10 nm bandpass filter (FB-500-10-1, Thorlabs) blocks the pump wavelength prior to the detector.

The collection efficiency of the imaging system assembled in a lens tube is calibrated to the total counts measured (less background) by placing an iris in front of the first lens to control the collection solid angle of the system (see Fig. 4.4). The collection efficiency of the photons emitted by a point source using an imaging

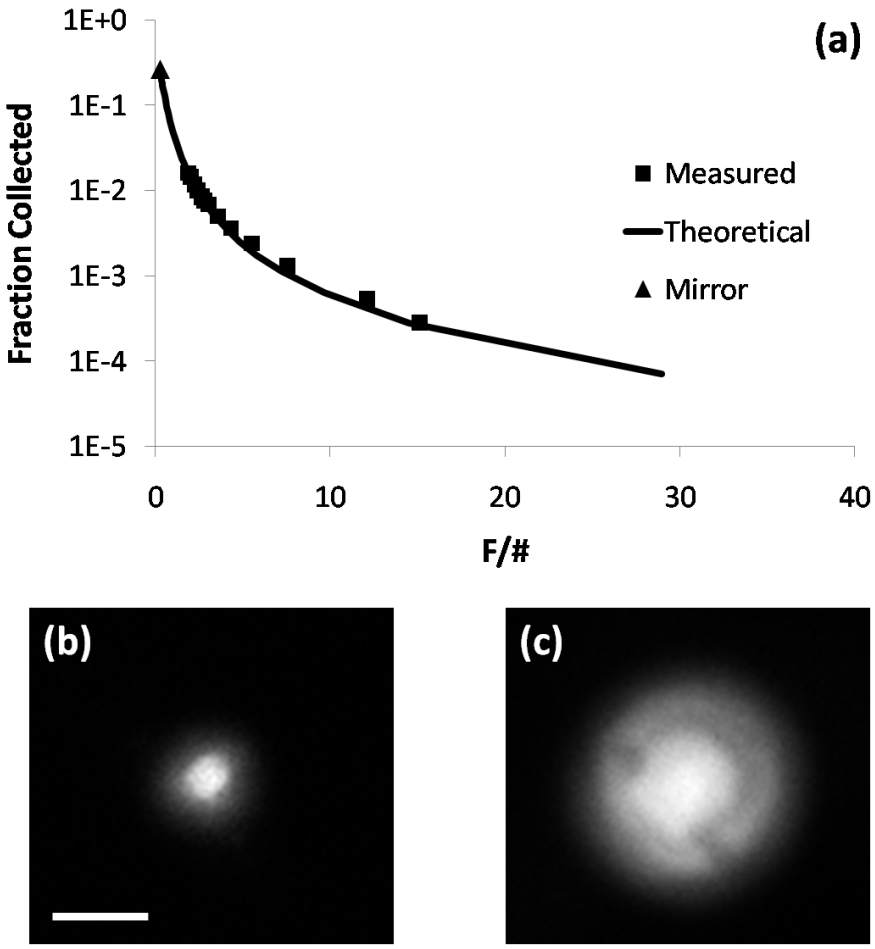

FIGURE 4.5: Measured and theoretical system $f/\#$ compared with equivalent $f/\#$ of system with micromirror determined by collection efficiency (a), and image of the bead without the micromirror in the system (b) in contrast with collection improvement with the mirror (c). Scale bar is 0.5 mm at the image plane. The shadow in image (c) is from the pipette tip, which we correct for in our final calculations.

system is related to its $f/\#$ by (solid line in Fig. 4.5(a))

$$\eta = \frac{1}{2}\left\{1 - \cos\left[\tan^{-1}\left(\frac{1}{2f/\#}\right)\right]\right\}. \tag{4.1}$$

We compared the number of background-corrected photon counts detected from the microbead fluorescence at different iris openings with Eq. 4.1 to determine the collection efficiency of the imaging system (Fig. 4.5(a)).

With the calibrated imaging optics in place, the custom fabricated micromirror is added to the system. The mirror array is adhered with wax to a kinematic mirror mount which is attached to a separate automated xyz stage with 2 µm resolution. The micromirror is aligned so that the microbead is at the mirror focal point in order to collimate the incident light toward the detector and maximize the collection efficiency. After background correction, the counts were further corrected for the shadowing due to the pipette tip holding the microbead by averaging counts across line plots of the image to estimate the total counts lost (∼2% of total counts). The amended counts were converted to fraction collected.

4.2.3 Results from Microbead Experiment

The relationship between the fraction of light collected and the effective system $f/\#$ with and without the microbead is shown in Fig. 4.5. When the iris is fully open, 1.6% of the light emitted from the bead is collected with the imaging optics, corresponding to $f/1.9$ of the imaging system (image shown in Fig. 4.5(b)). By adding the micromirror, the collection efficiency improves to 27±3% corresponding to an effective $f/0.27$ for the system. Figure 4.5(c) shows the image of the point source-micromirror combination at the EMCCD plane, showing noticeable enhancement in detected photon counts. A perfectly reflective micromirror would further improve collection to 30%.

The FoV of the optical system was measured by horizontally translating the imaging system with respect to the point source-micromirror pair and adjusting the CCD imager accordingly. Over a 17.8 mm FoV limited by our stage travel and detector size, we measured no degradation in the collection efficiency. Figure 4.6 shows the measured and simulated collection efficiency versus the object distance from the optical axis. According to our simulations, the extent of the FoV for a point source should only be limited by the aperture of the imaging system, and a FoV

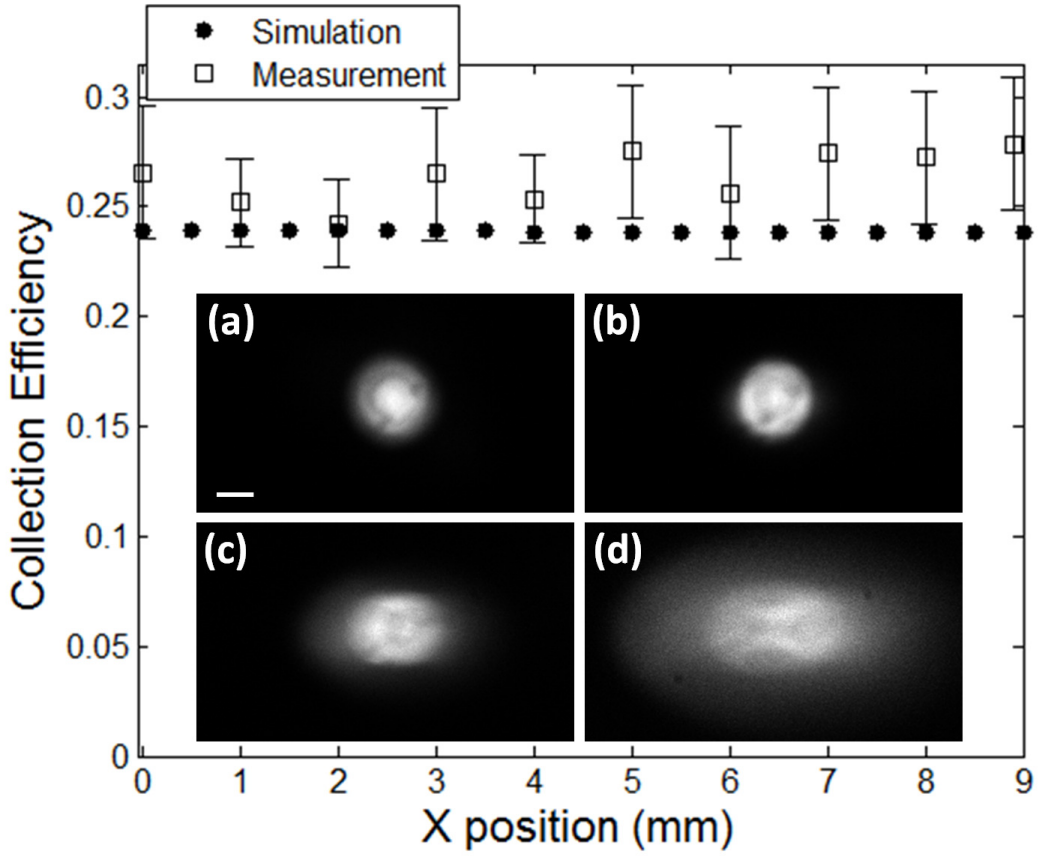

FIGURE 4.6: There is no observed reduction in collection efficiency within a 17.8 mm FoV. Distortions become apparent outside a 5 mm FoV. Scale bar is 0.5 mm at the image plane. Inset images show distortion with bead-micromirror pair distances (a) 0 mm, (b) 3 mm, (c) 5 mm, and (d) 7 mm from optical axis.

as large as 28 mm should be achievable. The image develops noticeable distortions outside a 5 mm FoV due to geometric aberrations in the imaging system, as verified in our simulations. Design of imaging systems with better aberration correction can reduce the blur if a larger FoV is desired.

The collection scheme is robust against the precise shape of the micromirror and misalignment of the point source, as verified by our simulations. Figure 4.7(a) shows the profile of the micromirror measured by a non-contact optical profiler (Zygo interferometer, as discussed above), which is fit to a fourth-order polynomial in one model (inset shows the deviation of the micromirror surface from a spherical surface).

We compared the simulated collection efficiency of several aspherical surfaces (conic constants K = -1, 0, 1) with our fourth order polynomial fit. Our fitted model yields a 4.5% lower collection efficiency compared to ideal conic surfaces. Furthermore, up to 4 μm of misalignment of the point source from the focal point of the micromirror in both x and z directions can be tolerated with less than 2.5% reduction in collection efficiency (Fig. 4.7(b)).

The bead and micromirror experiment shows that a multiscale optical system can be used to provide a significant improvement in both point source collection efficiency and FoV simultaneously over current solutions. Positioning errors and imperfections in the shape of the micromirror have minimal impact on the total collection. The micromirror array can be integrated with ion traps to provide a factor of 6 enhancement in light collection over current state-of-the-art (King, 1999), using only conventional optical components.

4.3 Testing a Multiscale Optics Integrated Trap

Micromirrors etched using the process described in the above microbead experiment were included as a design feature in a trap fabricated by Georgia Tech Research Institute. The trap design, shown in Fig. 4.8, includes 23 μm wide RF rails separated by 105 μm, which result in a 64 μm ion trapping height. A 100 μm diameter micromirror is centered between the RF rails and is located in the middle of the 1.8 mm extent of the trap. Insulating layer thickness and feature dimensions lead to a 150 V recommended RF voltage; we observed material breakdown at ∼200 V. Maximum trap depth for a given ion depends on the ion trapping height, RF voltage, RF frequency, and RF width and spacing; with 150 V of 22 MHz RF the maximum trap depth for Yb is 60 meV. Due to the increasing density of instability regions at higher Mathieu stability q parameter values (see chapter 2), the RF frequency is chosen so that $q \leqslant 0.2$ and the transverse trap frequencies are at least 1 MHz.

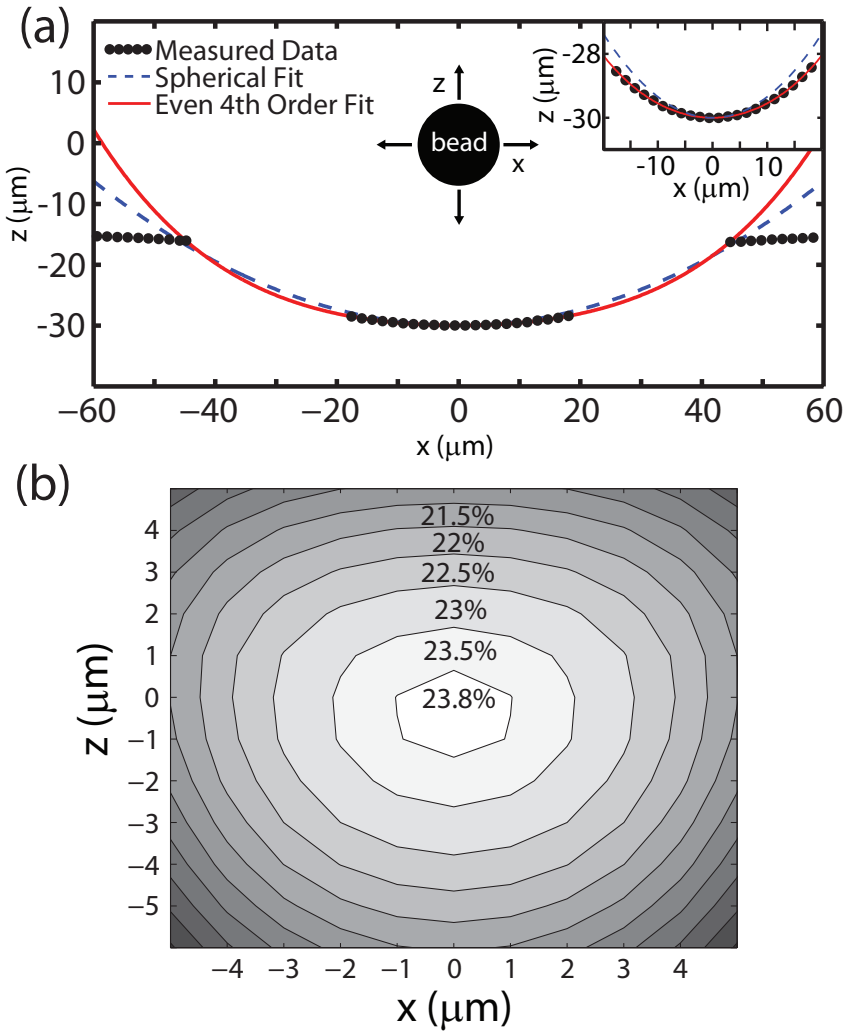

FIGURE 4.7: (a) Cross section of the measured micromirror profile (dotted line), even 4th order polynomial fit (solid line), and K=0 spherical fit (dashed line). The inset is a zoomed plot of the bowl of the mirror showing the deviation of the spherical fit from the data. (b) The simulated collection efficiency as the bead is moved away from the focal point of the mirror along the x and z directions.

The ion trap was installed in the vacuum chamber with a slotted ground plane located 2 mm above the trap to shield the ion from stray fields originating from charge buildup on the front window. An estimated 150 V RF were applied using our estimated geometric factor in calculating the power to apply to the helical resonator. After an extended period of not observing any ions when first testing a new trap, it is standard procedure to assume that the RF power is too low, thus the trap

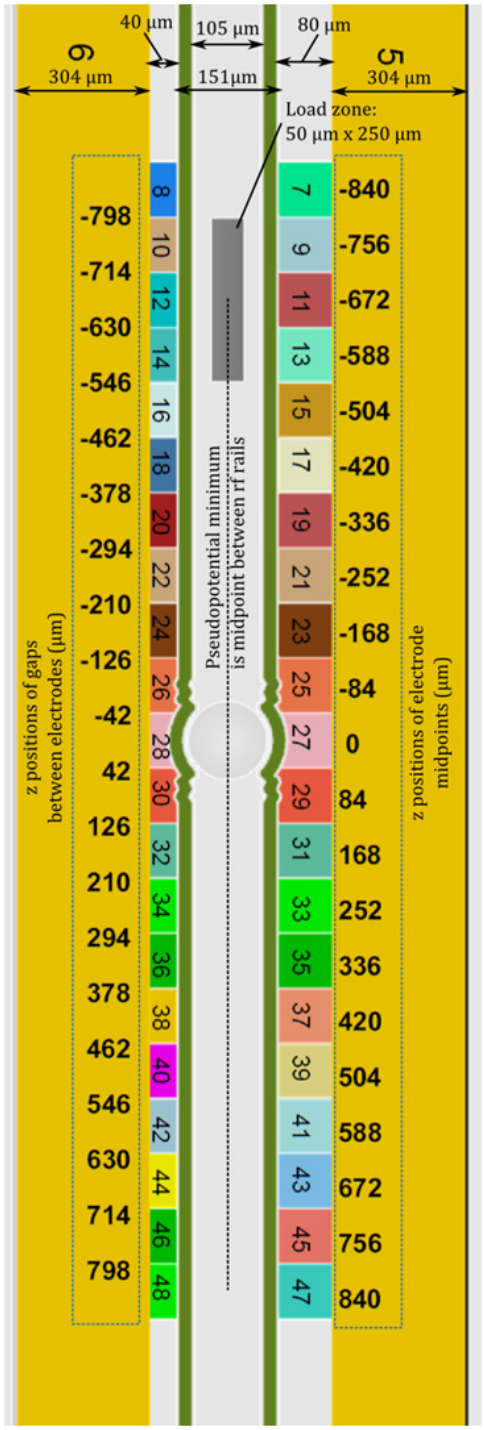

FIGURE 4.8: Design for a 100 µm diameter micromirror etched in silicon with an ion trap structure microfabricated around it. Trap from Georgia Tech Research Institute, schematic by Dr. Curtis Volin, used with permission.

too shallow, and gradually increase the RF power while scanning DC compensation voltages. After several weeks of applying a higher RF voltage to the trap, glowing was observed on the trap electrodes, which is an indication of severe leakage current and material breakdown. After replacing the chip with a duplicate trap, a capacitive voltage divider (1 pF/100 pF) was mounted at the output of the helical resonator and calibrated for measuring the applied RF voltage. A measured 150 V RF were applied to the trap. The input power to the resonator was not comparable before and after addition of the capacitive voltage divider, due to the capacitive loading which considerably altered the resonator Q-factor. DC compensation voltages were applied with varied magnitude and direction, however, no Yb ions were trapped with this design at Duke. To date, no ions have been trapped in our lab in traps less than $\sim$150 meV deep. For comparison, assuming a massless particle, a room temperature thermal trap is $\sim$39 meV. However, the melting point of ytterbium is 1091.8 K, which gives the ion an initial thermal energy of $\sim$141 meV before Doppler cooling. Others have also reported that heroic efforts are required to trap ions in shallow traps only a few times deeper than room temperature (Stick, 2007). To our knowledge, there were no physical problems in the experimental setup or with the trap itself, based on thorough capacitance and resistance measurements made outside the chamber. Some rough features were observed from the image of the laser light skimming across the surface of the trap (see Fig. 4.9); any of these could be caused by fabrication defects or dust particles on the surface of the trap. The first trap was tested with trapping calcium ions before coming to Duke, so there is reasonable certainty that any fabrication features were not harmful to the trapping potential.

Although no Yb ions were trapped in this trap at Duke, there were several helpful experimental observations: (1) the micromirror edge scatters a substantial number of photons from the laser beam, which could significantly reduce the signal to noise ratio, even with improved collection from the ion. (2) Although the ion should be

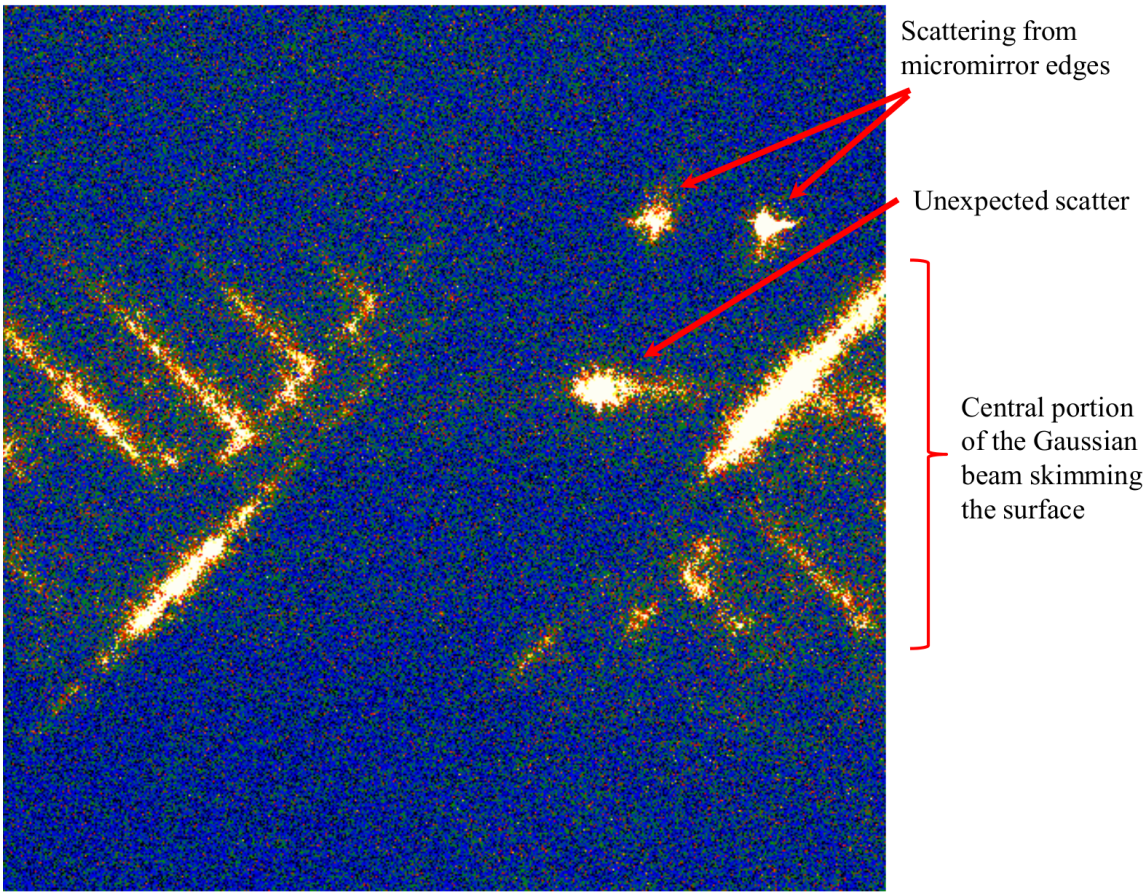

FIGURE 4.9: A false-color image showing the laser light scattering from the trap surface as it propagates parallel in close proximity to the surface (right to left). The wide band of scattering off the rectangular trap features is typical of the Gaussian beam scattering from most surface traps. We also see scattering from the edge of the micromirror, and a bright rough shape in the middle of the trap, which could come from dust on the surface or a defect from fabrication.

Doppler cooled and a trap depth of 60 meV should be sufficient for containing the Yb ion, we have more confidence in initial trapping of a hot ion using imperfect compensation voltages when using a deeper trap. (3) Final reflectivity of the mirror is limited by the surface roughness originating from the fabrication steps following the mirror etching (Merrill et al., 2011).

4.4 Summary of Multiscale Optics Experiments

Multiscale optics are a promising solution for higher efficiency light collection from a point source (∼30%). Reflective microscopic elements may result in smaller aberrations that could improve downstream mode shape, if the reflector can be fabricated with an ideal shape (e.g., parabolic or spherical). Trapped ion imaging requires a laser beam pointed at the ion in close proximity to the ion trap, which can result in large photon flux at the detector due to scattered laser light from proximate microoptic(s), although there is little data available to demonstrate this point to date. Fabrication of ideally shaped reflectors proves difficult, as is maintaining high reflectivity at short wavelengths due to roughening of the surface during the following fabrication steps.

5

Large Numerical Aperture Optics

Current ion trapping systems suffer from bulky UHV equipment and tedious vacuum chamber mechanics that make it difficult to immediately include integrated light collection optics. In order to fill this immediate need, we have purchased a custom large NA lens that requires little to no modification of current vacuum chambers, and can thus be rapidly incorporated into trapped ion experiments. The work in this chapter seeks to characterize the capability and usability of this lens in a typical ion trapping setup.

5.1 High Speed, High Fidelity State Detection with Large NA Optics

Fast qubit state detection is crucial for implementing quantum error correction (DiVincenzo and Aliferis, 2007) and fundamental tests of quantum mechanics, such as a loophole-free Bell test (Simon and Irvine, 2003). Effective qubit state detection can be achieved by driving a cycling transition between one of the qubit states and an auxiliary state with resonant light, causing state-dependent scattering (Wineland et al., 1980; Nagourney et al., 1986; Sauter et al., 1986; Bergquist et al., 1986). The state that scatters (does not scatter) light is commonly referred to as the *bright*

(*dark*) state. The detection fidelity and speed are limited by undesired effects such as off-resonant optical pumping, background photon counts, and imperfect detection of the scattered photons. The primary source of error in direct hyperfine qubit measurements is off-resonant scattering which can cause the qubit state to flip from the bright state into the dark state, or vice versa. Other significant sources of error may include polarization impurity in the excitation beam (Langer, 2006), and overlap between the photon number distributions corresponding to dark and bright states. Other methods to improve qubit detection fidelity include (1) shelving one of the qubit states to an auxiliary state (Langer, 2006; Myerson et al., 2008), (2) using the arrival time of the detected photons to identify qubit flip events (Myerson et al., 2008), and (3) extending the qubit measurement to multiple measurement attempts using a quantum logic gate (Schaetz et al., 2005; Hume et al., 2007). All demonstrated approaches suffer from low detection efficiency of photons scattered by the bright qubit state ($\approx 10^{-3}$), resulting in a slow measurement that limits efficient implementation of quantum error correction (DiVincenzo and Aliferis, 2007). Various strategies for implementing optical components integrated with trapped ions or neutral atoms to dramatically enhance the collection efficiency have been suggested (Noek et al., 2010; Shu et al., 2010; Streed et al., 2011; Merrill et al., 2011; Maiwald et al., 2012; Bochmann et al., 2010), and can lead to improved detection speed and fidelity. By drastically improving the detection efficiency of the scattered photons, reducing the background photon count rates, and employing a time-tagging circuit, we demonstrate a substantial improvement in the qubit measurement time far below multi-qubit gate times while maintaining a high fidelity.

5.1.1 Large NA State Detection Experiment Setup

Ytterbium is loaded into the trap from a natural Yb filled thermal oven located behind the trap. The isotope loaded into the trap is selected by the photoionization

laser frequency and the detuning of the Doppler cooling beam: undesired isotopes are inefficiently ionized, and in the rare occurrence of ionization the ion does not remain trapped due to the shallow depth of the trap and lack of efficient cooling. Spectroscopy using the 399 nm laser gives information about the most efficient photoionization frequency, flux of neutral atoms, and pointing of the Yb oven. The counts are monitored on the EMCCD camera with background subtraction and long integration time ($\sim$1 s), while the oven is ramped up from a typical trapping current of 0.87 A to 1 A.

For this experiment, a single trapped $^{171}Yb^{+}$ ion is directly imaged using a custom objective lens (Photon Gear, Inc.) with a large object side numerical aperture (NA = 0.6) capable of collecting 10% of the total light scattered by the ion. The lens tube diameter is approximately 2 in. and the objective weighs a few pounds. The working distance is approximately 12 mm plus the width of the vacuum window (4 mm). The system is shown in Fig. 5.2(a).

A microfabricated radio frequency (RF) Paul trap (Thunderbird, Sandia National Laboratories (Stick et al., 2010)) is used to trap a single ion 80 μm above the planar surface of the trap (Stick et al., 2010; Monroe and Kim, 2013). The symmetric trap features a 100 μm central backside loading slot, or gap, with two inner DC lines. The RF rails and dielectric layers are thick enough to tolerate 300 V of RF. We apply 250 V at 28 MHz, which gives a Mathieu stability parameter $q = 0.2$ and transverse trap frequencies near $2\pi \times 2$ MHz. A ground plate is located 2 mm above the trap surface, with a slot (NA $\approx$ 0.6) extending the length of the trap to allow imaging of the ion along the central linear trap axis (Fig. 5.2(b)). The 370 nm Doppler cooling and detection beams delivered to the trap setup via single mode fibers and are designed to have beam waists of $w_{\circ}$=30 μm. Paddle wheels control the polarization of the cooling, detection, and repump beams, and are set to maximize the ion's scattering rate.

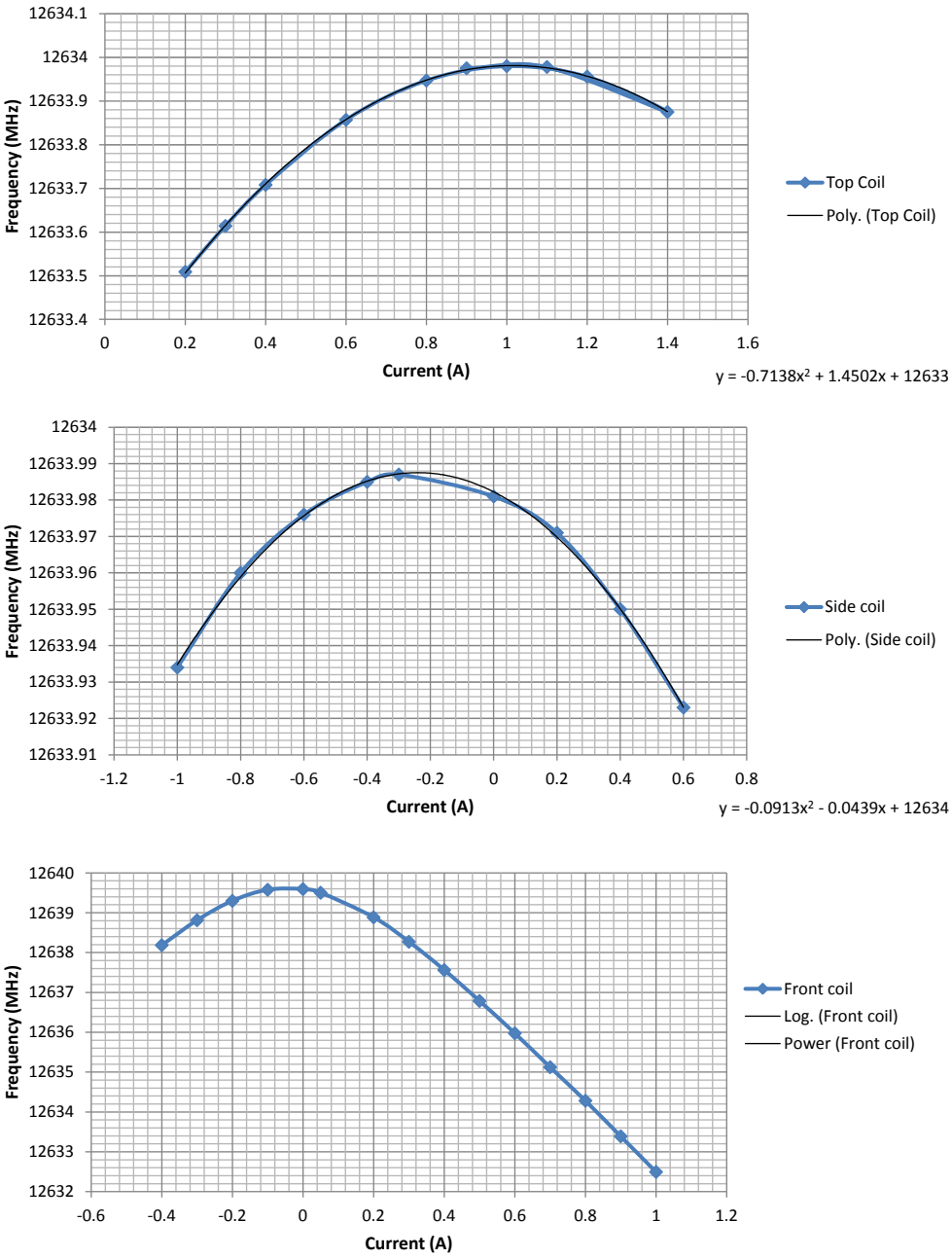

FIGURE 5.1: Magnetic field zeros for three coils. The magnetic field is adjusted, and then the microwave frequency is scanned to find the resonant frequency between the qubit $|0\rangle$ and $|1\rangle$ states. Independent control of each axis simplifies the field tuning and we can easily increase or decrease the field in a single direction at a time. The inflection point indicates the magnetic field zero for that direction.

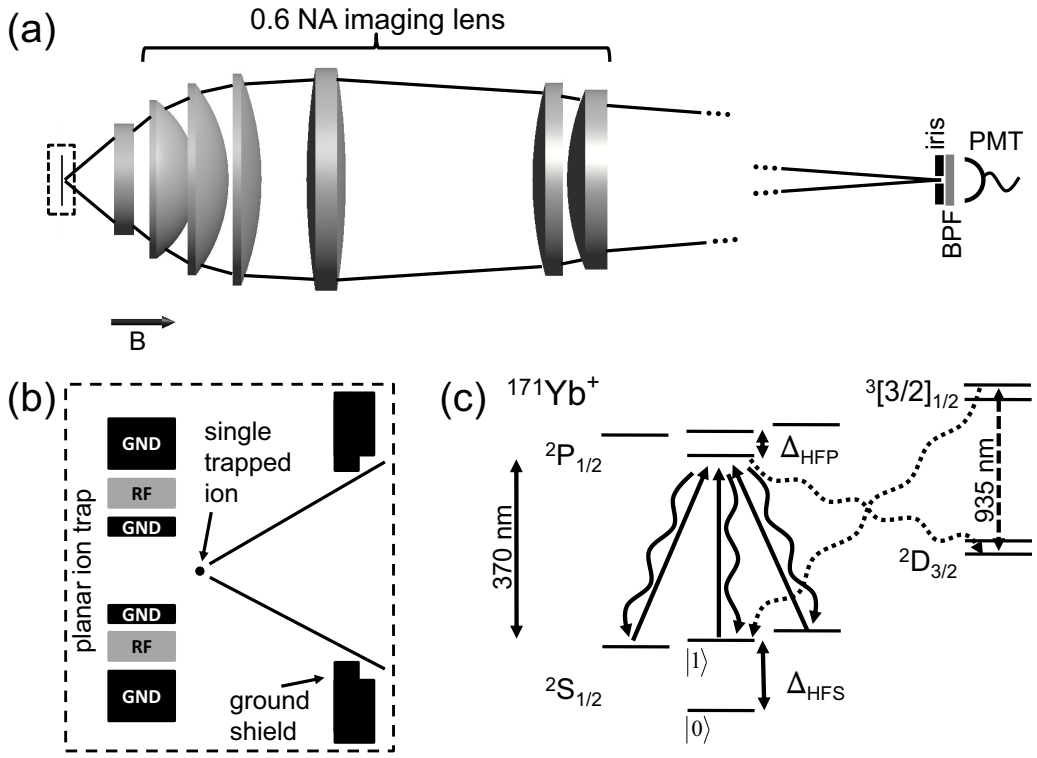

FIGURE 5.2: (a) A single ion is trapped using a microfabricated surface RF trap and imaged through the vacuum window by a large numerical aperture (NA = 0.6) lens. BPF: Band pass filter, PMT: Photomultiplier tube. The dashed-box region is magnified in (b) (not to scale). (c) Relevant energy levels of $^{171}Yb^{+}$. Δ_{HFS} and Δ_{HFP} are the hyperfine splitting of the S and P levels, respectively.

The magnetic field strength is tuned to be optimal for the ion scattering rate (discussed below), and the direction is tuned to be perpendicular to the surface of the trap. Individual magnetic field coils control each spatial direction, with the coils located on top of the chamber, on the side of the chamber, and on the front of the chamber. This allows us to easily and specifically tune the magnetic field for an ideal Zeeman splitting between levels. Plots of the current required for the coils as an example of the zero finding process are shown in Fig. 5.1.

Emitted photons are collected by the objective lens and focused on an iris used as a spatial filter. The light then passes through a 6 nm bandpass filter (Semrock) and is detected with a photon counting photomultiplier tube with 32% quantum

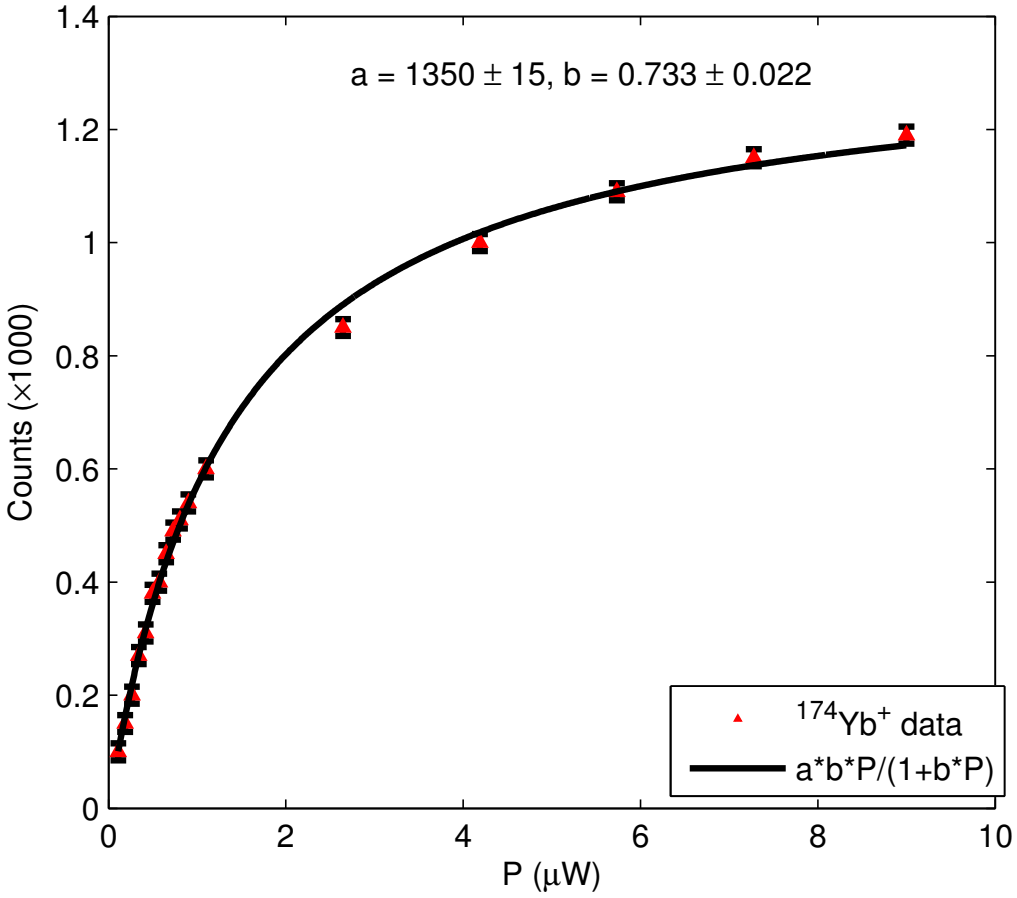

FIGURE 5.3: System calibration with resonant scattering from $^{174}Yb^{+}$, which closely follows the scattering rate of a simple two level system, allows us to determine our beam radius and collection efficiency. Here a$= \varepsilon\Gamma/2$ and b$P = I/I_{\rm sat}$.

efficiency at 370 nm (Hamamatsu). The overall photon detection efficiency, ε, was determined to be 2.2(1)% by measuring the photon counts as a function of detection beam power for $^{174}Yb^{+}$, an isotope which closely follows the simple scattering model of a two-level system such that on resonance (Fig. 5.3),

$$R_{174\rm Yb} = \frac{\Gamma}{2}\left(\frac{I/I_{\rm sat}}{1+I/I_{\rm sat}}\right), \tag{5.1}$$

with $I_{\rm sat}$=51 mW/cm^2 and $\Gamma = 2\pi \times 19.6$ MHz. For all calculations we use SI units,

and the intensity is defined as $I = cn\epsilon_0|E|^2/2$, where c is the speed of light, n is the refractive index of the medium, ϵ_0 is the vacuum permittivity, and E is the electric field.

Figure 5.2(c) shows the relevant energy levels of the hyperfine $^{171}Yb^+$ qubit. The qubit states $|0\rangle$ and $|1\rangle$ are defined as the two hyperfine states $^2S_{1/2}\left|F=0, m_f=0\right\rangle$ and $^2S_{1/2}\left|F=1, m_f=0\right\rangle$, respectively. The ion is prepared in the $|0\rangle$ state by applying light resonant with the $^2S_{1/2}\,|F=1\rangle \rightarrow\ ^2P_{1/2}\,|F=1\rangle$ transition for 150 µs with error $<1\times10^{-4}$. The optimal power for the EOM is determined mathematically to avoid pumping the ion bright due to power in the 7th sideband, which would be near resonance (2.1 GHz×7=14.7 GHz) with the transition from $|0\rangle$ to the $^2P_{1/2}|F=1\rangle$ state. Optimally, in the absence of bright pumping from the seventh sideband, the first sideband (2.1 GHz) should be maximized for efficient pumping to $|0\rangle$. Instead, enough power is applied to the EOM to minimize the carrier (as observed with an optical cavity signal). The error is on the order of $\sim10^{-6}$, which is almost two orders of magnitude lower than other sources of error. Because of this, we cannot detect error originating from imperfect modulation power. However, should other methods of light collection reduce the other errors, this could become significant. After the ion is pumped dark, an optional microwave π-pulse resonant with the $^2S_{1/2}$ state hyperfine splitting can rotate the ion to the $|1\rangle$ state in 240 µs with error $<5\times10^{-4}$. The microwave is tuned to within 1 kHz of resonance with the $|0\rangle \leftrightarrow |1\rangle$ energy spacing, then, because of the 1 kHz limited resolution of our microwave source, the magnetic field is fine tuned to bring the level spacing to resonance with the microwave signal. Microwave Rabi flopping, the population transfer from $|0\rangle$ and $|1\rangle$ and back again, is monitored long enough to observe a few rotations between $|0\rangle$ and $|1\rangle$ before the data is collected. We confirm with Rabi flopping that the microwave is resonant and the background counts are low (i.e., there is high visibility), and we obtain the π-time for moving the population from $|0\rangle$ to $|1\rangle$.

The detection fidelity for the $^{171}Yb^{+}$ hyperfine qubit is measured by preparing the ion in either the $|0\rangle$ or $|1\rangle$ state, followed by a detection time during which the ion is exposed to the detection beam resonant with the $^2S_{1/2}\,|F=1\rangle \rightarrow {}^2P_{1/2}\,|F=0\rangle$ transition, focused to a 41 μm beam waist at the ion. In the absence of off-resonant scattering, an ion in the $|0\rangle$ (dark) state will scatter no photons, whereas an ion in the $|1\rangle$ (bright) state will experience a cycling transition (the $^2S_{1/2}\,|F=0\rangle \rightarrow {}^2P_{1/2}\,|F=0\rangle$ transition is forbidden by dipole selection rules) and scatter photons at a rate of $R_\circ$. Throughout the initialization and detection process, a repump beam at 935 nm prevents the ion from remaining in the $^2D_{3/2}$ state, which has a lifetime of 52.7 ms that is significantly longer than our experimental timescales.

5.1.2 System Characterization

One can effectively distinguish the bright state from the dark state by monitoring the scattered photons. The speed and fidelity of identifying the bright state increase with higher photon collection efficiency, while R_{dc}, the sum of PMT dark counts (6.5 Hz) and background photon counts (0.94 Hz cm^2/mW), degrades the fidelity of identifying the dark state. Example histograms from this setup are shown in Fig. 5.4. At the highest measured fidelity, the signal to background ratio (SBR), which we define as the average signal counts to the average total background noise, is 5,000. Detection error can also arise from the off-resonant scattering of the $|1\rangle$ ($|0\rangle$) state to the $^2P_{1/2}\,|F=1\rangle$ state, from which it can decay to the $|0\rangle$ ($|1\rangle$) state, at a rate R_d (R_b).

We experimentally determine all relevant scattering rates that impact the qubit state detection process. The scattering rate of the bright state $R_\circ$ and the rate of dark pumping R_d take into account optical pumping to coherent dark states (Berkeland and Boshier, 2002). Coherent dark states occur when there are at least as many degenerate ground states as excited states such that no matter the polarization of the

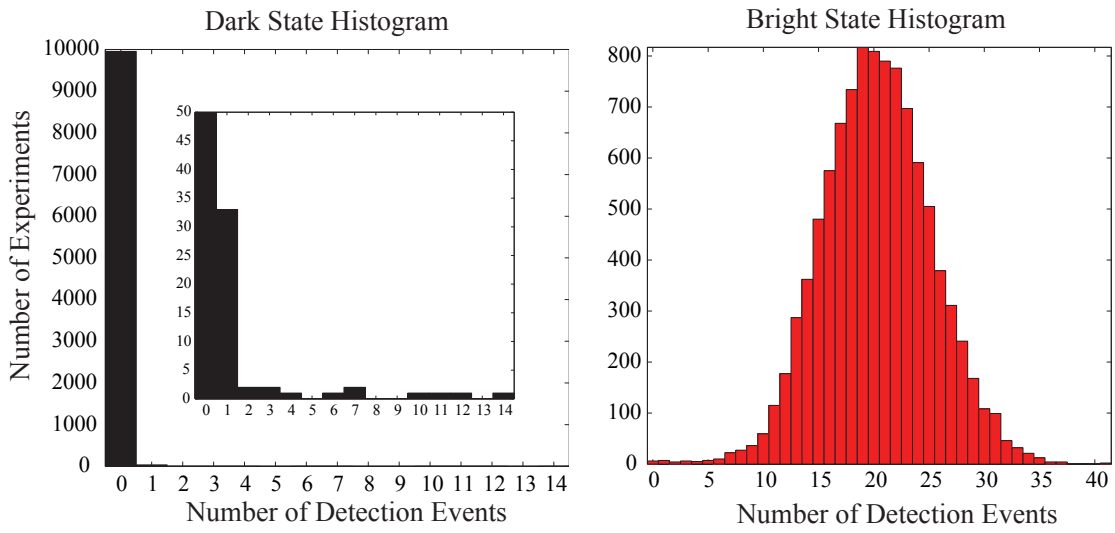

FIGURE 5.4: Typical histograms for 1 ms detection time with beam intensity $8\,\mathrm{mW/cm^2}$. The inset shows a zoomed view of the dark state histogram, where the single photon events are mostly due to background counts, whereas higher photon numbers originate from bright pumping. The bright state histogram shows the Poissonian distribution with a lower photon count tail that comes from cases where the bright ion pumped dark.

applied laser field, there is at least one state pumped dark. Even when the degeneracy of the ground states is lifted by applying a magnetic field, there is a reduction in the overall scattering rate. For our case, we can consider the situation with different polarizations of light. Assuming the beam contains only σ_+ light, we find that the $^2\mathrm{S}_{1/2}\big|F=1, m_f=0,+1\big\rangle$ states are pumped dark. If the beam contains only π-polarized light, the $^2\mathrm{S}_{1/2}\big|F=1, m_f=-1,+1\big\rangle$ states are pumped dark. Similarly, with only σ_--polarized light, the $^2\mathrm{S}_{1/2}\big|F=1, m_f=-1,0\big\rangle$ states are pumped dark, as shown in Fig. 5.5 for the $R_\circ$ case. Appropriate control of the detection beam polarization allows us to address all transitions, and the Zeeman splitting, δ, is chosen to destabilize these dark states, making them time-independent. For $\delta \ll \Omega$, the state evolution is slow enough that the atom can follow the dark state, and for $\delta \gg \Omega$ the scattering rate is reduced because of the detuning. The maximal scattering

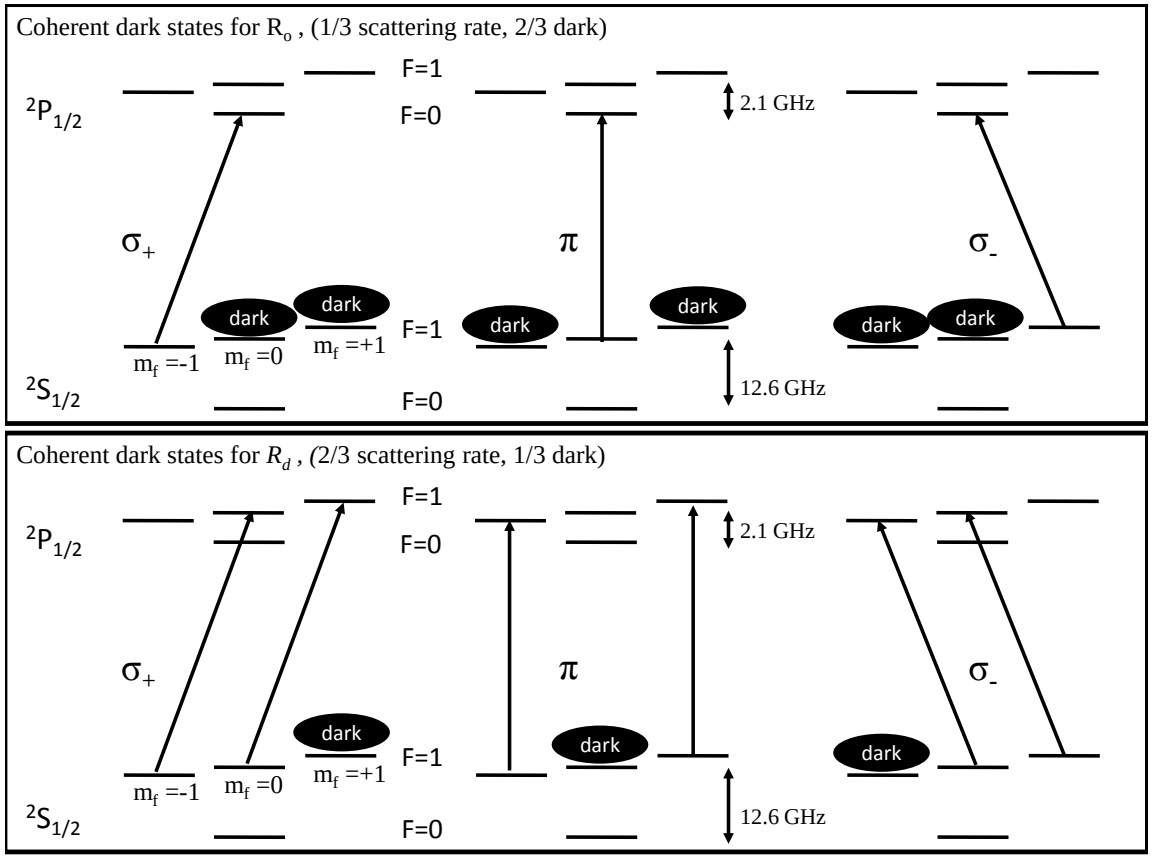

FIGURE 5.5: Coherent dark states occur when there are at least as many ground states as excited states such that a single laser field always pump the ion into a dark state. Here, coherent dark states occur for different light polarizations in $^{171}Yb^+$. For a combination of σ_+, σ_-, and π light, there still exist superpositions of states which are dark.

rate is obtained for a Zeeman splitting $\delta = \Omega/2$. In this work the Zeeman splitting is fixed (by fixing the magnetic field) at $\delta = 2\pi \times 4.8\,\text{MHz}$. The optimized scattering rate of the ion is given by:

$$R_{\circ,\text{opt}} = \left(\frac{1}{3}\right)\left(\frac{\Gamma}{2}\right)\frac{s_\circ}{1+\frac{2}{3}s_\circ+\left(\frac{2\Delta}{\Gamma}\right)^2}, \tag{5.2}$$

where $\Gamma = 2\pi \times 19.6\,\text{MHz}$ is the linewidth of the $^2P_{1/2}$ state, $s_\circ = 2\Omega^2/\Gamma^2$ (with Rabi frequency Ω) is the on-resonance saturation parameter, and Δ is the detuning of the detection beam from the cycling transition resonance. This result assumes an

optimal Zeeman splitting of half the Rabi frequency ($\delta = \Omega/2$), which is a function of the optical power. At higher powers the scattering rate decreases because the ion will pump into a coherent dark state on a timescale faster than the destabilization rate of the coherent dark states (given by δ) and remains dark for a larger fraction of the time.

The rate at which an ion initially in the $|1\rangle$ state will pump to the $|0\rangle$ state for large detuning is

$$R_d \approx \left(\frac{2}{3}\right)\left(\frac{1}{3}\right)\left(\frac{\Gamma}{2}\right)\left(\frac{2\Omega^2}{\Gamma^2}\right)\left(\frac{\Gamma}{2\Delta_{\mathrm{HFP}}}\right)^2, \tag{5.3}$$

where $\Delta_{\mathrm{HFP}} = 2\pi \times 2.1\,\mathrm{GHz}$ is the hyperfine splitting of the $^2\mathrm{P}_{1/2}$ state. The factor of 2/3 is due to the fact that one out of three states in the $^2\mathrm{S}_{1/2}\,|F=1\rangle$ manifold is a coherent dark state at any given time, and so the expected reduction in the scattering rate for this transition is smaller than that for $R_\circ$. The factor of 1/3 is the branching ratio of the $^2\mathrm{P}_{1/2}\,|F=1\rangle$ states decaying into the dark $|0\rangle$ state. Similarly, the rate for $|0\rangle$ to pump into one of the bright $^2\mathrm{S}_{1/2}\,|F=1\rangle$ states is

$$R_b \approx \left(\frac{2}{3}\right)\left(\frac{\Gamma}{2}\right)\left(\frac{2\Omega^2}{\Gamma^2}\right)\left(\frac{\Gamma}{2\left(\Delta_{\mathrm{HFP}} + \Delta_{\mathrm{HFS}}\right)}\right)^2, \tag{5.4}$$

where $\Delta_{\mathrm{HFS}} = 2\pi \times 12.6\,\mathrm{GHz}$ is the hyperfine splitting of the $^2\mathrm{S}_{1/2}$ state, and the factor of 2/3 is the branching ratio of the $^2\mathrm{P}_{1/2}\,|F=1\rangle$ states decaying into the bright $^2\mathrm{S}_{1/2}\,|F=1\rangle$ states. For $^{171}\mathrm{Yb}^+$ ions, R_d/R_b=16.3.

These scattering rates are measured by preparing the ion in the $|1\rangle$ state and detecting the scattered photons over a duration τ. We fit this data to the function

$$\bar{n}(\tau) = \int_0^\tau \varepsilon R_\circ p_1(t)\,\mathrm{d}t, \tag{5.5}$$

which is obtained by simultaneously solving the equations $\dot{p}_1 = R_b p_0 - R_d p_1$ and $p_0 + p_1 = 1$ for $p_1(t)$, where $p_1(t)$ ($p_0(t)$) is the probability of the ion to be in the

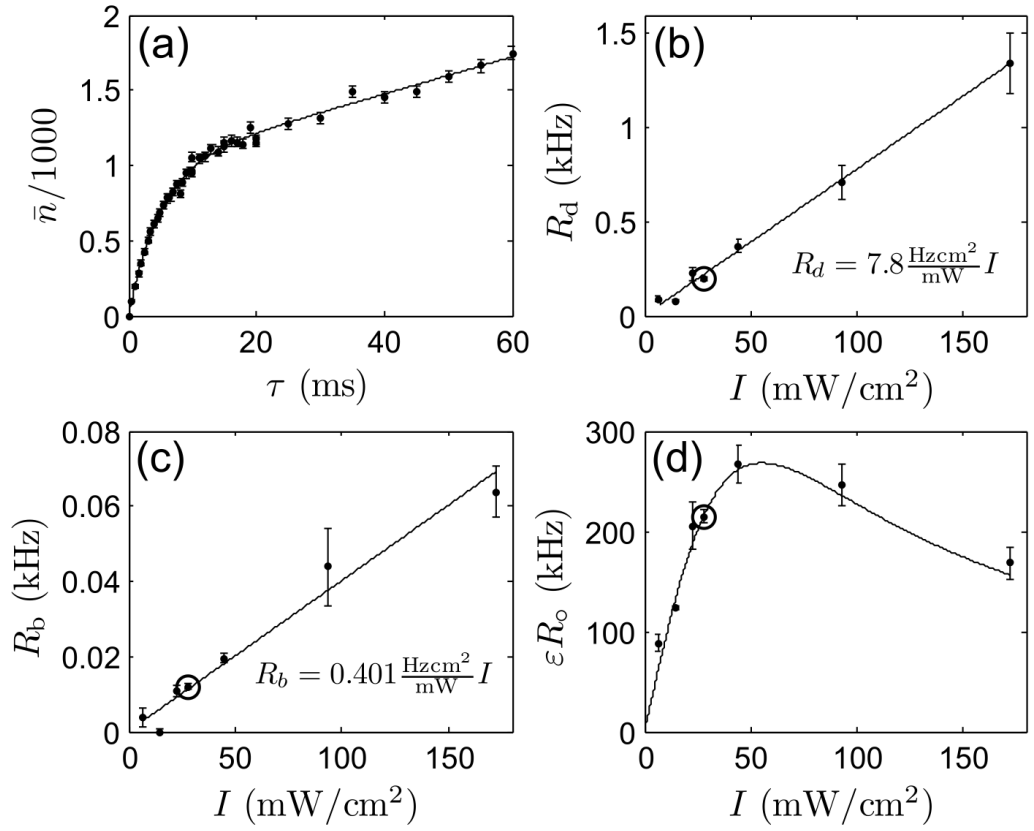

FIGURE 5.6: (a) A sample plot of the average number of detected photons ($\bar{n}$) in a duration τ with a detection beam intensity of 29 mW/cm^2. (b) The dark pumping rate (R_d), (c) the bright pumping rate (R_b), and (d) the photon detection rate in the absence of dark pumping ($\varepsilon R_\circ$). R_d and R_b are fitted to a line to obtain the proportionality constant between the detection beam power and the square of the Rabi frequency, which is used to obtain the theoretical curve for $R_\circ$. Circled points in (b)-(d) correspond to the data shown in (a).

bright states (dark state) as a function of time (see Fig. 5.6(a)), and ε is the detection efficiency. From these measurements, we can experimentally determine the dark pumping rate R_d, bright pumping rate R_b and the photon detection rate $\varepsilon R_\circ$ as a function of optical intensity (Fig. 5.6(b), (c), and (d), respectively).

5.1.3 Strategy for Fast, High Fidelity State Detection

One strategy to discriminate the bright and dark states is to count the number of detected photons over a given detection period $\tau_{\max}$ and compare it to a fixed threshold (the threshold method). Alternatively, if the photon time of arrival information is available, one can utilize a more effective decision procedure to reduce the average detection time (Myerson et al., 2008). For the conditions in our experiments with high photon detection efficiency and low background counts, we attribute any detection cases with zero counts as dark states and those with two or more counts as bright states. The ambiguity arises for those cases where the PMT registers one event during the detection period: these counts can arise from either a background count for a dark qubit state, or from a bright qubit state that pumps dark after one photon is detected. We employ a fast detection scheme where we monitor the arrival time of at most the first two detection events. If the first event occurs before a cut-off time τ_c, it is likely a photon from a bright state scattering event, and the state is determined to be bright. However, if the first event occurs after τ_c, we wait for a second event up to a maximum wait time $\tau_{\max}$. The state is declared bright as soon as a second event is registered, whereas if no more events occur, the first event is more likely from a background count and the state is determined to be dark. This two-event discrimination (TED) method leads to a measured 8-21% reduction in state detection error over the threshold method.

It is unlikely for an ion starting in the $|0\rangle$ state to pump bright and scatter only a single photon. Therefore, the probability of registering the first event before a time t grows linearly and depends only on $R_{\rm dc}$ ($P_0(t) \approx R_{\rm dc}t$). The probability of detecting the first photon before t for an ion in the $|1\rangle$ state is approximately given by:

$$P_1(t) \approx R_d/(\varepsilon R_\circ)\left[1-\exp(-\varepsilon R_\circ t)\right], \tag{5.6}$$

where the first factor is the probability of off-resonant scattering to $|0\rangle$ after obtaining

the first photon (in the limit where the Poissonian probability of obtaining only a single photon is negligible), and the second factor is the probability of at least one event occurring before t (or conversely, one minus the probability that zero photons are detected before time t). Recall that the Poisson distribution has the probability for a discrete random variable X to take on a positive integer value k given by

$$\mathrm{P}(X = k) = \frac{\lambda^k e^{-\lambda}}{k!},$$

where λ is the positive, real expected value, which is also the variance.) We find the time where $P_1(t) - P_0(t)$ is maximized by setting the time derivative equal to zero:

$$\begin{aligned}
\frac{d}{dt}[P_1(t) - P_0(t)] &= 0 \\
\frac{d}{dt}\left\{\frac{R_d}{\varepsilon R_\circ}\left[1 - \exp\left(-\varepsilon R_\circ t\right)\right] - R_{\mathrm{dc}} t\right\} &= 0 \\
\frac{R_d}{\varepsilon R_\circ}\left(-\varepsilon R_\circ\right)\left[-\exp\left(-\varepsilon R_\circ t\right)\right] - R_{\mathrm{dc}} &= 0 \\
\exp\left(-\varepsilon R_\circ t\right) &= \frac{R_{\mathrm{dc}}}{R_d} \\
-\varepsilon R_\circ t &= \ln\left(\frac{R_{\mathrm{dc}}}{R_d}\right)
\end{aligned}$$

then by rearranging and letting $\tau_c = t$ we obtain the cutoff time,

$$\tau_c = \ln\left(R_d/R_{\mathrm{dc}}\right)/\varepsilon R_\circ, \tag{5.7}$$

the time before which the first photon detection event is more likely to have originated from a bright state. The maximum wait time $\tau_{\max}$ is determined experimentally and depends on R_b. This is because the overall error probability starts to increase after $\tau_{\max}$ due to the small chance of off-resonant pumping of the dark states to $|1\rangle$, and because the bright state error reaches a lower limit given by the fraction of bright ions which pump dark before a sufficient number of photons are collected (Fig. 5.7

inset). The overall error probability reaches a minimum (and therefore the detection window for the TED method is ended) at $t = \tau_{\max}$. It will always take the maximum time $\tau_{\max}$ to determine the state as dark. However, the bright state is typically determined on a timescale $\sim 1/(\varepsilon R_\circ) \ll \tau_{\max}$, reducing the average state detection time by almost a factor of two.

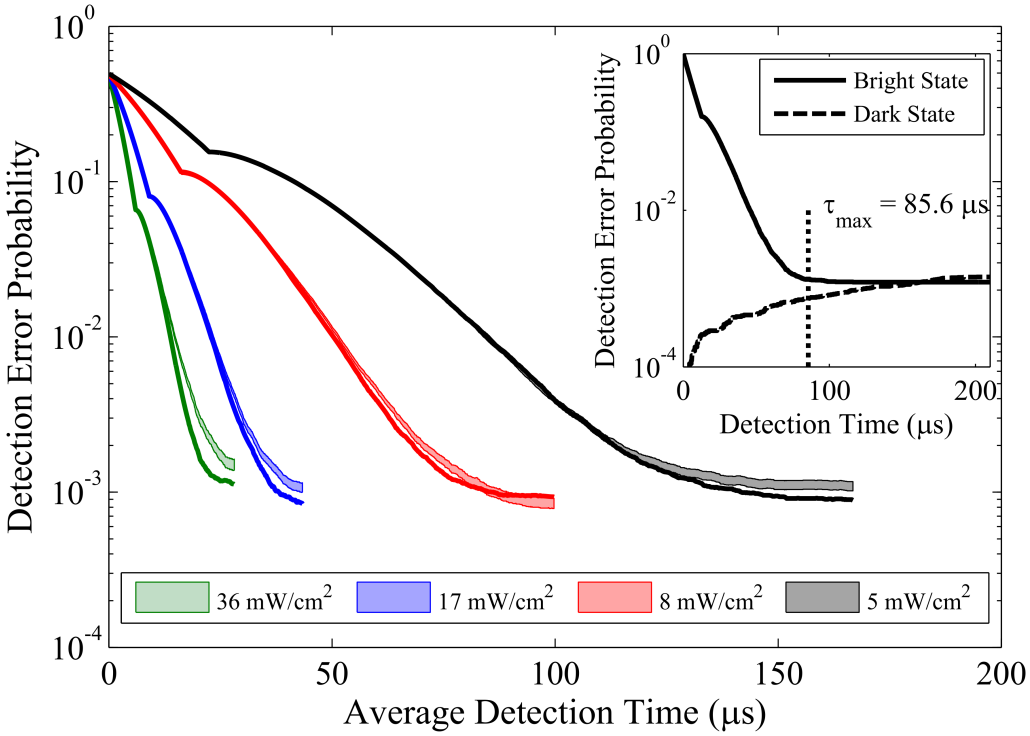

FIGURE 5.7: State detection experimental results and simulations for different intensities of the detection beam. The wide trends are the experimental results where the width indicates the 1/e confidence interval, and the solid lines are simulation results. Inset: The dark and bright state errors for a typical case ($I = 17\,\mathrm{mW/cm^2}$) shown separately. After an optimal detection time $\tau_{\max}$, the increase in the dark state error exceeds the reduction in the bright state error.

The average state detection error determined from 200,000 experiments (100,000 each for $|0\rangle$ and $|1\rangle$ prepared states) is shown in Fig. 5.7, as a function of the average detection time for various levels of detection beam intensities. The curves are generated by plotting the average result from all samples for a maximum detection time ranging from zero to $\tau_{\max}$, and the sharp bends correspond to the detection

time reaching τ_c. The solid lines are generated from the simulation using the relevant rates determined experimentally (procedures shown in Fig. 5.6), and match very well with the experimental results. Table 5.1 compares the average measurement time and fidelity obtained for qubit state detection using the threshold and the TED methods. The results indicate experimental qubit state detection fidelities of 99.856(8)% (99.915(7)%) after an average detection time of 28.1 μs (99.8 μs) at a pump laser intensity of 36 mW/cm^2 (8 mW/cm^2). Using the threshold method, the average detection time increases to $\tau_{\max} = 52.1\,\mu s$ ($\tau_{\max} = 183.1\,\mu s$) and the fidelity degrades slightly. For applications where higher qubit detection speeds are desired, we can use the arrival of the first photon to classify the state to be $|1\rangle$, and dramatically reduce $\tau_{\max}$ at the expense of reduced fidelity. With this approach, our system is capable of achieving a 99% detection fidelity for $\tau_{\max} = 17.0\,\mu s$, with an average detection time of 10.5 μs.

Table 5.1: Average measurement time and fidelity comparison between the threshold and the TED methods.

Intensity (mW/cm^2)	Threshold		TED	
	Time (μs)	Fidelity	Time (μs)	Fidelity
5	301.1	99.882(8)	165.4	99.891(7)
8	183.1	99.892(7)	99.8	99.915(7)
17	85.6	99.883(8)	45.7	99.897(7)
36	52.1	99.831(9)	28.1	99.856(8)

5.1.4 Summary of State Detection Experiments

We have demonstrated a substantial reduction in the direct qubit state detection time for a $^{171}Yb^+$ hyperfine qubit using high NA optics while maintaining a low error rate. The fidelity of the direct state detection for our hyperfine qubit is ultimately limited by off-resonant scattering of the qubit states. Other strategies that increase the photon collection efficiency can be used in tandem with our approach to increase

both fidelity and detection speed (Noek et al., 2010; Shu et al., 2010; Merrill et al., 2011; Maiwald et al., 2012).

The average detection time demonstrated in this work is comparable to the timescale over which a two-qubit gate is typically performed in trapped ion systems. This shows that the state detection might not be the rate-limiting procedure in quantum computations which employ error correction (DiVincenzo and Aliferis, 2007), and also reduces the distance required for realizing space-like separation in a loophole-free Bell test to well below 10 km, making an ion trap system a feasible candidate for this task (Simon and Irvine, 2003).

5.2 Combining a Large NA Lens with a High Optical Access Trap

Having already demonstrated high speed, high fidelity state detection using our large NA collection optics, we are interested in using this light collection method as part of more complex quantum information operations. These include sympathetic cooling with Barium ions, ion shuttling, remote ion entanglement, and ion-ion gates. Unfortunately, the Sandia Thunderbird trap used in the previous experiment is not well-suited for these tasks. Sympathetic cooling and ion-ion gates require stable trapping of ion chains, but a high Mathieu stability parameter q value and low radial secular frequencies make Thunderbird ion chains unstable and motional gates difficult due to the ease of gaining motional quanta (where a single motional quanta $E = \hbar\omega$). Remote ion entanglement and ion-ion gates require high power pulsed lasers to address the ion on short time scales (Moehring et al., 2007; Sørensen and Mølmer, 1999, 2000; Zhu et al., 2006). These high power beams in the UV can cause severe charging of the trap dielectric materials as any part of the beam impinges on the ion trap surface (Harlander et al., 2010), inducing undesired motion of the ion that can be fatal to motional addressing using pulsed lasers. During these operations it is critical that the number of motional quanta remain uninfluenced by the environment

during the gate (Sørensen and Mølmer, 1999). Current surface traps are fabricated on large $\sim$1 cm^2 substrates, with the RF rails oriented so that the pulsed laser beams must propagate along the diagonal (1.4 cm). This results in large pulsed laser beams to keep the divergence of the beam small so that the beam is small at the edge of the trap, and high beam power requirements because the intensity at the ion is low due to the large beam mode diameter. In response to this, Sandia National Laboratories New Mexico, in collaboration with the ion trapping community, has designed and fabricated a high optical access (HOA) trap with a narrow central region to allow large NA optical access, incorporated with a design better suited for trapping ion chains. This section is a report on the setup and findings from the Sandia HOA trap combined with the large NA optics.

5.2.1 Sandia HOA Trap and Large NA Experiment Setup

The Sandia HOA trap (shown in Fig 5.8) is a microfabricated surface trap designed to allow tightly focused beams and have a deep trapping potential with higher transverse secular frequencies at higher RF frequencies than previous generations of traps, which results in lower Mathieu stability parameter q values which are required for stable trapping of ion chains (see Fig. **??**). Prior generations of surface traps require beams with small divergence angles to successfully cross the trap without clipping at the chip edges. As a result, high laser power is required to achieve sufficient optical intensity ($\sim 10^2$ W cm^{-2}) at the ion, which increases the risk of trap surface charging. A Gaussian beam with beam radius w at distance z from the beam waist $w_\circ$ is described by

$$w(z) = w_\circ \sqrt{1 + \left(\frac{z}{z_R}\right)^2}, \tag{5.8}$$

where $z_R = \pi w_\circ^2/\lambda$ is the Rayleigh range of a beam of wavelength λ. To compare the traps, a Gaussian beam with $w_\circ$=15 μm crossing the Sandia Thunderbird trap center

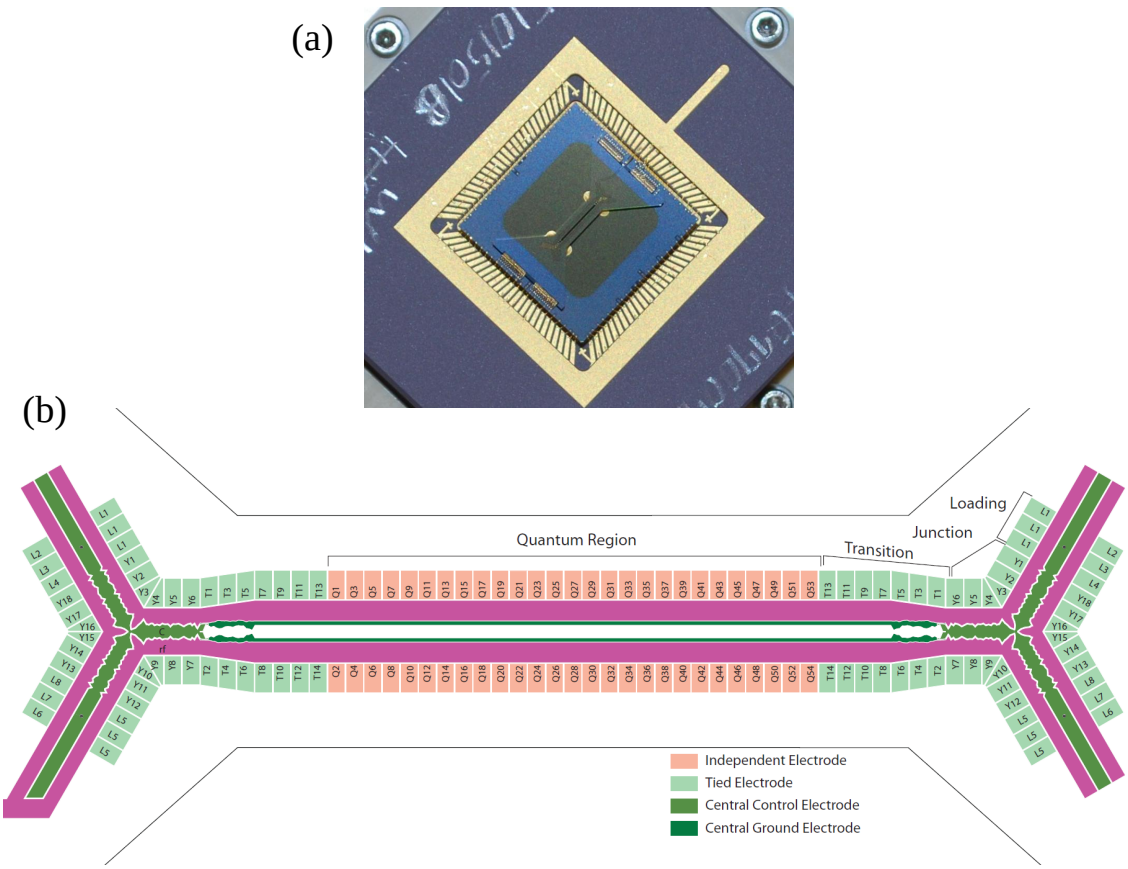

FIGURE 5.8: The Sandia high optical access trap has a narrow central region only 1.2 mm wide that allows high NA beam access to the ion across the chip. (a) A picture of the Sandia HOA used here packaged in a 98-pin CPGA, and (b) a schematic of the trap design with central ion loading slot. (Photograph by Duke team, schematic by Dr. Peter Maunz. Used with permission from Sandia National Laboratories and IARPA.)

at 45° would diverge to $w(7\,\text{mm})$=70 µm at the edge of the trap, whereas the same beam crossing the Sandia HOA trap would only diverge to $w(0.85\,\text{mm})$=16.4 µm at the edge of the trap.

For this setup, the Doppler cooling and detection beams for the Sandia HOA trap are designed to have beam waists of $w_\circ$=15 µm. Without the vacuum window in the path, the cooling beam waist was measured at the $1/e^2$ radius to be 14±1 µm. A ground shield is located 2.5 mm above the surface of the trap with slot NA=0.69 to

avoid clipping of the light collection NA.

5.2.2 Sandia HOA Trap Characterization

Initially, the trap was operated with the same helical resonator used for the Sandia Thunderbird. With an HOA loaded frequency of 24.4 MHz and 260 V of RF at the trap, the weakest trapping direction was >500 meV deep, with radial frequencies near 5.2 MHz and q=0.6. This solution gives an unusually deep trap (for surface traps), which is convenient for initial trap testing, but we have found that the large q makes chain trapping unstable, possibly due to the increased number of resonances with multiple ions and the narrower stability regions along a=0 at higher q values (Leibfried et al., 2003).

The trap heating rate was measured as described in chapter 3 using the Doppler heating method with the 24.4 MHz helical resonator. Raw data from various heating times is plotted in Fig. 5.9. These data are fit to find the starting energy corresponding to the total motional quanta, and the heating rate was determined to be 7.4 quanta/ms with axial secular frequency ω_x=382 kHz, which gives a PSD (see chapter 3) of $\omega S_E(\omega) = 3.67\times10^{-4}\,\mathrm{V^2/m^2}$. Micromotion of the ion is reasonably well compensated in this trap with small adjustments to the DC electrodes, although the micromotion has not been monitored over a long period (many hours) and could be changing slowly over time from charged dielectric fields originating from the front window and passing the very large NA slotted ground shield. The significant exposure to the charged dielectric is a significant concern for this method because it may pose a threat to motion-sensitive gates.

The helical resonator used for the Thunderbird provides a nice single-ion trap, but a very high stability q = 0.6, which is poor for trapping chains. It is possible with the HOA trap to change the RF frequency to reduce the q parameter while maintaining a good trap. Trap simulations allowed us to estimate that a new RF

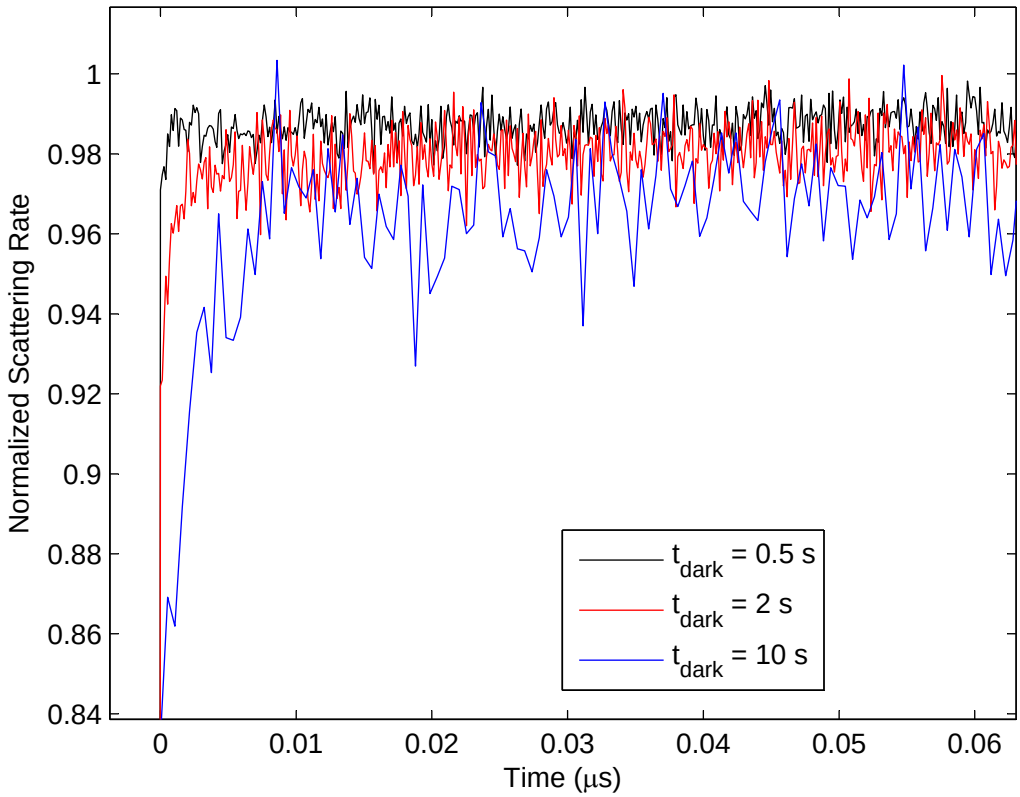

FIGURE 5.9: Doppler recooling measurements to determine the heating for various dark times. The shape of the curve at the beginning of the cooling cycle is fit to determine the different starting energies, which are related to the total motional quanta. Average motional quanta gained per heating period are plotted and linearly fit to find the trap heating rate. Our HOA trap heating rate is 7.4 quanta/ms with an axial secular frequency ω_x=382 kHz.

frequency of 37.5 MHz gives a reasonable trap depth of $\geqslant$140 meV and radial secular frequencies $\geqslant 2\pi\times$2.6 MHz at an RF voltage of 200 V. With the new resonator, linear chains of 2 and 3 ions are easily trapped and appear to have a lifetime of over 20 min.

We have observed an ion detection SBR of up to 3,000 with $\sim$10 μW of cooling beam power focused on a single $^{174}Yb^+$ ion, although it should be noted that this SBR value is not comparable to the quoted Thunderbird SBR due to the difference in isotope ($^{171}Yb^+$ has only $\sim$1/3 the counts of $^{174}Yb^+$ due to coherent dark states). However, the actual state detection SBR has not yet been characterized for this trap.

5.2.3 Future Plans for the HOA Trap

Upcoming challenges for the HOA trap setup include fiber coupling the output of the large NA lens to a UV fiber with a mode diameter of 3 μm; demonstrating shuttling, including heating rate measurements before and after to ascertain whether the qubit will maintain coherence during transfer to a new location; alignment and testing of a pulsed laser for remote ion entanglement, Raman motional ground state cooling, and more precise heating rate measurement. Of these, the most unknown to date is the fiber coupling efficiency from the large NA lens, which has a theoretical mode matching efficiency of 80%. To date, the light has been fiber coupled to 40% efficiency at the University of Maryland, however, the theoretical limit is 80% and it is as yet unclear if given a strong method for the large NA lens alignment it is possible to achieve a coupling closer to the theoretical value. High sensitivity to tilt, short depth of focus (0.027° and ∼1 μm, respectively, correspond to the fiber coupling efficiency dropping to 50%), and the challenge of determining the accuracy of the alignment in real time while the ion is trapped and fiber coupled leave the final possible coupling efficiency and the long term stability of the fiber coupling in question.

5.3 Summary of Large NA Lens Experiments

Large NA light collection from the ion using a custom objective lens provides an essential, immediate solution for increasing the speed and fidelity of any photon-collection based ion trap experiments. A custom objective lens with NA=0.6 provides 10% collection from the ion and has an output Gaussian mode matched to a single mode fiber. Using this lens we have achieved an SBR of 5,000 in ion state detection, resulting in fidelities up to 99.915% in 100 μs. We have further observed a high SBR in ion Doppler cooling measurements of $^{174}Yb^{+}$ using a Sandia HOA trap with a tight beam waist of 15 μm. The large NA lens in combination with an HOA

trap for reduced addressing beam power promise fast, high fidelity detection and manipulation as required for advanced quantum information experiments.

6

Conclusions and Comparison of Light Collection Techniques

Experiments to date using different methods to collect light from a point source show the potential to improve the speed and fidelity of atomic state detection and remote entanglement (Bochmann et al., 2010; Trupke et al., 2005; Noek et al., 2010; Merrill et al., 2011; Noek et al., 2013b,a; Moehring et al., 2007; Shu et al., 2010; Streed et al., 2011). The experiments included in this document cover a wide range of techniques and potential applications. This chapter contains a summary of each method and finally a comparison of the various methods.

6.1 Optical cavities

Optical cavities have great potential for directly collecting a large fraction of emitted light into a single spatial mode. According to our calculations, our integrated fiber-trap-cavity design should allow us to collect 30% of the light emitted by the ion directly into a single mode fiber (Kim et al., 2011). A custom trap design that fits on a 2 mm fiber ferrule surface shows nice trapping characteristics including high trans-

verse secular frequencies around 5 MHz and a deep trapping potential of 270 meV with 200 V of RF. Although the small footprint trap has nice characteristics, we have found that the fiber integration is difficult. Microfabrication, a process that conventionally requires a flat surface, is incompatible with the prerequisite superpolishing process that rounds the surface of the ferruled fiber. This issue is not necessarily insurmountable; for example, the fiber ferrule could be replaced by a larger fused silica plate more compatible with microfabrication processes. Significant challenges would remain in fabricating on a plate with a fragile fiber extending perpendicular to the surface, and in general directly coupling the cavity to a fiber is a difficult task. While our cavity design is difficult to implement, a similar design without direct fiber coupling is significantly more approachable.

6.2 Multiscale optics

Multiscale optics use microscopic optical elements to cover a large solid angle of a point source and relay that light to distant, macroscopic, low aberration optics. Use of microscopic elements close to the source can reduce the size, expense, and, potentially, aberrations that come with comparable macroscopic elements covering the same solid angle. A team of people from Duke and GTRI has developed a process for etching spherical mirrors in a silicon substrate (Merrill et al., 2011). Here, we experimentally verified the capability to collect 27% of the light emitted by a microbead point source when the micromirror is placed close to the microbead and the light is relayed through a low NA lens (NA$\approx$0.2) to an EMCCD (Noek et al., 2010).

The placement of the microbead for highest collection efficiency was closer to the mirror than the focal point of a similarly dimensioned spherical mirror. This is explained with careful characterization of the mirror shape, where three dimensional interferometry scans show that the mirror is only spherical near the center. This is

significant for ion trapping, where the ion height is fixed with the trap design. Also, the closer the ion is to the surface of the trap, the closer the addressing laser is to the trap. This results in collection of more scattered laser light from the surface that could increase the background noise counts.

Concurrently with the microbead light collection testing of the micromirror, micromirror equipped traps were fabricated at GTRI. Two of these traps later came to Duke for state detection measurements. The traps featured 100 μm diameter micromirrors and an ion trapping height of 64 μm, with potential null depth of 60 meV. Multiple microfabrication steps are required to create the trapping electrode structures after the mirrors have been etched in the substrate. Thick, electrically insulating SiO_2 layers that are required to electrically separate the electrodes roughen the surface of the mirror considerably and thereby reduce the reflectivity. No Yb ions were trapped in the trap at Duke, possibly due to the shallow trap depth. However, GTRI measured a collection efficiency enhancement factor of 1.9 for $^{40}Ca^{+}$ ions with a transition at 397 nm. This factor was lower than optimal due to fabrication errors which substantially roughened the mirror surface (Merrill et al., 2011).

6.3 Large NA imaging lens

To date, large NA optics have been our most successful ion emission collection method. In part, this success is due to the ubiquitous design and experimentation already done with macroscopic imaging lenses and the overall simplicity of the setup that allow us to implement the design effectively on the first try. Setup modifications were limited to replacing the front window with a re-entrant window, replacing the ground screen above the trap with a large NA ground screen, and repositioning the trap surface relative to the front window to achieve the optimal imaging characteristics. The highest risk change was significantly increasing the ion exposure to variable stray fields coming from the front window, both by bringing the window closer to

the trap and increasing the NA of the ground shield. No adverse affects have been observed, but further testing is required.

Improving the light collection fraction to 10% in our setup increased the state detection fidelity up to 99.915% (average detection time $\sim$100 μs), and lowered the detection period required to a minimum average of 10.5 μs (fidelity 99%), 40 times faster than previous results (Myerson et al., 2008). The very low background counts and maximized SBR of 5,000 lead to a two-event discrimination method, where we rely on at most the first two PMT counts to determine the internal state of the ion. It is important to note the significant impact of low background counts on the speed of the state determination. More background counts would require us to wait for the arrival of more photons. As the number of photons required to discriminate the state increases, our method approaches the adaptive method in Ref. (Myerson et al., 2008), where the detection event histogram is compared to typical bright and dark state distributions. Therefore even comparable collection efficiencies may not achieve similar detection times or fidelities if the background count rate were significantly higher.

6.4 Comparison of Light Collection Methods

Each of these light collection approaches brings favorable results. Optical cavities are capable of collecting a large fraction of the ion emission into a single spatial mode, but come with the caveat of difficult setup and debugging; our large NA optics are also designed to match single mode fiber at our wavelength of interest with theoretical efficiency of 80%, but require a large front window and increased exposure to window dielectric material that is a source of variable stray fields. Micromirrors integrated in traps are intended only for state detection; the mode shape is very difficult to convert to a single spatial mode for high fiber coupling efficiency and doing so would result in a significant loss of photons that would nullify the benefit. They may also suffer

from high background count rates due to laser scattering when the ion is positioned for maximum light collection.

Initial setup costs vary widely between these, where integrated micromirrors and custom cavities take years of planning, design, and formation before initial demonstration. Alternatively, the large NA lens can be designed by and purchased from a vendor on a shorter time scale and is significantly more likely to meet the specifications after the initial effort. However, all methods are comparably expensive financially today: UV cavities are pricey because of custom mirror coatings and superpolished substrates, integrated micromirrors require a significant amount of clean room and microfabrication costs during development, and custom macroscopic large NA optics are costly due to the custom design, polishing, and assembly. Each of these have reduced cost in large quantities and thus are financially competitive.

Presently, large vacuum chambers are the standard container for ion trap experiments. This macroscopic setup makes large NA optics the easiest optical approach to integrate into existing systems. Increasing numbers of qubits will most likely boost efforts toward miniaturized systems, where large, clunky objective lenses are no longer desirable. When miniaturization is popular, small optical cavities and integrated micro-optics will be necessary to improve the scalability of a trapped ion quantum computer.

Eventually, long-term stability will be a major concern. Some possible long-term cavity issues are ion dependent, including degradation of UV HR coatings over time and strong stray fields originating from proximate dielectric mirror surfaces (Sterk et al., 2012). Mirror decay could require regular maintenance. Micromirrors used as simple reflectors should not suffer significantly, as the overall reflectance does not diminish considerably.

Cavities and micro-optics are still in their infancy with respect to reliable integration, but are promising for future miniaturized systems. Large NA optics are a

strong option for the present wherever high speed, high fidelity state detection is essential.

7

Outlook

Presently, ion trapping systems can benefit from large, external optics specially designed for high ion emission collection efficiency that are easy to integrate into current experiments, and have been tested and characterized (are "risk-free"). There is high time overhead and risk involved in changing the UHV chamber and characterizing a new system. These factors make it undesirable for active systems performing state-of-the art quantum information experiments to perform complete system upgrades to gain higher light collection efficiency optics. The benefit of large NA optics is the simplicity of integration into existing systems. Few to no vacuum system changes are required and the ion trap can remain the same, minimizing the new characterization required of the updated system. Hence, macroscopic, large NA optics are very convenient for the immediate future. However, integrating these optics is only plausible on the scale of a single experiment or a few interconnected experiments. As the complexity of quantum information tasks grows, more ions will be required and bulky components will scale poorly.

It is possible that quantum information may experience growth similar to Moore's Law in density of ions; in this case it will eventually demand small footprints for most

required elements, and it will be useful to have many trap chips close together. A densely-packed ion trap array would require many of the large items in use today to be miniaturized to facilitate such a scheme. Light collection optics would be no exception to this, as there would be no room for 20 mm working distances and 2 in. objective lens diameters.

Significant advances have been made in microoptical designs that have not been discussed herein, including Fresnel microlenses (Brady et al., 2011; Streed et al., 2011) and microcavities (Sterk et al., 2012; Trupke et al., 2005). However, the effects of these proximate optics on the trapping characteristics are largely uncharacterized (Brady et al., 2011; Jechow et al., 2011), and current results show the need for further design and testing (Sterk et al., 2012). Cavities in the UV have dielectric charging issues, such that even long (2 mm) UV cavities where the ion is trapped equidistant to the two mirrors show significant variable displacement of the ion (Sterk et al., 2012). Microlenses with NA>0.6 have been successfully demonstrated with trapped ions, but as yet there has been no quantitative characterization of the trapping conditions in the presence of the microlenses (Jechow et al., 2011; Brady et al., 2011). Other advances in detection include local detectors (Eltony et al., 2013), though currently the quantum efficiency in the UV is very low and the total background counts are high, resulting in poor contrast between bright and dark states.

The path for the future demands small components that can be automatically assembled within the tolerance of the optical design. Recent experiments indicate that success with microlenses is probable; dielectric charging effects and stringent alignment requirements may cause optical cavities to be an arduous route to pursue, but they still hold considerable potential for cavity quantum electrodynamics and the capabilities that may provide and may be well worth the effort.

Appendix A

Derivation of the Optimized Scattering Rate for $^{171}Yb^{+}$

The speed and fidelity of our ion state detection experiments rely on the contrast in detection between the bright and dark ion states. To achieve the optimal contrast, we require the maximum scattering rate for the bright ion state. The scattering rate for $^{171}Yb^{+}$ is maximized when the coherent population trapping of the Zeeman-degenerate states is optimally destabilized. Here we follow the method of Ref. (Berkeland and Boshier, 2002) to obtain the scattering rate.

For any of σ_+, σ_-, or π polarized light, there are two dark states in $^{171}Yb^{+}$. These can be destabilized by lifting the degeneracy with an applied magnetic field (Janik et al., 1985), or by scanning the laser polarization (Shirley and Drullinger, 1994). Fig. A.1 shows the relevant transition for $^{171}Yb^{+}$. To simplify the notation, we label the $^2S^{1/2}\big|F=1, m_f=-1,0,1\big\rangle$ states "1", "2", and "3", respectively, and the $^2P^{1/2}\big|F=0, m_f=0\big\rangle$ state "4".

To find the scattering rate, we consider the time evolution of the density matrix

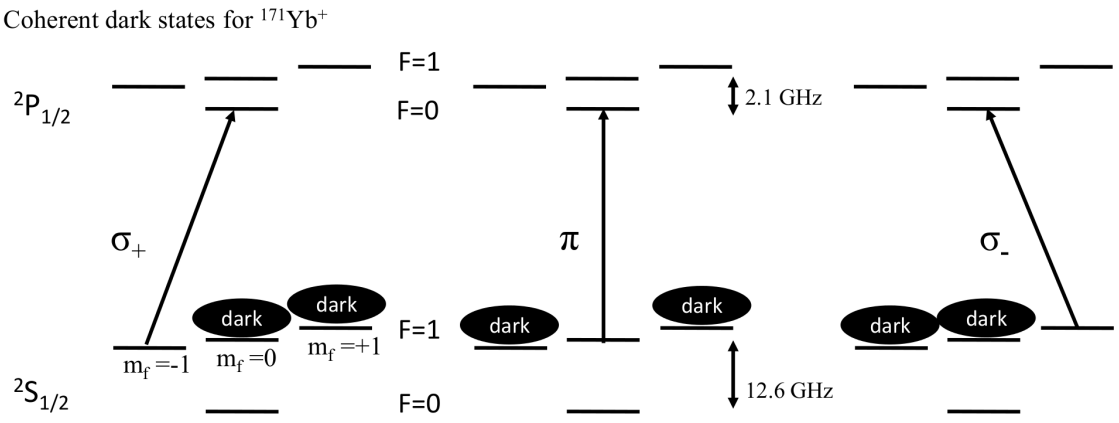

FIGURE A.1: Coherent dark states for $^{171}\mathrm{Yb}^{+}$ affecting the scattering rate $R_{\circ}$.

described by the Liouville equation of motion:

$$\dot{\rho} = \frac{1}{\mathrm{i}\hbar}\left[H, \rho\right] + \dot{\rho}_{\mathrm{r}}, \tag{A.1}$$

where H is the Hamiltonian of the system and $\dot{\rho}_{\mathrm{r}}$ is the spontaneous emission term. The Hamiltonian of the system is

$$H = \hbar \begin{pmatrix} -\delta & 0 & 0 & \frac{\Omega_{-}}{2} \\ 0 & 0 & 0 & \frac{\Omega_{\circ}}{2} \\ 0 & 0 & \delta & \frac{\Omega_{+}}{2} \\ \frac{\Omega_{-}}{2} & \frac{\Omega_{\circ}}{2} & \frac{\Omega_{+}}{2} & \Delta, \end{pmatrix} \tag{A.2}$$

where δ is the Zeeman shift of the magnetic field sensitive $^{2}\mathrm{S}^{1/2}\big|F=1, m_f=\pm 1\big\rangle$ states from the $^{2}\mathrm{S}^{1/2}\big|F=1, m_f=0\big\rangle$ state, Δ is the laser detuning, $\Omega_{\pm}$ are the Rabi rates corresponding to the $\sigma_{\pm}$ polarized light transitions and $\Omega_{\circ}$ is the Rabi rate corresponding to the π polarized light transition. The relaxation term is

$$\dot{\rho}_{\mathrm{r}} = \begin{pmatrix} \frac{\Gamma}{3}\rho_{44} & 0 & 0 & -\frac{\Gamma}{2}\rho_{14} \\ 0 & \frac{\Gamma}{3}\rho_{44} & 0 & -\frac{\Gamma}{2}\rho_{24} \\ 0 & 0 & \frac{\Gamma}{3}\rho_{44} & -\frac{\Gamma}{2}\rho_{34} \\ -\frac{\Gamma}{2}\rho_{41} & -\frac{\Gamma}{2}\rho_{42} & -\frac{\Gamma}{2}\rho_{43} & -\Gamma\rho_{44} \end{pmatrix}. \tag{A.3}$$

Here, we assume the magnetic field is applied in the positive $\hat{z}$-direction and that our light propagates perpendicular to this field as in our system, and we obtain the Rabi frequencies

$$\Omega_{\pm} = \mp\Omega\frac{\sin\theta}{\sqrt{2}},\ \Omega_{\circ} = \Omega\cos\theta$$

We use that constraint that $\rho_{11} + \rho_{22} + \rho_{33} + \rho_{44} = 1$ and solve for the steady state solution to find ρ_{44}, which is related to the scattering rate by the spontaneous emission rate $R_{\circ} = \Gamma\rho_{44}$. This yields

$$R_{\circ} = \Gamma\rho_{44} = 3\Gamma\frac{\Omega^2\cos^2\theta\sin^2\theta}{1+3\cos^2\theta}\left(\frac{1}{(\Gamma')^2+4\Delta^2}\right), \tag{A.4}$$

$$(\Gamma')^2 = \Gamma^2 + 4\Omega^2\cos^2\theta\frac{1-3\cos^2\theta}{1+3\cos^2\theta} + \frac{4\cos^2\theta}{1+3\cos^2\theta}\left(\frac{\Omega^4}{4\delta^2}+4\delta^2\right). \tag{A.5}$$

From these we find that the scattering rate is maximized for Zeeman splitting $\delta = \Omega/2$, and polarization corresponding to $\theta = \arccos(1\sqrt{3})$. It is also worth noting that for only π polarized light ($\theta = 0$), only $\sigma_{\pm}$ polarized light, or a Zeeman splitting $\delta = 0$, the scattering rate goes to zero as expected.

Assuming optimal polarization and Zeeman splitting and substituting $s_{\circ} = 2\Omega^2/\Gamma^2$, the scattering rate simplifies to that given in chapter 5:

$$R_{\circ,\mathrm{opt}} = \left(\frac{\Gamma}{6}\right)\frac{s_{\circ}}{1+\frac{2}{3}s_{\circ}+\left(\frac{2\Delta}{\Gamma}\right)^2}. \tag{A.6}$$

Instead of solving the 7×7 matrices for the dark pumping rate, R_d is obtained by noting that the differences in Eqn. A.6 from the scattering rate for a simple two-level system are a factor of 1/3 for the ratio of bright to dark states, and the factor of 2/3 affecting $s_{\circ}$ in the denominator. The latter becomes insignificant for very large detuning as in the case for dark pumping, so we estimate R_d to be

$$R_d \approx \left(\frac{2}{3}\right)\left(\frac{1}{3}\right)\left(\frac{\Gamma}{2}\right)\left(\frac{2\Omega^2}{\Gamma^2}\right)\left(\frac{\Gamma}{2\Delta_{\mathrm{HFS}}}\right)^2, \tag{A.7}$$

where Δ_{HFS}=12.6 GHz is the hyperfine splitting of the $^2\mathrm{S}^{1/2}$ level, the factor of 2/3 is the ratio of bright to dark states for a given pure polarization, and the factor of 1/3 is the branching ratio to the $^2\mathrm{S}^{1/2}\big|F=0, m_f=0\big\rangle$ state. For the bright pumping rate R_b we use the scattering rate for a two-level system because R_b has no coherent dark states.

Bibliography

Beckman, D., Chari, A. N., Devabhaktuni, S., and Preskill, J. (1996), "Efficient networks for quantum factoring," *Phys. Rev. A*, 54, 1034–.

Bergquist, J. C., Hulet, R. G., Itano, W. M., and Wineland, D. J. (1986), "Observation of Quantum Jumps in a Single Atom," *Phys. Rev. Lett.*, 57, 1699–1702.

Berkeland, D. J. and Boshier, M. G. (2002), "Destabilization of dark states and optical spectroscopy in Zeeman-degenerate atomic systems," *Phys. Rev. A*, 65, 033413.

Bochmann, J., Mucke, M., Guhl, C., Ritter, S., Rempe, G., and Moehring, D. L. (2010), "Lossless State Detection of Single Neutral Atoms," *Phys. Rev. Lett.*, 104, 203601.

Brady, D. J. and Hagen, N. (2009), "Multiscale lens design," 17, 10659–10674.

Brady, G., Ellis, A., Moehring, D., Stick, D., Highstrete, C., Fortier, K., Blain, M., Haltli, R., Cruz-Cabrera, A., Briggs, R., Wendt, J., Carter, T., Samora, S., and Kemme, S. (2011), "Integration of fluorescence collection optics withamicrofabricated surface electrode ion trap," *Applied Physics B*, 103, 801–808.

Cirac, J. I. and Zoller, P. (2000), "A scalable quantum computer with ions in an array of microtraps," *Nature*, 404, 579–581.

Coppersmith, D. (1994), "An Approximate Fourier Transform Useful in Quantum Factoring," Research Report RC19642, IBM.

DiVincenzo, D. P. and Aliferis, P. (2007), "Effective fault-tolerant quantum computation with slow measurements," *Phys. Rev. Lett.*, 98, 020501.

Drever, R., Hall, J., Kowalski, F., Hough, J., Ford, G., Munley, A., and Ward, H. (1983), "Laser phase and frequency stabilization using an optical resonator," 31, 97–105–.

Elson, J. M. and Bennett, J. M. (1995), "Calculation of the power spectral density from surface profile data," *Appl. Opt.*, 34, 201–208.

Eltony, A. M., Wang, S. X., Akselrod, G. M., Herskind, P. F., and Chuang, I. L. (2013), "Transparent ion trap with integrated photodetector," *Applied Physics Letters*, 102, 054106.

Epstein, R. J., Seidelin, S., Leibfried, D., Wesenberg, J. H., Bollinger, J. J., Amini, J. M., Blakestad, R. B., Britton, J., Home, J. P., Itano, W. M., Jost, J. D., Knill, E., Langer, C., Ozeri, R., Shiga, N., and Wineland, D. J. (2007), "Simplified motional heating rate measurements of trapped ions," *Phys. Rev. A*, 76, 033411.

Feynman, R. (1986), "Quantum mechanical computers," *Foundations of Physics*, 16, 507–531, 10.1007/BF01886518.

Fisk, P., Sellars, M., Lawn, M., and Coles, G. (1997), "Accurate measurement of the 12.6 GHz "clock" transition in trapped $^{171}Yb^{+}$ ions," *Ultrasonics, Ferroelectrics and Frequency Control, IEEE Transactions on DOI - 10.1109/58.585119*, 44, 344–354.

Grover, L. K. (1996), "A fast quantum mechanical algorithm for database search," in *Proceedings of the twenty-eighth annual ACM symposium on Theory of computing*, pp. 212–219, Philadelphia, Pennsylvania, United States, ACM.

Guthohrlein, G. R., Keller, M., Hayasaka, K., Lange, W., and Walther, H. (2001), "A single ion as a nanoscopic probe of an optical field," *Nature*, 414, 49–51.

Haffner, H., Hansel, W., Roos, C. F., Benhelm, J., Chek-al kar, D., Chwalla, M., Korber, T., Rapol, U. D., Riebe, M., Schmidt, P. O., Becher, C., Guhne, O., Dur, W., and Blatt, R. (2005), "Scalable multiparticle entanglement of trapped ions," *Nature*, 438, 643–646.

Harlander, M., Brownnutt, M., Hansel, W., and Blatt, R. (2010), "Trapped-ion probing of light-induced charging effects on dielectrics," *New Journal of Physics*, 12, 093035.

Herskind, P. F., Wang, S. X., Shi, M., Ge, Y., Cetina, M., and Chuang, I. L. (2011), "Microfabricated surface ion trap on a high-finesse optical mirror," *Opt. Lett.*, 36, 3045–3047.

Hite, D. A., Colombe, Y., Wilson, A. C., Brown, K. R., Warring, U., Jrdens, R., Jost, J. D., McKay, K. S., Pappas, D. P., Leibfried, D., and Wineland, D. J. (2012), "100-Fold Reduction of Electric-Field Noise in an Ion Trap Cleaned with InSitu Argon-Ion-Beam Bombardment," *Phys. Rev. Lett.*, 109, 103001–.

Hume, D. B., Rosenband, T., and Wineland, D. J. (2007), "High-fidelity adaptive qubit detection through repetitive quantum nondemolition measurements," *Phys. Rev. Lett.*, 99, 120502.

Janik, G., Nagourney, W., and Dehmelt, H. (1985), "Doppler-free optical spectroscopy on the Ba+ mono-ion oscillator," *J. Opt. Soc. Am. B*, 2, 1251–1257.

Jechow, A., Streed, E. W., Norton, B. G., Petrasiunas, M. J., and Kielpinski, D. (2011), "Wavelength-scale imaging of trapped ions using a phase Fresnel lens," *Opt. Lett.*, 36, 1371–1373.

Kim, J. and Kim, C. (2009), "Integrated optical approach to trapped ion quantum computation," *Quant. Inf. Comput.*, 9, 181 – 202.

Kim, J., Pau, S., Ma, Z., McLellan, H., Gages, J., Kornblit, A., and Slusher, R. (2005), "System design for large-scale ion trap quantum information processor," *Quant. Inf. Comp.*, 5, 515.

Kim, T., Maunz, P., and Kim, J. (2011), "Efficient collection of single photons emitted from a trapped ion into a single-mode fiber for scalable quantum-information processing," *Phys. Rev. A*, 84, 063423–.

King, B. E. (1999), "Quantum State Engineering and Information Processing with Trapped Ions," Ph.D. thesis, University of Colorado, Boulder.

Langer, C. E. (2006), "High fidelity quantum information processing with trapped ions," Ph.D. thesis, University of Colorado at Boulder.

Leibfried, D., Blatt, R., Monroe, C., and Wineland, D. (2003), "Quantum dynamics of single trapped ions," *Rev. Mod. Phys.*, 75, 281–324.

Leibfried, D., Knill, E., Seidelin, S., Britton, J., Blakestad, R. B., Chiaverini, J., Hume, D. B., Itano, W. M., Jost, J. D., Langer, C., Ozeri, R., Reichle, R., and Wineland, D. J. (2005), "Creation of a six-atom 'Schrodinger cat' state," *Nature*, 438, 639–642.

Luo, L., Hayes, D., Manning, T., Matsukevich, D., Maunz, P., Olmschenk, S., Sterk, J., and Monroe, C. (2009), "Protocols and techniques for a scalable atom-photon quantum network," *Fortschr. Phys.*, 57, 1133–1152.

Macalpine, W. and Schildknecht, R. (1959), "Coaxial Resonators with Helical Inner Conductor," *Proceedings of the IRE DOI - 10.1109/JRPROC.1959.287128*, 47, 2099–2105.

Maiwald, R., Leibfried, D., Britton, J., Bergquist, J. C., Leuchs, G., and Wineland, D. J. (2009), "Stylus ion trap for enhanced access and sensing," *Nat. Phys.*, 5, 551–554.

Maiwald, R., Golla, A., Fischer, M., Bader, M., Heugel, S., Chalopin, B., Sondermann, M., and Leuchs, G. (2012), "Collecting more than half the fluorescence photons from a single ion," *Phys. Rev. A*, 86, 043431.

Matsukevich, D. N., Maunz, P., Moehring, D. L., Olmschenk, S., and Monroe, C. (2008), "Bell Inequality Violation with Two Remote Atomic Qubits," *Phys. Rev. Lett.*, 100, 150404–.

Matsuyama, T., Ohmura, Y., and Williamson, D. M. (2006), "The lithographic lens: its history and evolution," in *Proceedings of SPIE Volume 6154*.

Merrill, J. T., Volin, C., Landgren, D., Amini, J. M., Wright, K., Doret, S. C., Pai, C.-S., Hayden, H., Killian, T., Faircloth, D., Brown, K. R., Harter, A. W., and Slusher, R. E. (2011), "Demonstration of integrated microscale optics in surface-electrode ion traps," *New Journal of Physics*, 13, 103005–.

Moehring, D. L., Maunz, P., Olmschenk, S., Younge, K. C., Matsukevich, D. N., Duan, L.-M., and Monroe, C. (2007), "Entanglement of single-atom quantum bits at a distance," *Nature*, 449, 68–71.

Molmer, K. and Sorensen, A. (1999), "Multiparticle Entanglement of Hot Trapped Ions," *Phys. Rev. Lett.*, 82, 1835–1838.

Monroe, C. and Kim, J. (2013), "Scaling the Ion Trap Quantum Processor," *Science*, 339, 1164.

Monz, T., Schindler, P., Barreiro, J. T., Chwalla, M., Nigg, D., Coish, W. A., Harlander, M., Hänsel, W., Hennrich, M., and Blatt, R. (2011), "14-Qubit Entanglement: Creation and Coherence," *Phys. Rev. Lett.*, 106, 130506.

Mount, E., Baek, S.-Y., Blain, M., Stick, D., Gaultney, D., Crain, S., Noek, R., Kim, T., Maunz, P., and Kim, J. (2013), "Single qubit manipulation in a microfabricated surface electrode ion trap," *New Journal of Physics*, 15, 093018–.

Mundt, A. B., Kreuter, A., Becher, C., Leibfried, D., Eschner, J., Schmidt-Kaler, F., and Blatt, R. (2002), "Coupling a Single Atomic Quantum Bit to a High Finesse Optical Cavity," *Phys. Rev. Lett.*, 89, 103001–.

Myerson, A. H., Szwer, D. J., Webster, S. C., Allcock, D. T. C., Curtis, M. J., Imreh, G., Sherman, J. A., Stacey, D. N., Steane, A. M., and Lucas, D. M. (2008), "High-fidelity readout of trapped-ion qubits," *Phys. Rev. Lett.*, 100, 200502.

Nagourney, W., Sandberg, J., and Dehmelt, H. (1986), "Shelved optical electron amplifier: observation of quantum jumps," *Phys. Rev. Lett.*, 56, 2797.

Noek, R., Knoernschild, C., Migacz, J., Kim, T., Maunz, P., Merrill, T., Hayden, H., Pai, C. S., and Kim, J. (2010), "Multiscale optics for enhanced light collection from a point source," *Opt. Lett.*, 35, 2460–2462.

Noek, R., Vrijsen, G., Gaultney, D., Mount, E., Kim, T., Maunz, P., and Kim, J. (2013a), "High speed, high fidelity detection of an atomic hyperfine qubit," *Opt. Lett.*, 38, 4735–4738.

Noek, R., Kim, T., Mount, E., Baek, S.-Y., Maunz, P., and Kim, J. (2013b), "Trapping and cooling of 174Yb+ ions in a microfabricated surface trap," *J. Korean Phys. Soc.*, 63, 907–913.

Odlyzko, A. (1995), "The future of integer factorization," *CryptoBytes (The technical newletter of RSA Laboratories)*, 1, 2.

Olmschenk, S. (2009), "Quantum Teleportation Between Distant Matter Qubits," Physics, University of Maryland.

Olmschenk, S., Younge, K. C., Moehring, D. L., Matsukevich, D. N., Maunz, P., and Monroe, C. (2007), "Manipulation and detection of a trapped Yb^+ hyperfine qubit," *Phys. Rev. A*, 76, 052314.

Paul, W. (1990), "Electromagnetic traps for charged and neutral particles," *Rev. Mod. Phys.*, 62, 531.

Pound, R. (1946), "Electronic Frequency Stabilization of Microwave Oscillators," *Review of Scientific Instruments*, 17, 490–505.

Purcell, E. M. (1946), "Spontaneous emission probabilities at radio frequencies," *Phys. Rev.*, 69, 681.

Rarity, J. G. and Tapster, P. R. (1990), "Experimental violation of Bell's inequality based on phase and momentum," *Phys. Rev. Lett.*, 64, 2495–2498.

Ritter, S., Nölleke, C., Hahn, C., Reiserer, A., Neuzner, A., Uphoff, M., Mücke, M., Figueroa, E., Bochmann, J., and Rempe, G. (2012), "An elementary quantum network of single atoms in optical cavities," *Nature*, 484, 195–201.

Robbins, H. and Schwartz, B. (1960), "Chemical Etching of Silicon," *J. Electrochem. Soc.*, 107, 108–111.

Sauter, T., Neuhauser, W., Blatt, R., and Toschek, P. E. (1986), "Observation of quantum jumps," *Phys. Rev. Lett.*, 57, 1696.

Schaetz, T., Barrett, M. D., Leibfried, D., Britton, J., Chiaverini, J., Itano, W. M., Jost, J. D., Knill, E., Langer, C., and Wineland, D. J. (2005), "Enhanced quantum state detection efficiency through quantum information processing," *Phys. Rev. Lett.*, 94, 010501.

Seidelin, S., Chiaverini, J., Reichle, R., Bollinger, J. J., Leibfried, D., Britton, J., Wesenberg, J. H., Blakestad, R. B., Epstein, R. J., Hume, D. B., Itano, W. M., Jost, J. D., Langer, C., Ozeri, R., Shiga, N., and Wineland, D. J. (2006), "Microfabricated Surface-Electrode Ion Trap for Scalable Quantum Information Processing," *Phys. Rev. Lett.*, 96, 253003.

Shirley, J. and Drullinger, R. (1994), "Zeeman coherences and dark states in optically pumped cesium frequency standards," in *Precision Electromagnetic Measurements, 1994. Digest., 1994 Conference on*, pp. 150–151.

Shor, P. (1994), "Algorithms for quantum computation:Discrete logarithms and factoring," in *Proceedings of the 35th Annual Symposium on Foundations of Computer Science*, ed. S. Goldwasser, pp. pp. 124–134, IEEE Computer Society Press, Los Alamitos, CA.

Shu, G., Dietrich, M. R., Kurz, N., and Blinov, B. B. (2009), "Trapped ion imaging with a high numerical aperture spherical mirror," *Journal of Physics B: Atomic, Molecular and Optical Physics*, 42, 154005–.

Shu, G., Kurz, N., Dietrich, M. R., and Blinov, B. B. (2010), "Efficient fluorescence collection from trapped ions with an integrated spherical mirror," *Phys. Rev. A*, 81, 042321.

Simon, C. and Irvine, W. T. M. (2003), "Robust long-distance entanglement and a loophole-free Bell test with ions and photons," *Phys. Rev. Lett.*, 91, 110405.

Sørensen, A. and Mølmer, K. (1999), "Quantum Computation with Ions in Thermal Motion," *Phys. Rev. Lett.*, 82, 1971–1974.

Sørensen, A. and Mølmer, K. (2000), "Entanglement and quantum computation with ions in thermal motion," *Phys. Rev. A*, 62, 022311.

Sterk, J. D., Luo, L., Manning, T. A., Maunz, P., and Monroe, C. (2012), "Photon collection from a trapped ion-cavity system," *Phys. Rev. A*, 85, 062308–.

Stick, D. (2007), "Fabrication and Characterization of Semiconductor Ion Traps for Quantum Information Processing," Ph.D. thesis, The University of Michigan.

Stick, D., Hensinger, W. K., Olmschenk, S., Madsen, M. J., Schwab, K., and Monroe, C. (2006), "Ion trap in a semiconductor chip," *Nature Physics*, 2, 36.

Stick, D., Fortier, K., Haltli, R., Highstrete, C., Moehring, D., Tigges, C., and Blain, M. (2010), "Demonstration of a microfabricated surface electrode ion trap," http://arxiv.org/abs/1008.0990v2.

Streed, E. W., Norton, B. G., Jechow, A., Weinhold, T. J., and Kielpinski, D. (2011), "Imaging of Trapped Ions with a Microfabricated Optic for Quantum Information Processing," *Phys. Rev. Lett.*, 106, 010502–.

Trupke, M., Hinds, E. A., Eriksson, S., Curtis, E. A., Moktadir, Z., Kukharenka, E., and Kraft, M. (2005), "Microfabricated high-finesse optical cavity with open access and small volume," *Applied Physics Letters*, 87, 211106.

Vandersypen, L. M. K., Steffen, M., Breyta, G., Yannoni, C. S., Sherwood, M. H., and Chuang, I. L. (2001), "Experimental realization of Shor's quantum factoring algorithm using nuclear magnetic resonance," *Nature*, 414, 883–887.

VanDevender, A. P., Colombe, Y., Amini, J., Leibfried, D., and Wineland, D. J. (2010), "Efficient Fiber Optic Detection of Trapped Ion Fluorescence," *Phys. Rev. Lett.*, 105, 023001.

Wang, S. X., Hao Low, G., Lachenmyer, N. S., Ge, Y., Herskind, P. F., and Chuang, I. L. (2011), "Laser-induced charging of microfabricated ion traps," *Journal of Applied Physics*, 110, 104901–104901–7.

Wesenberg, J. H., Epstein, R. J., Leibfried, D., Blakestad, R. B., Britton, J., Home, J. P., Itano, W. M., Jost, J. D., Knill, E., Langer, C., Ozeri, R., Seidelin, S., and Wineland, D. J. (2007), "Fluorescence during Doppler cooling of a single trapped atom," *Phys. Rev. A*, 76, 053416–.

Wineland, D. J., Bergquist, J. C., Itano, W. M., and Drullinger, R. E. (1980), "Double-resonance and optical-pumping experiments on electromagnetically confined, laser-cooled ions," *Opt. Lett.*, 5, 245.

Wineland, D. J., Monroe, C., Itano, W. M., Leibfried, D., King, B. E., and Meekhof, D. M. (1998), "Experimental issues in coherent quantum-state manipulation of trapped atomic ions," *J. Res. Nat. Inst. Stand. Tech.*, 103, 259–328.

Zhu, S.-L., Monroe, C., and Duan, L.-M. (2006), "Trapped Ion Quantum Computation with Transverse Phonon Modes," *Phys. Rev. Lett.*, 97.

Biography

Rachel Noek was born in Albuquerque, New Mexico on September 11, 1983. After graduating from high school in May of 2001, she started a long and productive internship at Sandia National Laboratories, NM under the advisement of Dr. Steven Thornberg, an expert chemist in mass spectrometry and gas analysis techniques. After three years, she changed mentors to Dr. Jerilyn Timlin to work on hyperspectral image analysis for biological materials. Rachel earned her Bachelor's of Science in Mathematics from the University of New Mexico and was named the Top Graduating Senior in Distributed Mathematics in 2005. For three years after graduating, she continued her hyperspectral imaging work at Sandia in a laboratory support role.

By the Fall of 2007, she was excited to learn something new and submitted applications for graduate school. The Fall of 2008 found Rachel at Duke University to earn a Ph.D. in Electrical Engineering in the topic of quantum information science under the guidance of Prof. Jungsang Kim. She made her choice by determining that quantum information sounded the most futuristic and challenging of all her choices. Rachel finished her Ph.D at Duke in December of 2013.